Model-Based Performance Analysis of Filtration Devices and Membrane Adsorbers

Modellbasierte Untersuchung der Leistung von Filtereinheiten und Membranadsorbern

Von der Fakultät für Maschinenwesen der Rheinisch-Westfälischen Technischen Hochschule Aachen zur Erlangung des akademischen Grades einer Doktorin der Ingenieurwissenschaften genehmigte Dissertation

vorgelegt von

Eirini Velali

Berichter: Univ.-Prof. Dr. rer. nat. Wolfgang Wiechert

Univ.-Prof. Dr.-Ing. Matthias Wessling

Tag der mündlichen Prüfung: 12.12.2018

Diese Dissertation ist auf den Internetseiten der Universitätsbibliothek online verfügbar.

Not everything that can be counted counts. Not everything that counts can be counted.

A. Einstein

To my parents, Giorgos & in memory of the beloved ones

Acknowledgments

First, I would like to thank Prof. Wolfgang Wiechert for offering me the possibility to pursue my PhD project at the Institute of Bio- and Geo-Sciences 1 (IBG-1). I am also grateful to Prof. Wolfgang Wiechert and to Prof. Matthias Wessling for agreeing to review my PhD thesis. In addition, I would like to express my gratitude to my scientific advisor Dr. Eric von Lieres for his support and guidance during the project. I gratefully acknowledge our industrial partner Sartorius Stedim Biotech and especially Dr. Martin Leuthold, Dr. Thomas Loewe, Sebastian Handt and Jannik Dippel for providing data and for the fruitful discussions. I would also like to thank my group and colleagues for the nice working environment. Moreover, I am thankful to Prof. Alexander Aivasidis for his advice and help to start my PhD studies. Finally, I am grateful to my family for their unconditional love and support.

Zusammenfassung

Filtereinheiten und Membranadsorber werden in der Biotechnologie häufig verwendet, um Zielmoleküle von Unreinheiten zu trennen. Filtrationseinheiten enthalten typischerweise ein oder zwei Membranlagen, die um einen zylindrischen Kern in Falten angeordnet sind. Diese Membranlagen werden durch Fleecelagen und einen Plastikkäfig an ihrem Platz gehalten. Die Wasserflussrate bei verschiedenen Druckabfällen ist ein wichtiger Performance-Indikator für solche Filtereinheiten. Diese Performanz wurde mittels Computational Fluid Dynamics (CFD) untersucht, und die Ergebnisse wurden durch experimentelle Daten validiert. Vier verschiedene Methoden zur Rekonstruktion der Geometrie der gefalteten Membranen wurden entwickelt und verglichen. Der Einfluss des Plastikkäfigs auf die Wasserflussrate wurde mit Hilfe von 3D-Smulationen beurteilt. Die Resultate zeigen, dass dieser Käfig einen vernachlässigbaren Einfluss auf die Wasserflussrate hat, außer für sehr große Permeabilitäten der porösen Region die für praktische Anwendungen nicht relevant sind. Die Fleecelagen haben einen signifikanten Einfluss auf die Wasserflussrate. Die Permeabilität der Fleecelagen ist kompliziert zu messen, und direkte Experimentaldaten waren für diese Studie nicht verfügbar. Deshalb mussten die Permeabilitäten aus den gemessenen Wasserflussraten bestimmt werden. Die geschätzten Werte hängen von der Wasserflussrate ab, die durch die Kompression der Fleecelagen zum Zentrum der Filtereinheit hin beeinflusst werden, was in der Geometrie der CFD-Simulationen jedoch nicht explizit berücksichtigt ist. Der Kompressionsgrad hängt auch von der Anzahl der Falten und dem Kerndurchmesser ab. Zwischen dem Widerstand (1/Permeabilität) und dem Druckabfall wurde ein linearer Zusammenhang festgestellt, was eine Vorhersage des gesamten Bereichs auf Basis von nur zwei Datenpunkte für die Filtereinheit erlaubt. Darüber hinaus erlauben die CFD-Simulationen, geschätzte Permeabilitäten zwischen Filtereinheiten mit ähnlichen Membraneigenschaften zu übertragen. Membranadsorber (MA) beinhalten gewöhnlich viel mehr Membranschichten, als gefaltete Filter, um eine größere Betthöhe zu erreichen. Prozesse werden häufig im Kleinmaßstab entwickelt und dann auf größere Maßstäbe übertragen. Diese Übertragung wird grundsätzlich durch unterschiedliches Skalierungsverhalten von fluss- und bindungsbezogenen Nichtidealitäten erschwert. CFD-Simulationen erlauben, Modellparameter konsistent zwischen Skalen zu übertragen, indem die Einflüsse dieser Nichtidealitäten unabhängig voneinander beschrieben und damit entkoppelt werden. In dieser Studie werden vier kommerzielle MA untersucht, die die gleiche Membran beinhalten. Sie habe Membranvolumen von 0.08 ml bis 1.6 L. Sie besitzt eine besonders komplizierte Geometrie, die im Gegensatz zu den anderen Einheiten dreidimensionale Simulationen erfordert. Darüber hinaus können diese sogenannten Kassetten parallelisiert werden, um Volumina von bis zu 20.8 L und darüber hinaus zu prozessieren. Die geschätzten Adsorptions- und Desorptionsraten hängen von der Flussrate ab, was durch eine Kombination von konvektivem und diffusivem Fluss in den Mikroporen der Membran erklärt werden kann. Die Gleichgewichtskonstante und alle anderen Bindungsparameter bleiben davon jedoch unberührt. Darüber hinaus kann der Skalenwechsel durch produktionsbedingte Variationen in der Bindungskapazität der Membranen erschwert werden. Dieses Problem kann praktisch gelöst werden, indem die CFD-Simulationen mit nur einem Experiment mit einer Membran aus der gleichen Produktionscharge kalibriert werden.

Summary

Filtration devices and membrane adsorbers are commonly applied in biotechnology for separating target biomolecules from impurities. Filtration devices typically contain one or two membrane layers that are arranged in pleats around a cylindrical core. These membrane layers are held in place by fleece layers and a plastic cage. The water flow rate at different pressure drops is an important performance indicator for such filtration devices. This performance has been studied using Computational Fluid Dynamics (CFD), and the results were validated against experimental data. Four different methods for reconstructing the geometry of the pleated membrane were developed and compared. The impact of the plastic cage on the water flow rate was assessed using 3D simulations. The results reveal that this plastic cage has a negligible influence on the water flow rate except for very high permeabilities of the porous region that are not relevant for practical applications. However, the fleece layer has a significant impact on the water flow rate. The permeability of fleece layers is complicated to measure and direct experimental information was not available for this study. Hence, the unknown fleece permeability had to be determined from the measured water flow rates of the cartridges. The estimated values depend on the flow rate because they are affected by compression of the fleece layers towards the center of the device which is not explicitly accounted for in the geometry of the CFD simulations. The degree of compression also depends on the number of pleats and the core diameter. A linear dependency was found between the resistance (1/permeability) and the pressure drop, which allows predicting the full range from only two data points of a cartridge. Moreover, CFD simulations allow to transfer estimated fleece permeabilities between filtration devices with similar membrane properties. Membrane adsorbers (MA)s typically contain many more membrane layers than pleated filters in order to achieve larger bed height. Processes are often developed at small scales and then transferred to larger scales. This transfer is generally complicated by differences in the scaling behaviour of flow and binding related non-idealities. CFD simulations allow to consistently transfer model parameters across scales by independently capturing and practically decoupling the impacts of these non-idealities. In this study four commercial MAs are analyzed which contain the same membrane. They have membrane volumes from 0.08 mL to 1.6 L. The largest device has recently been introduced to the market. In addition, these so-called Cassettes can be parallelized to process volumes of up to 20.8 L and above. The estimated adsorption and desorption rates are flow rate dependent, which can be explained by a combination of convective and diffusive transport in the micro-pores of the membrane. However, the equilibrium constant and all other binding parameters are unaffected by that. Scale-up can be additionally complicated by batch-to-batch variations in the membrane capacity. This problem can be practically resolved by calibrating the CFD simulation to just one experiment with membrane from the same production batch.

List of abbreviations

Abbreviation	Meaning
AeDNV	Aedes aegypti DensoNucleosis Virus
BSA	Bovine Serum Albumin
BTC	Breakthrough Curve
BDF	Backward Differentiation Formula
CAD	Computer Aided Design
CFD	Computational Fluid Dynamics
CSTR	Continuous Stirred-Tank Reactor
EDM	Equilibrium Dispersive Model
IgG	Immunoglubolin G
LRV	Log Reduction Value
MA	Membrane Adsorber
mAb	Monoclonal Antibody
MRI	Magnetic Resonance Imaging
MUMPS	Multifrontal Massively Parallel sparse direct Solver
MV	Membrane Volume
PFR	Plug Flor Reactor
PVDF	Polyvinylidene fluoride
Re	Reynolds number
RE	Relative error
SMA	Steric Mass Action
TSD	Transport Dispersive Model
VLP	Virus-Like Particle

List of parameters

Parameter	Meaning
beta	ratio of occupied surface area at different states
ε	porosity
ϵ_{ij}	strain rate tensor
μ	dynamic viscosity
ν	kinematic viscosity
σ_{ij}	stress tensor
τ_{ij}	viscous stress tensor
ρ	density
c	concentration
Di	diameter
D	diffusion coefficient
g	gravitational acceleration
h	height
j	flux in vector form
k	intrinsic permeability
k_a	adsorption rate
k_d	desorption rate
k_{12}	transition from state 1 to state 2
k_{21}	transition from state 2 to state 1
L	thickness
N_p	number of pleats
n	normal vector
P	pressure
p	form factor
Q	water flow rate
q_m	maximum binding capacity
S	surface
V	velocity
$V*$	interstitial velocity
v	control volume

Contents

List of Figures

List of Tables

Chapter 1

Introduction

1.1 Motivation

Filtration devices and membrane adsorbers are commonly applied in biotechnology for purifying target biomolecules at different operational conditions. Pleated filter cartridges and membrane adsorbers are constantly improved and optimized in terms of flow patterns and sizes. However, knowledge is still limited regarding the influence of specific design parameters on the performance of these devices. For example, details of how the mechanism of fleece compression influences the water flow rate can not be experimentally investigated. CFD can be used for identifying root causes of the system's behaviour. Model-based performance analysis is of particular importance since it can spare experimental costs. In addition, device development is partly based on empirical development and insights on the flow and transport mechanisms can potentially accelerate the design and optimization of such devices.

Scale-up of membrane adsorbers with data obtained from small capsules is a growing demand due to their increasing use in biopharmaceutical industry. However, overly simplified 1D models have been predominantly used in the past to model the performance of membrane adsorbers. Nevertheless, successful transfer of binding parameters can only be achieved with orthogonal modeling that allows to decouple non-ideal hydrodynamics and non-ideal binding. When this is taken into account then binding parameters estimated from a small capsule can be used in order to predict the binding

behaviour of a larger capsule. In literature several models have been used in an attempt to describe the binding mechanism of the protein to the membrane. It has been shown that the Langmuir model fails to capture the complexity of the binding process and as a result multiscale binding models have to be used. Moreover, variations in membrane capacity during manufacturing are unavoidable and only a minimum binding capacity is specified by vendors. Although an exceeded membrane capacity is beneficial for the purification process, in practice it makes scale-up more challenging.

1.2 Short history of membrane science

Membrane science emerged in 1700. The first experiments were conducted using natural membranes, such as cattle, sausage and fish casings made of gum elastics [1]. Traube firstly reported the use of an artificial membrane made by the precipitation of cupric ferrocyanide in a layer of porous porcelain [2]. In the early nineteenth and twentieth centuries membranes had scientific rather than industrial or commercial applications. In that sense, Pfeffer used this semi-porous membrane for studying the phenomenon of osmosis [3]. Fick gave the explanation of osmosis and of mass transport through membranes and related the diffusive flux to the concentration [4]. van't Hoff studied the thermodynamics perspective and formulated the osmotic pressure of solutions [5]. Nernst, Planck and Donnan interpreted theoretically the phenomena that take part in the membrane and they also focused on the membrane potentials under the existence of electrolytes [6, 7, 8]. Bechhold prepared nitrocellulose membranes that were used for filtration of macromolecules by Bachman and Zsigmondy [9, 10]. The latter, who won a Nobel Prize in chemistry for his research in colloids, introduced microfiltration in 1918. In addition, Zsigmondy was the leader of the filter production department in Sartorius Stedim Biotech. Since then membranes have developed as an economical and effective tool for separation applications in different sectors such as water preparation, sterile filtration, gas separation, haemodialysis and in biopharmaceutical industry [11].

1.3 Membranes

In downstream processing membranes are applied as a semi - permeable barrier between two phases where the mass transport takes place by a driving force [12]. The driving force can be for example pressure, concentration, electrical charge or temperature. Membranes can be classified according to their morphology as porous and non-porous. Porous membranes have large pores with sizes ranging from 0.05 micrometers to 2 milimeters and they are typically employed in microfiltration, ultrafiltration and nanofiltration processes. Non-porous membranes have pores on a molecular level. In addition, membranes can have symmetric and asymmetric structure [11]. In symmetric membranes the structure is constant everywhere. In asymmetric membranes the surface has different structure from the interior.

1.4 Filtration

Filtration is the process of separating molecules, solid parts, microorganisms or droplets from liquids with the use of a solid membrane [13]. The pressure drop across the membrane forces the liquid solution to go through the membrane where for example the solid parts are retained. Generally, membrane separations are classified based on [13]:

a) The location of particle retention

This can be at the surface (surface filtration, cake filtration) or inside the filter (depth filtration).

Depth filtration

In depth filtration the liquid goes through the filter medium that can be granular or compressible. It is a size - exclusion mechanism where the particles are retained in the filter medium, and thus, they are removed from the liquid [14]. However, usually there is an adsorption effect added i.e. diatomaceous earth in depth filter sheets. Slow sand filtration is a type of depth filtration that has been traditionally used in wastewater treatment facilities because it is suitable for removing algae, bacteria etc. Rapid sand filtration is employed prior to reverse osmosis in desalination facilities and the operating flow rate is higher than in low sand filtration [15].

Surface filtration

In surface filtration particle retention occurs at the surface of the filter based on the size-exclusion mechanism. Particles that have larger size than the pores of the membrane will be retained. In cake filtration the particles are retained from the filter medium and a cake layer is formed with the time [16]. Cross-flow filtration is another type of surface filtration where the flow is tangential to the surface of the filter in order to minimize the formulation of the cake layer [17].

b) The size of the retained solutes

That ranges from atoms to macro-molecules.

c) The mode of operation

It is continuous where the filtration is not interrupted or discontinuous where the filtration is stopped for collecting the retained solids.

d) The area of application

Membrane separations are commonly applied for example in the food industry, in air purification, in pharmaceutical and in biopharmaceutical industry.

Regarding the size of the dissolved components there are the following separation processes [18]:

1) Reverse Osmosis (RO)

This method is used for separating solutes with a molecular weight smaller than 350 Da by flowing through a membrane. The pressure drop is ranging from 20 to 80 Mpa. The liquid naturally flows from the lower concentrated solution to the higher concentrated solution. However, if the pressure is higher than the osmotic pressure then the liquid will flow from the higher to the lower concentrated solution and this procedure is called reverse osmosis. It is mainly applied for the purification of drinking water but it is also used for instance in food industry, petrochemical industry and in metal finishing industry [19].

2) Microfiltration (MF)

This method is employed for retention of particles with pores ranging from 0.025 to 10 μm and the pressure used is typically lower than 0.2 MPa. Very often microorganisms are retained as a form of particulate as in sterile filtration for example. More recently microfiltration systems are operated under constant flux instead of constant pressure drop

to increase product yield [20]. Furthermore, different modules can be employed such as rotating disk filters [21] and conical-shaped rotors [22]. Microfiltration is commonly applied in the food industry, in biotechnology or in the production of pharmaceuticals. It has also applications in drinking water filtration or in wastewater treatment plants.

3) Ultrafiltration (UF)

This method is used for separating molecules with submicron size and molecular weight between 1 and 300 kDa. The applied pressure drop is bigger than 1 MPa. It has applications in food industry, in biotechnology, in drinking water filtration, in wastewater treatment plants and in pharmaceuticals. Regarding the latter, ultrafiltration has been widely applied for clearance of DNA [23] and virus-like parts (VLP)s [24] for example.

4) Nanofiltration (NF)

This method is used for retaining particles such as viruses with molecular weight between 350 and 1000 Da at a pressure drop between 4 and 20 MPa. Some of the applications include removal of organic matter in groundwater treatment and the food industry [18].

1.5 Filtration devices

There are different construction forms of devices used in filtration such as plate and frame (cassettes), spiral wound devices or hollow fiber devices [25, 26]. Another type is filter cartridges where the membrane is arranged in pleats around a plastic core in order to maximize the surface area. Furthermore, due to the pleats a smaller footprint is obtained which is highly desirable in industry [27]. Pleated filter cartridges usually contain one or two membrane layers. In the case of two membrane layers, there are the prefilter and the main filter. A prefilter and a main filter are packed in filter cartridges with two membrane layers. The membrane layers are placed between fleece layers and are packed between two concentric cylindrical cores [28]. The outer one is the cage and it is called back-pressure screen whereas the inner is called core. The fleece layers are used for maintaining the position of the pleats.

1.5.1 Applications of filtration

Filtration is applied in different sectors ranging from food and beverage industry to gas separation and biopharmaceuticals. For example, microfiltration is in dairy industry for bacterial removal up to 99.7% or at brine treatment [29]. High flow rates can be processed if a pressure of only 30-40 kPa is applied and the properties of the milk remain the same. Ultrafiltration with the use of ceramic or polysulfone membranes is employed in cheesemaking because it leads to higher yield and better quality of the product. In addition, ultrafiltration and reverse osmosis are used in whey processing. Mavrov et al. [30] used membrane filtration for treating low-contaminated water streams that come from the food industry. In their study they used a pilot treatment plant of 2 m^3/h where pre - treatment, filtration (nanofiltration and/or reverse osmosis) and UV disinfection are applied to vapor condensate from milk industry, to water from meat processing and to water from bottle washing machines. The clean water streams had drinking quality and the vapour condensate could be used in boiler make-up water. Girard et al. [31] presented ultrafiltration and microfiltration as alternative methods for clarifying fruit juice by removing large suspended particles for example. In apple juice plants ultrafiltration exhibited certain advantages such as reduction of process times and lower energy consumption. Reverse osmosis is applied in enology in wine concentration and dealcoholisation. When the grapes contain low sugar levels reverse osmosis is used for removing water from them in order to reach the right alcohol concentration for instance. Moreover, filtration systems are also used in gas separation. Hollow-fiber modules are used in gas companies for separating hydrogen and spirally wounded modules are applied in air dehydration [32]. Polymeric membrane modules are employed in removing CO_2 and in heavy hydrocarbon recovery because they are disposable and easy to handle [33]. In addition, filtration devices are used for supplying sterile air in bioreactors [34]. Another field of applications is that of biopharmaceutical industry since most of the products can't be directly used. Shukla et al. [35] present downstream processing technology for industrial production of antibodies where filtration is used for separating cell fragments for example. Saxena et al. [36] present an overview of microfiltration and ultrafiltration processes. Microfiltration membranes are also used in sterilized filters for

bacteria removal whereas ultrafiltration membranes were used for protein concentration and exchange of buffers. Moreover, the authors reported that electrically enhanced membrane microfiltration (EMF) which is a technique where electricity is applied as the driving force showed lower membrane selectivity and higher permeate flux. Ultrasonic fields can be applied in ultrafiltration for membrane fouling control because the bubbles are formed and dissolved when the ultrasonic energy is applied to the liquid.

1.6 Membrane adsorbers (MA)s

Size exclusion is a physical retention mechanism used in filtration devices in contrast to binding which is a physiochemical retention mechanism and is used in membrane adsorbers. Apart from filtration devices membrane adsorbers (MA)s which are also referred to as membrane chromatography are used in biopharmaceutical industry. Chromatography was initially used by the botanist Mikhail Tswett [37] in 1890 for separating plant pigments of different colour. The materials that have to be separated travel with the mobile phase through the column or the membrane sheet which is the stationary phase. The name chromatography derives from two greek words “chroma” meaning colour and “graphe” that means writing. Paper chromatography is often used as an educational example. Ink is placed on a filter paper (stationary phase) which is soaked into a solvent such as alcohol or water. The ink components are separated because they travel up the filter paper with different speed [38].

Membrane adsorbers (MA)s have been introduced to the market as an alternative method to traditional column chromatography [39, 40, 41]. They are used for the purification of DNA parts and monoclonal antibodies (mAb)s or in polishing steps for removing impurities such as viral parts, nucleic acids, endotoxins or host cell proteins (HCP)s. MAs overcome the mass transfer limitations of the packed bed chromatography since convection is the main transport mechanism to the binding sites of the membrane allowing higher flow rates at lower pressure drops. In addition, MAs are often single-use devices hence the risk of cross-contamination is minimized.

1.6.1 Configurations of membrane adsorbers

Membrane adsorbers can be classified based on the flow configuration into the following: a) Axial b) Radial and c) Tangential flow devices [26] (Fig. 1.1). a) Axial flow devices are mainly used at lab scale and the membrane is usually placed in discs [42]. b) In radial flow devices the membrane is placed around a cylindrical core and it can have several geometries such as pleated sheet and spiral wound [43, 44, 45].

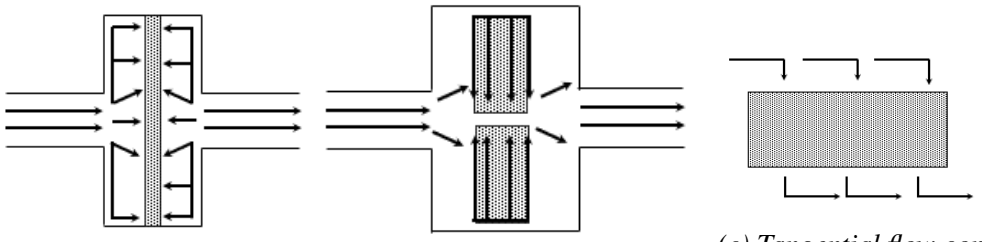

(a) Axial flow configuration *(b) Radial flow configuration* *(c) Tangential flow configuration*

Figure 1.1: Commercial membrane adsorbers in different configurations based on the flow (adapted from [26])

1.6.2 Surface functionalization

According to the retention mechanism there are different options for functionalization of the membranes.

Ion-exchange chromatography

Ion-exchange chromatography is based on electrostatic interaction between functionalized groups on the membrane and the molecules to be separated. A cation exchanger has negatively charged ligands thus positively charged molecules bind on it whereas an anion exchanger has positively charged ligands since negatively charged molecules bind on the surface. When the pI is lower than the pH, the molecules have a net negative charge and therefore they will bind to an anion exchanger. Conversely, if the pI is greater than the pH, the molecules have a net positive charge and they will bind to a cation exchanger [46]. Another classification can be made between strong and weak ion-exchangers. Strong ion-exchangers are less sensitive to pH changes. For example, quaternary ammonium (Q) ligands are strong anion-exchangers and sulfonic acid (S) are strong cation-exchangers. Weak ion-exchangers have a limited pH range and in many

applications diethylaminoethyl (DEAE) ligands are used as weak anion-exchangers and carboxyl (C) ligands serve as weak cation-exchangers [41].

Affinity chromatography

Affinity chromatography is based on specific interactions that appear between biological molecules such as binding of antigens with antibodies for example [47]. There are different types of affinity ligands such as: a) immunoaffinity b) protein A or G c) low-molecular-mass (LMM) as well as other ligands [48].

Hydrophobic interaction chromatography

Hydrophobic interaction chromatography is based on hydrophobic interaction between hydrophobic groups and molecules. Since most proteins exhibit some degree of hydrophobicity, hydrophobic interaction chromatography is commonly applied in biopharmaceutical industry [49]. Examples of hydrophobic ligands are hydrocarbon chains or rings which are attached to membranes employed in this method [41].

1.6.3 Applications of membrane adsorbers

MAs are employed in biopharmaceutical industry for the purification of biomolecules. Teeters et al. [50] used anion-exchange membrane adsorbers for capturing plasmid DNA (pDNA) parts. The maximum binding capacity of the membrane was 10 mg plasmid/ml, which is 10 times higher in comparison to packed bed chromatography. Guerrero-German et al. [51] worked on the purification of pDNA from Escherichia Coli lysate solution. They used hollow-fiber tangential filtration and membrane chromatography. They concluded that parallelization of the devices can potentially be used for purification of pDNA in the scale of kilograms. Furthermore, viral particles are essential in the fields of immunization and in gene therapy and therefore their demand is high. Endres et al. [52] used ion-exchange MAs for purification of pDNA from Escherichia Coli lysate solution. Dynamic binding capacity was 20-25 bigger and flow rates were 55-550 higher in comparison to packed-bed chromatography. Similarly, Zhang et al. [53] used anion-exchange MAs for pDNA purification at high flow rates. 10-fold concentration of pDNA was achieved and the concentration of endotoxins was 10000 times

lower at the final solution.

In addition, monoclonal antibodies (mAbs) have applications in the biomedical field for diagnosing and treating diseases like cancer or infections. Zhou et al. [54] proposed the use of an anion-exchange membrane with quaternary ammonium (Q) ligands for the purification of mAbs on large scale as a feasible choice over the traditional packed-bed columns. Ghosh et al. [48] used hydrophobic interaction membrane chromatography for separating the hIgG1-CD4 mAb from mammalian cell culture media. It was shown that under optimized operating conditions the recovery and purity are maximized up to 97%. Yu et al. [55] used cation exchange MAs and protein A affinity MAs for purifying a human mAb from transgenic tobacco. More specifically cation exchange MAs were used before protein A affinity MAs. High recovery was obtained due to low pressure drop that occurred in the cation exchange MAs. In addition, the use of the cation exchange MAs enhanced the bioburden reduction and minimized the fouling of the membrane at the protein A affinity MAs. Specht et al. [56] showed that ion exchange membranes can be used for capturing effectively the mosquito-specific parvovirus called Aedes aegypti densonucleosis virus (AeDNV). More specifically their work shows maximum viral concentration when the pH of the feed is adapted accordingly to the isoelectric point (pI) of the virus particles. Peixoto et al. [57] used MAs for purification of adenoviruses. First, the authors used cross-flow ultrafiltration membrane for clarification and concentration. Then purification with ion-exchange MAs followed by a final concentration step and the average recovery yield was 62%.

Chapter 2

Computational Fluid Dynamics (CFD)

Three conserved moieties govern the physical aspects of every fluid flow: a) mass, b) momentum, c) energy [58].
These conservation relations can be expressed by partial differential equations (PDE)s. CFD is based on numerical solution of these PDEs. The capabilities of CFD have significantly progressed over the last years due to advancements in computers which allow the solution of more complex problems that require large memory and fast processors. According to Anderson et al. [58] CFD can be located between pure experiment and pure theory. CFD can provide information on how the performance of a device is affected when the design parameters or the operating conditions are varied.

2.1 Theory

In this chapter the equations that describe flow and mass transfer will be presented. In addition, a typical simulation workflow will be described. For computing the flow profile it is important to know whether the flow is in the laminar or turbulent regime. Classification between laminar and turbulent flow was introduced by Osborne Reynolds [59]. Reynolds used a glass pipe filled with water, and the velocity magnitude of the water was controlled by a flow control valve. A streak of dyed water was added in the pipe with the pure water. For lower flow rates the dye streak is observed to follow a distinct flow path with some diffusion. For higher flow rates fluctuations of the dye are observed. In the cases of even higher flow rates the dye streak is randomly scattered in

the pipe. The Reynolds number $Re = \frac{\rho\ V\ Di}{\mu}$, where ρ is the density of the fluid, V is the average velocity, Di the diameter of the pipe and μ the dynamic viscosity, is used in fluid mechanics to distinguish between these flow regimes.

2.1.1 Laminar flow

The linear momentum of every fluid flow can be described by Cauchy's equation (eq. 2.1) [60]

$$\rho\frac{D\vec{V}}{Dt} = \rho\vec{g} + \vec{\nabla}\sigma_{ij} \tag{2.1}$$

where g is the gravitational acceleration and σ_{ij} is the stress tensor. In this thesis Newtonian fluids and incompressible flow with constant density, ρ are considered. In addition, isothermal flow is assumed which means that the dynamic viscosity, μ, and the kinematic viscosity, ν, are constant. The viscous stress tensor, τ_{ij} can be written as

$$\tau_{ij} = 2\mu\epsilon_{ij} \tag{2.2}$$

where ϵ_{ij} is the strain rate tensor. In Cartesian coordinates we can write:

$$\tau_{ij} = \begin{pmatrix} \tau_{xx} & \tau_{xy} & \tau_{xz} \\ \tau_{yx} & \tau_{yy} & \tau_{yz} \\ \tau_{zx} & \tau_{zy} & \tau_{zz} \end{pmatrix} = \begin{pmatrix} 2\mu\frac{\partial u}{\partial x} & \mu(\frac{\partial u}{\partial y} + \frac{\partial v}{\partial x}) & \mu(\frac{\partial u}{\partial z} + \frac{\partial w}{\partial x}) \\ \mu(\frac{\partial v}{\partial x} + \frac{\partial u}{\partial y}) & 2\mu\frac{\partial v}{\partial y} & \mu(\frac{\partial v}{\partial z} + \frac{\partial w}{\partial y}) \\ \mu(\frac{\partial w}{\partial x} + \frac{\partial u}{\partial z}) & \mu(\frac{\partial w}{\partial y} + \frac{\partial v}{\partial z} & 2\mu\frac{\partial w}{\partial z}) \end{pmatrix} \tag{2.3}$$

The stress tensor can be written in Cartesian coordinates

$$\sigma_{ij} = \begin{pmatrix} -P & 0 & 0 \\ 0 & -P & 0 \\ 0 & 0 & -P \end{pmatrix} + \begin{pmatrix} 2\mu\frac{\partial u}{\partial x} & \mu(\frac{\partial u}{\partial y} + \frac{\partial v}{\partial x}) & \mu(\frac{\partial u}{\partial z} + \frac{\partial w}{\partial x}) \\ \mu(\frac{\partial v}{\partial x} + \frac{\partial u}{\partial y}) & 2\mu\frac{\partial v}{\partial y} & \mu(\frac{\partial v}{\partial z} + \frac{\partial w}{\partial y}) \\ \mu(\frac{\partial w}{\partial x} + \frac{\partial u}{\partial z}) & \mu(\frac{\partial w}{\partial y} + \frac{\partial v}{\partial z} & 2\mu\frac{\partial w}{\partial z}) \end{pmatrix} \tag{2.4}$$

where the pressure, P is given by

$$P = -\frac{1}{3}(\sigma_{xx} + \sigma_{yy} + \sigma_{zz}) \tag{2.5}$$

Eq. (2.4) can be substituted into Cauchy's equation such that we get for x- component

$$\rho\frac{Du}{Dt} = -\frac{\partial P}{\partial x} + \rho g_x + 2\mu\frac{\partial^2 u}{\partial x^2} + \mu\frac{\partial}{\partial y}(\frac{\partial v}{\partial x} + \frac{\partial u}{\partial y}) + \mu\frac{\partial}{\partial z}(\frac{\partial w}{\partial x} + \frac{\partial u}{\partial z}) \tag{2.6}$$

By rearranging the viscous terms we get

$$\rho\frac{Du}{Dt} = -\frac{\partial P}{\partial x} + \rho g_x + \mu[\frac{\partial^2 u}{\partial x^2} + \frac{\partial}{\partial x}\frac{\partial u}{\partial x} + \frac{\partial}{\partial x}\frac{\partial v}{\partial y} + \frac{\partial^2 u}{\partial y^2} + \frac{\partial}{\partial x}\frac{\partial w}{\partial z} + \frac{\partial^2 u}{\partial z^2}] \tag{2.7}$$

$$\rho\frac{Du}{Dt} = -\frac{\partial P}{\partial x} + \rho g_x + \mu[\frac{\partial}{\partial x}(\frac{\partial u}{\partial x} + \frac{\partial v}{\partial y} + \frac{\partial w}{\partial z}) + \frac{\partial^2 u}{\partial x^2} + \frac{\partial^2 u}{\partial y^2} + \frac{\partial^2 u}{\partial z^2}] \tag{2.8}$$

The term in round parentheses above for incompressible fluids equals zero which is expressed by the continuity equation (eq. 2.9) [58]

$$\frac{\partial u}{\partial x} + \frac{\partial v}{\partial y} + \frac{\partial w}{\partial z} = 0 \tag{2.9}$$

As a result for the x- component we have

$$\rho\frac{Du}{Dt} = -\frac{\partial P}{\partial x} + \rho g_x + \mu\nabla^2 u \tag{2.10}$$

In a similar way we get for y- component and z- component

$$\rho\frac{Dv}{Dt} = -\frac{\partial P}{\partial y} + \rho g_y + \mu\nabla^2 v \qquad \rho\frac{Dw}{Dt} = -\frac{\partial P}{\partial z} + \rho g_z + \mu\nabla^2 w \tag{2.11a}$$

In vector notation we obtain the Navier-Stokes equations for constant viscosity and incompressible flow

$$\rho\frac{D\vec{V}}{Dt} = -\vec{\nabla}P + \rho\vec{g} + \mu\nabla^2\vec{V} \tag{2.12a}$$

$$\nabla\vec{V} = 0 \tag{2.12b}$$

The Navier-Stokes equations are a set of non-linear second-order partial differential equations for which analytical solutions can be obtained only for very simple geometries [61]. On the left hand side of eq. (2.12a) there are the inertial forces whereas on

the right hand side there are the pressure and viscous forces.

2.1.2 Boundary Conditions

No-slip boundary conditions are used where the fluid contacts a wall and the fluid velocity is zero at walls [61]. Elsewhere inlet or outlet boundary conditions are defined.

2.1.3 Turbulent flow

At high flow rates the Navier-Stokes equations fail to accurately describe the fluid flow. In this case Reynolds-Averaged Navier-Stokes (RANS) equations are used in this study which consider local fluctuations in a time-averaged way [62]. In this study the yPlus algebraic model was used which was introduced by Prandtl. In this approach the mixing length is proportional to the mean free path length of the molecules in the fluid. The algebraic equations that calculate the turbulence viscosity are based on the local fluid and the distance to the nearest wall [63].

2.1.4 Flow in porous media

The flow in porous media is described by a combination of Darcy's law [64] and the Navier-Stokes equations resulting in the Brinkman's equations [65].

$$\rho\frac{D\vec{V}*}{Dt} = -\vec{\nabla}P + \rho\vec{g} + \mu\nabla^2\vec{V}* - \frac{\mu}{k}\,\vec{V}* \tag{2.13a}$$

$$\nabla\vec{V}* = 0 \tag{2.13b}$$

Here, $V^* = \frac{V}{\varepsilon}$ is the interstitial velocity, ε is the porosity and k is the intrinsic permeability. Brinkman's equations consider Darcy's law in accounting for dissipation of kinetic energy by viscous shear similarly to the Navier-Stokes equations [66].

2.2 Mass transfer

In this study mass-transfer occurs through convection and diffusion. Both are time-dependent phenomena. Convective mass transfer occurs because of the bulk motion

of a fluid [67]. In the present study diffusion describes the net flux of molecules from regions with higher to regions with lower concentration [68].

2.2.1 Conservation of mass

From the conservation law for a control volume, v we have

$$\frac{d}{dt}\int c\, dv = -\int j\, n\, dS \tag{2.14}$$

where c is the concentration, j is the flux in vector form, n the vector normal to the surface S. Using the transport theorem [69] for the left hand side of the equations and the divergence theorem [70] for the right side of the same equation, we obtain

$$\int_{v(t)} (\frac{\partial c}{\partial t} + \nabla(cV) dv = -\int_{v(t)} \nabla j\, dv \tag{2.15}$$

For that to hold for any control volume

$$\frac{\partial c}{\partial t} + \nabla(c\, V) = -\nabla j \tag{2.16}$$

For constant diffusivity and using Fick's law ($j = -D\nabla c$) [71] we get

$$\frac{\partial c}{\partial t} + \nabla(c\, V) = D\nabla^2 c \tag{2.17}$$

where D is the diffusion coefficient and the term $\nabla(cV)$ is convection in our case and eq. 2.17 can be written

$$\frac{\partial c}{\partial t} + V\nabla c + c\nabla V = D\nabla^2 c \tag{2.18}$$

The term $c\nabla V$ equals to zero when the velocity doesn't change over the time and therefore we obtain

$$\frac{\partial c}{\partial t} + V\nabla c = D\nabla^2 c \tag{2.19}$$

In this study, binding processes have also to be considered which are described by adding source and sink terms to the mass balance equation

$$\frac{dc}{dt} = -V\nabla c + D\nabla^2 c - \frac{dq}{dt} \tag{2.20}$$

2.2.2 Numerical solutions

In the present work CFD simulations are performed using COMSOL Multiphysics 5.3 which is commercial software based on the finite element method. In this method the computational domain is divided into a set of smaller domains which are called finite elements. On every element the solution is approximated using algebraic polynomials. Then the domains are assembled in order to have one solution for the total geometry [72]. In this study, quadratic basis functions are used for the velocity and linear basis functions for the pressure. For solving the mass transfer studies also linear basis functions were used.

2.3 Simulation Workflow

A typical computational modeling and simulation procedure has the following steps:

1) Creation of computational geometry

The geometry can generally be created in COMSOL but in special cases other software are required such as computer aided design (CAD) software for example. The geometry has to be only as complex as needed since extra details will cause unnecessary computational complexity. Hence symmetries are exploited when the computational geometries allow. For example, rotational symmetry will reduce a three dimensional model to two dimensions and mirror symmetry halves the geometry in the same dimensions.

2) Mesh generation

In order to discretize the computational domain in space it is necessary to generate a mesh. The models are usually meshed in COMSOL but other software can also be used for example the Gmsh. Different types of elements are available such as triangular elements, tetrahedral elements, pyramids, prisms or hexahedral elements. When a mesh follows a regular pattern is structured. Such meshes often yield faster conver-

gence but they are challenging to create for complicated geometries. Therefore unstructured meshes are most commonly applied [73]. Another option is to generate a hybrid mesh which usually consists of a structured boundary layer mesh combined with an unstructured volume mesh. In this study triangular elements are used in 2D studies, and tetrahedral or hexahedral elements are used in 3D studies. Typically the mesh is generated from lower to higher topologies which means that first the edges are meshed, then the faces and at last the volumes. The mesh density should be higher where the velocity gradient, the pressure gradient and the concentration gradient are larger. These gradients are expected to be larger in narrow gaps and channels of the geometry.

3) Choice of modules (Multiphysics)

The hydrodynamic simulations can be set up and solved previously to mass transfer simulations. The calculation of the flow velocity profiles is time independent because the concentrations are low and the velocity both at the inlet and outlet does not change over time. The obtained solution enters the mass transfer simulations. In COMSOL the hydrodynamic profile is calculated by the use of the laminar flow or turbulent flow module and for the mass transfer simulations the transport of diluted species module is used.

4) Definition of boundary conditions

In this study no-slip boundary condition are applied at walls and elsewhere inlet and outlet conditions are used. Symmetry boundaries are applied in some cases in order to reduce the computational effort. In addition, periodic boundary conditions are used in structures that exhibit spatial periodicity.

5) Numerical solvers

The resulting algebraic problems can be solved with direct and iterative solvers. In the present study the direct solver 'MUltifrontal Massively Parallel sparse direct Solver" (MUMPS) and the Backward differentiation formula (BDF) are used. MUMPS is a parallel solver based on LU decomposition and it uses a version of Gaussian elimination for large sparse systems of equations [74]. In addition, the solver is capable of solving well-conditioned finite element problems. MUMPS is an out-of-core solver which means that it can store parts of the data on the hard drive when the memory of the computer is full without losing efficiency in performance. The spatially discretized dif-

ferential equations are integrated over time using a backward difference formula (BDF). The BDF is a numerical integration method that approximated the time derivative of a function at a time *t* using information from previous time steps with variable step width and order.

6) Postprocessing

After numerically solving the model equations, the results are visualized and evaluated. Plots of concentration over time can be created in COMSOL but in this study the data sets were exported and the plots are created in MATLAB in order to compare simulation results to experimental breakthrough curves. Plots of the simulated velocity magnitude are created for all the studied models. For the 3D geometries cut planes are used for creating 2D cross sectional plots of the simulated velocity magnitude. In addition, arrow plots that show the direction of the velocity and contour plot of the pressure shows the minimum and maximum values are also created.

Chapter 3

Filtration Cartridges

3.1 Introduction

Filtration cartridges are used for removing impurities found in fluids and gases. For example, they are used in potable water purification, in wastewater treatment and in beer production. As another example, fluids are filtrated in aeronautical applications [75]. Pleated filter cartridges that are studied in this work are commonly employed at different stages in the pharmaceutical industry. For instance they are used for buffer filtration, for sterile filtration prior to the formulation of the product and also at the final step when filling the drug into the vials.

Capsules typically consist of two parts [76]: 1) the housing 2) the filter cartridge. The filter cartridge is placed in the middle of the housing which is made of stainless steel. Inlet and outlet pipes are attached to the bottom housing. Inside the filter, one or more membrane layers are arranged in pleats around a cylindrical core. Moreover, fleece layers are placed between the membrane layers. The upstream fleece layer protects the membrane during the assembly and keeps the pleats at a fixed position. In addition, it can also serve as a prefilter in order to prolong the service life of the membrane [77]. The downstream fleece layer also holds the membrane layers in place. An important function of both fleece layers is to maintain the gaps between the pleats. Pleated filter cartridges with different combinations of membrane and fleece layers are commercially available. The fleece layers are typically made of polyester or polyolefines

and some typical membrane materials are polyethersulfone, cellulose acetate, cellulose nitrate, polyamide and polyvinylidene fluoride [77]. Membranes are often chemically treated at their surface for enhancing their hydrophilicity, wettability and pleatability [77]. The two concentric cylindrical plastic parts that hold the pleated structure together. The cage prevents damage of the pleated structure during the installation. The distance between the outer and the inner cylinder defines the pleat height. At the top and bottom of the filter cartridges there are end caps. The lower end cap serves for connecting the filter cartridge to the housing and on the upper end cap another filter cartridge can be studied.

Usually the plastic parts are made from polypropylene [77]. The fluid flows from the outer periphery of the plastic cylinder through the porous media and it is collected in the middle of the inner core. Fig. 3.1a shows the pleated filter cartridge which is considered as standard configuration in this study. It is 10 *inches* long and has a filtration area ranging from 0.5 m^2 to 0.8 m^2. In general, the height of a pleated filter cartridge can be from 1 to 40 *inches* and the filtration area is within a range of 0.015 m^2 to 36 m^2 [77]. Pleated filter cartridges have the following advantages [77]: The membrane is pleated in order to achieve a maximum filtration area which enables processing of higher flow rates and higher concentration for longer time. This results in long lifetime of such filter cartridges. In addition, when maximum filtration area is packed into a small volume the footprint of the unit is reduced which is highly desirable in industry. The standard pleated filter cartridge is shown in Fig. 3.1. It has three domains 1) upstream of the medium 2) the filter medium 3) downstream of the filter.

The porosity, ε and the intrinsic permeability, k are the two material properties that characterize the membranes. The most important design parameters are the pleat height, the pleat type and the pleat packing density. The pleat packing density depends on the number of pleats. An increased pleat packing density can cause compression of the porous media, pleat deformation and/or crowding [78]. Fig. 3.2a shows the standard star pleat type which is found in many commercial filter cartridges whereas Fig. 3.2b shows twin pleats. In general, manufacturers are interested to know how the flow rate, the pressure drop and the lifetime of pleated filter cartridges depend on:
a) the number of fleece and membrane layers

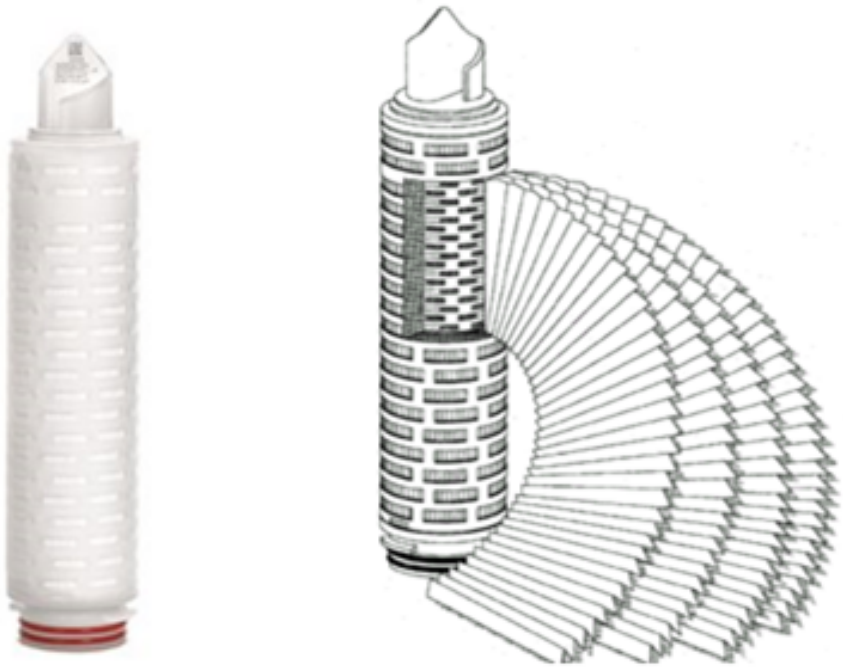

(a) Filter cartridge *(b) Schematic diagram*

Figure 3.1: Pleated filter cartridge (courtesy of Sartorius Stedim Biotech)

b) the thickness of the fleece and membrane layers

c) the geometric arrangement i.e. pleat type, pleat height and pleat density

d) the material properties of the membranes, i.e. the porosity, ε and the intrinsic permeability, k

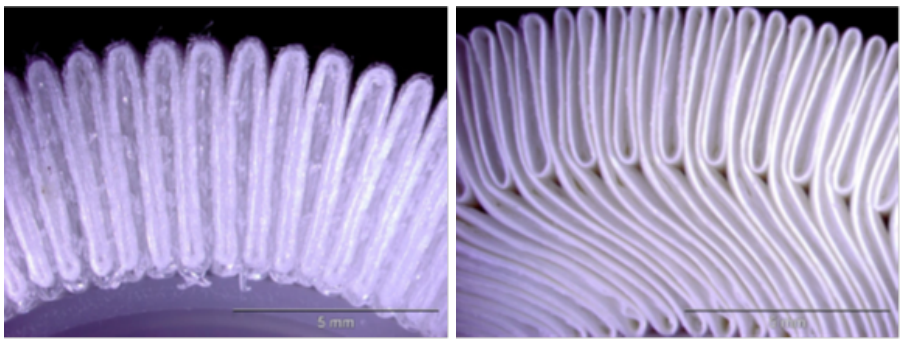

(a) Star pleat type *(b) Twin pleat type*

Figure 3.2: Microscopic images of star and twin pleats (courtesy of Sartorius Stedim Biotech)

3.1.1 Literature review for pleated filtration cartridges

Bioprocess industry

Pleated filtration cartridges are used in the biotechnology [79]. For example, prior to virus filtration pleated filter cartridges in dead- end filtration mode can be employed for aggregate removal [80]. In filtration area membranes with pore size of up to 5 μm are typically used as prefilters and pore sizes of 0.2 μm and 0.1 μm serve as final filters. The appropriate pore size of the membranes depends highly on the application. For example, in beverage industry final filters of 0.65 μm are employed for yeast filtration. Their main use is the bioburden reduction in order to eliminate the risk of contamination in the final solution [79, 81]. Pleated filters are also used in blood fractionation or for blood transfusion [82].

Environmental virology

Another area where filter cartridges are extensively applied is that of environmental virology. Enteric viruses are present in water and can be responsible for waterborne diseases [83]. Some of the methods used for removing viruses from water employ adsorption to a filter and elution with an adjusted pH. Viruses are typically negatively charged and therefore if a filter carries a negative charge then the water sample has to be preconditioned. Alternatively, positively charged filters are used. Virosorb 1 MDS has been largely employed and as a cheaper alternative NanoCeram filters are also used [83]. For the recovery of viruses from filters in organic and inorganic solutions are used.

Virus concentration

Concentration is important for decreasing the volume of the eluate in order to improve the detection of the viruses [83]. Farrah et al. [84] reported the concentration of polioviruses in tap water at a pH of 3.5 with addition of $AlCl_3$. The authors used 10-inch fiber-glass depth cartridges and electronegative 10-inch epoxy-fiberglass pleated filters in series at high flow rates of up to 38 L/min. Adsorption occurred at a pH of 3.5 and for the elution glycine buffer with a pH of 11 was used. The average viral recovery was 40-50% in a sample of 1900 L of water. Similarly, Gerba et al. [85] used 10-inch fiber-glass depth cartridges and electronegative 10-inch epoxy-fiberglass pleated filters at high flow rates of up to 37.8 L/min for concentration of polioviruses. They tested tap

water, waste and marine waters following the same procedure as Farrah et al. [84]. The average recovery of poliovirus 1 was 52% from a sample size of 472 L of tap water, 53% from 378 L of wastewater and 50% from 19 L *to* 190 L of seawater. In addition, Preston et al. [86] used electronegative epoxy-fiberglass pleated filter cartridges for recovery of coliphages and enteroviruses (poliovirus 1 and coxsackievirus B5) from tap water. The cartridge filters were modified with cationic polymers. At a pH of 8.1 the modified filter cartridges adsorbed about 96% of viruses and the recovery was about 99% in contrast to 20% and 18% when the filter cartridges were not modified. Shields et al. [87] studied the recovery of poliovirus 1, coxsackievirus B3, B4, B5 and echovirus 1 from 114 L of tap water. The pH of water was 3.5 with the addition of CH_3COOH. The viruses were adsorbed to electronegative 10-inch epoxy-fiberglass pleated filter cartridges and eluted with sodium trichloroacetate at pH 9. For the concentration of viruses 47 *mm* asbestos filter cartridges were used and an average virus recovery of 45% was achieved in 16 *ml* sample. Negatively charged filter cartridges offer high recovery of viruses, they are inexpensive and commercially avaible from different vendors. However, the pH of the water samples has to be adjusted which can be difficult when large volumes are processed. Surface modification of the membranes can be also considered but variations regarding the surface charge are observed [88]. In the following studies positively charged pleated filter cartridges (NanoCeram) with alumina nanofibers were used. Karim et al. [89] studied the concentration of poliovirus, coxsackievirus B5, and echovirus 7 from tap water. The authors used water samples of 100 L at a pH ranging from 6 to 9.5 and at flow rates ranging from 5.5 L/min to 20 L/min. The average adsorption to the filters was 84% and two elutions were performed. The average recoveries were 54% for poliovirus, 27% for coxsackievirus and 32% for echovirus 7. Similarly, Ikner et al. [90] focused on the concentration of viruses from tap water. MS2 coliphage, poliovirus 1, echovirus 1, coxsackievirus B5 and adenovirus 2 were tested in water samples of 20 L. Average viral retention was 99% and average recoveries were 45-56 % for MS2 coliphage, 66% for poliovirus 1, 84% for echovirus 1, 77% for coxsackievirus B5 and 14% for adenovirus. Furthermore, Gibbons et al. [91] studied the recovery of adenovirus, norovirus and male-specific coliphages from seawater in samples of 40 L. The average adsorption to the filters of 98% was observed for adenovirus

and male-specific coliphages. Moreover, average recoveries of 96% were shown for norovirus and male-specific coliphages.

Virus filtration

Pleated filter cartridges have been also used in virus filtration. Oshima et al. [92] used pleated filter cartridges in order to remove viruses from biological fluids. The authors compared virus removal of 47 *mm* flat sheet discs to pleated filter cartridges. The latter can process considerably large sample volumes faster than the 47 *mm* flat sheet discs. Both configurations contained the 3 layers of polyvinylidene fluoride (PVDF) membrane. The results from both filtration systems were similar and it was shown that viruses with small sizes were removed. Additional experiments showed that the average recovery of albumin and immunoglobulin IgG was 90%. Liu et al. [93] performed studies with filters for eliminating the danger of contamination in bioreactor. The authors used 47 *mm* flat sheet discs and 10 *in*. pleated filter cartridges for viral retention based on the size-exclusion mechanism. Viral filtration greater than 3 log reduction value (LRV) was achieved for 20 nm minute virus of mice and LRV greater that 4.5 was obtained for 28 nm bacteriophage ΦX174. In addition, removal greater than 8.8 LRV was shown for the mycoplasma Acholeplasma laidlawii and greater than 9.2 for the bacteria Brevundimonas diminuta. A pleated filter cartridge processed a volume of 800 *L* in 2 *h* whereas a 47 *mm* flat sheet disc exhibited equivalent results but for smaller volumes.

Performance analysis

Several studies have focused on the performance of pleated filter cartridges. For example, Brown et al. [27] studied how the pleating influences the performance of a cartridge in terms of water flow rate at a given pressure drop. They compared pleated filter cartridges to flat sheet discs with the same properties. The experiments resulted in 50% lower flow rate for the commercial pleated filter cartridges. When the pleated filter cartridges have a reduced pleat packing density and smaller pleat height then their performance is similar to that of the flat sheet discs. The results obtained with water were compared with additional experiments with a yeast suspension. The aim was to assess the accessibility of particles at the base of the pleat. The results revealed that for greater pleat heights and higher pleat packing densities the yeast didn't access the pleats due

to crowding phenomena. The authors concluded that in this study an increased pleated membrane area didn't help to increase the performance in terms of water flow rate.

In addition, Brown et al. [94] manufactured disposable scale-down pleated membrane cartridges. The prototypes were used to predict the performance of scaled-up devices because the assessment of flat sheet discs doesn't provide accurate information. The scale-down pleated filter cartridges had the same design properties with the larger scale cartridges (pleat packing density, pleat height and pleat type) but a reduced active membrane area. Experiments with two different feedstocks were carried out. The results revealed a successful prediction of flow rate and protein transmission for the scaled-up pleated filter cartridges.

Model-based performance analysis

Several model-based methods have been reported in literature in order to predict the performance of pleated filtration cartridges. Chen et al. [95] studied pleated filter panels with six commercial media used for air filtration. The design parameters which are the pleat height, the pleat number and the pleat type were optimized. A 2D model of a rectangular pleat was solved using the finite element method for different geometries. It was shown that for every cartridge configuration there is an optimum pleat count that minimizes the pressure drop. Their model was validated against experiments of Yu et al. [96].

Furthermore, Theron et al. [97] focused on the impact of the pleat geometry on velocity field and on pressure drop in fibrous filters for air applications. Their model consists of a half pleat in three dimensions with varying pleat widths and heights. Two turbulent models were implemented and the results revealed that the minimum pressure drop is achieved by a decreased pleat height and an increased pleat width. The simulations were compared with experiments from prototypes.

Chen et al. [98] studied the impact of pleat shape on the performance of reverse pulsed-jet cleaning of filter cartridges. They aimed at the enhancement of the cleaning efficiency and quality. Four different pleat shapes were studied i.e. V-shaped, convergent trapezoidal, divergent trapezoidal and rectangular shapes. 3D models with computational geometry of one pleat were solved using the finite volume method. The transient flow velocity profiles and the calculation of the pressure fields revealed that

the trapezoidal shaped pleats are suitable for higher cleaning efficiency. Subrenat et al. [99] focused on a pleated filter packed with activated carbon cloth which is used for the removal of volatile organic compounds. The model consists of one half pleat in three dimensions and the solution is calculated using the finite volume method. They analyze the aerodynamic behaviour with respect to the fluid flow and the pressure drop and they have case studies with different number of pleats.

Moreover, Wakeman et al. [78] performed studies for laminar and incompressible flow in a pleated filter cartridge. Their two dimensional computational domain consists of two pleats and the plastic cage was neglected. The solutions were obtained using the finite element method. In addition, a second model that accounted for the membrane compression and the loss of filtration area was developed. The combination of both models showed good agreement with the measurements. When the height of the pleat increases then the created space can lead to deformation of the pleats at the periphery of the cartridge.

Nassehi et al. [75] studied pleated filtration cartridges for the filtration of hydraulic fluids used in aeronautical applications. The authors studied four different models with increasing level of complexity and the solutions were obtained with two different finite element methods. The results from the two different solution schemes were compared with each other but not with experimental data. Understanding hydrodynamic effects in such devices is a key prerequisite for transferring membrane related data across devices with different arrangements of the same membrane type. This particularly applies to scaling from small discs to large filter cartridges [100].

3.1.2 Scope of this study

The scope of this study is to help answering questions regarding the performance of star pleated cartridges with the use of CFD modeling. The performance indicator here is the water flow rate as a function of the pressure drop. The influence of the pleat thickness, the pleat height and the pleat density on the water flow rate is assessed. The impact of the plastic cage and of the fleece layer is quantified. In the CFD simulations all the required parameters are known except for the permeability of the fleece layers. The lat-

ter wasn't experimentally determined and hence the values are estimated such that the simulated water flow rate simulations match the corresponding measurements. Transfer of the estimated permeabilities across different cartridges with similar membrane properties in order to achieve predictive simulations is also studied. Seven pleated filter cartridges are analyzed whose configurations are shown in Tab. 3.1 and a table with more detailed characteristics of the cartridges is shown in the Appendix (Tab. 6.1). Filter A is a standard commercial cartridge whereas the others are prototypes. All cartridges and measurements were provided by Startorius Stedim Biotech.

3.2 Pleat Geometry

In order to quantitatively predict the performance of a filter cartridge an accurate reproduction of the geometry is crucial. Four different geometry reconstruction methods are developed and compared based on Fig. 3.5 for the standard cartridge A. They are then applied for the other cartridges. For the pleat reconstruction a 2D representative cross section is used.

3.2.1 Image Analysis Design

In the image analysis method the pleat geometry is manually recreated using Inkscape which is a vector graphics editor. The first step is to import a high quality microscopic image and to scale it to its real dimensions. Secondly, the image is set as background by reducing the contrast. On the foreground Bezier curves are used to reproduce the center line of each pleat. The Bezier curves are created from nodes which are manually placed and adjusted in order to accurately reproduce the curvature and the position of each pleat. Pleats with a finite width are created using the "draw to path" command. This procedure can result in some defects in a few nodes which have to be manually removed. Otherwise, they can lead to some local distortion of the pleat design especially at the regions close to the bends. In addition, two concentric circles that serve as the inlet and outlet boundaries of the computational geometry are created (Fig. 3.4). High quality microscopic images often provide information only on a sector (Fig. 3.2a), hence side

Table 3.1: Specifications of the studied cartridges

Cartridge Units	Number of pleats	Pleat height *mm*	Core diameter *mm*	Thickness of prefilter μm	Thickness of main filter μm	Thickness of fleece upstream μm	Thickness of fleece downstream μm	Water flow density of prefilter $\frac{mL}{(min\ cm^2\ bar)}$	Water flow density of main filter $\frac{mL}{(min\ cm^2\ bar}$
A	104	11.5	44	163	150	300	300	83	25
B	138	11.5	44	155	150	155	155	137	25
C	95	11.5	44	160	153	260	260	91	25
D	102	11.5	44	160	153	260	260	91	25
E	110	11.5	44	160	153	260	260	91	25
F	82	11.5	44	–	160	600	600	–	257
G	57	18.5	28	–	160	600	600	–	257

boundaries are needed to complete the computational domain. For the sake of studying a full cross section of the cartridge periodic boundary conditions are applied at the left and right boundaries of the sector. The position of the membrane where it is cut through by the side boundaries has to be the same at both sides in order to apply periodic boundary conditions. Therefore it has to be manually adjusted. The geometry is saved as a DXF file which is then imported to COMSOL. Within COMSOL boundary conditions are defined. The inlet is defined at the outer periphery of the circle and the outlet at the inner core. In the case where only a sector is simulated, periodic boundaries are applied at the sides.

The image analysis method can also be used for recreating the fleece layers which are used for maintaining the distance between the pleats. After the membrane pleats have been created they are set as background and the procedure that has been already explained is repeated for the fleece layers.

3.2.2 Regular Generic Design

In contrast to the image analysis design, in this method all pleats are considered the same and are created by a mathematical function, eq. (3.1) in four steps (Fig. 3.3). The function takes into account the physical properties of the pleats, such as the number of pleats, N_p, the curvature of the pleats and the radial extension between r_2 and r_3 (Fig. 3.4). First, using eq. (3.1a) a periodic curve, h_1 is created with a certain number of pleats. Secondly, the curvature of the pleats can be adjusted by the form factor, p in eq. (3.1b). Then the resulting function, h_2 is stretched and shifted depending on the radial position of the pleats, h_3 in eq. (3.1c). As a last step the shape of the pleats is transformed into radial coordinates, x and y, eq. (3.1d). These functions are implemented in MATLAB and the result is imported to Inkscape. In Inkscape the procedure that has been already described is followed from the point where the two concentric circles are created. This method doesn't require a microscopic image as long as the user knows the pleat thickness, the pleat number and the pleat height. A further advantage is that a full cross section can always be created.

$$h_1 = sin(\phi N_p) \quad \text{with} \quad \phi \in [0, 2\pi] \tag{3.1a}$$

$$h_2 = sign(h_1)\, abs(h_1)^{1/p} \tag{3.1b}$$

$$h_3 = r_2 + (r_3 - r_2)\,(1 + h_2)/2 \tag{3.1c}$$

$$x = h_3\, sin(\phi) \quad \text{and} \quad y = h_3\, cos(\phi) \tag{3.1d}$$

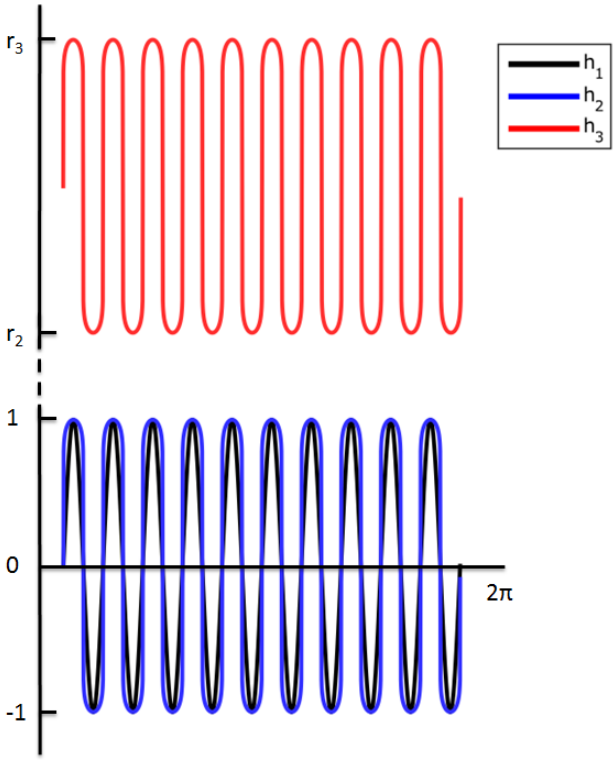

Figure 3.3: Stepwise definition of mathematical function for membrane curvature in generic pleat design where h_1 is a sinus function, h_2 is used for adjustment of the pleat widths and h_3 is used for shifting and stretching the pleats along the radius

3.2.3 Deterministic Irregular Design

The idea behind this method is to combine the advantages of the previous methods. The regular generic design can be used for reconstructing the pleat geometry in a very short time whereas the greatest advantage of the image analysis method is the accuracy. In the deterministic irregular design, the microscopic image is used for measuring the exact

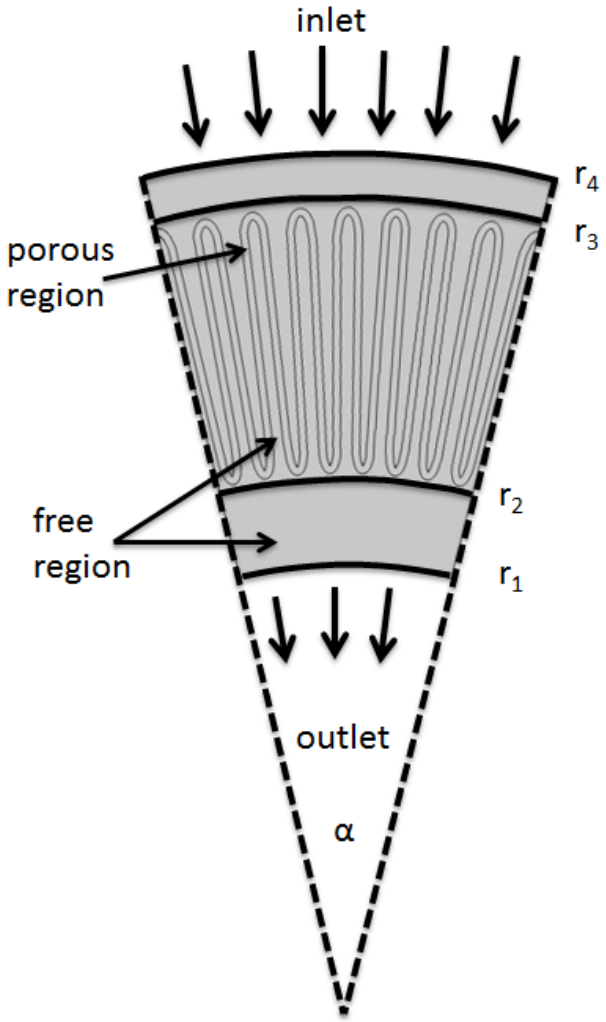

Figure 3.4: Generic sketch of computational geometry

width of each pleat. The measured widths are manually adjusted in the regular generic design method such as to match the pleat widths from the microscopic image. The result is imported in Inkscape the same procedure is followed as in the regular generic design. A potential limitation of this method and of the image analysis method is that in most cases high quality microscopic images provide information only on a sector of pleats.

3.2.4 Randomized Irregular Design

The randomized irregular design method builds on the deterministic irregular design method. The measured pleat widths are statistically analyzed in terms of mean values

and variances. Correlations of the width of neighbouring pleats are taken into account in the statistical analysis. Random numbers that follow the distribution are generated and are used for creating the pleats. With the randomized irregular design reconstruction of a full cross section is possible. The randomized irregular design can be applied for analysing the effect of natural variations for the same device.

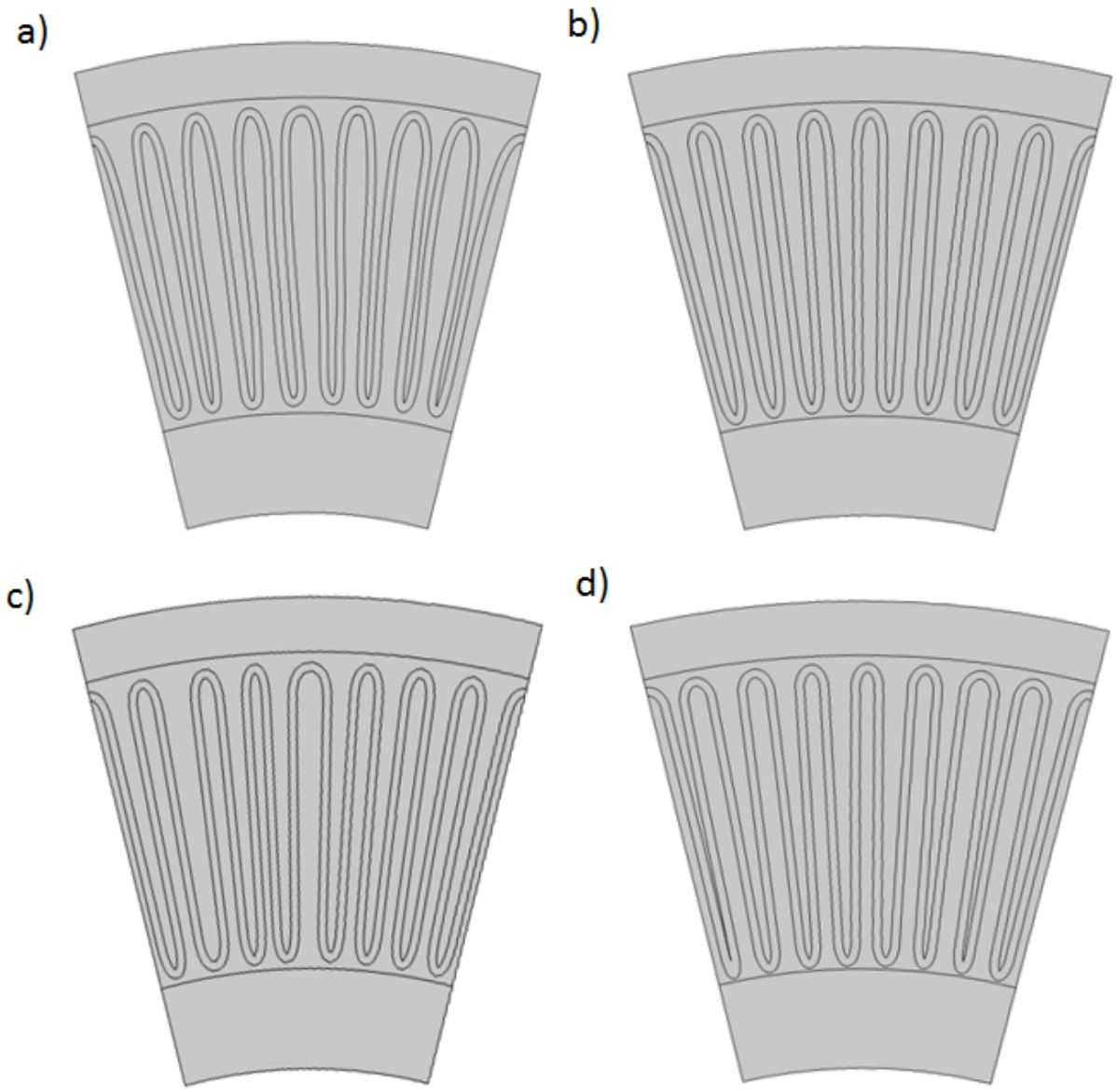

Figure 3.5: Pleat geometry as reconstructed by a) image analysis, b) regular generic, c) deterministic irregular, and d) randomized irregular design

3.3 Porous media

The membrane parameters that are experimentally determined are the porosity, ε and the water flow density, Q, with unit $ml/(min\ cm^2\ bar)$. The water flow density is measured using membranes in a flat sheet arrangement with surface area S and thickness L at a defined pressure drop ΔP. However, in COMSOL the membrane parameters are porosity, ε and the intrinsic permeability, k with unit m^2. The latter can't be directly measured but it can be calculated from the water flow density using Darcy's law [64], eq. 3.2.

$$Q = \frac{S\ k\ \Delta P}{\mu\ L} \tag{3.2}$$

In this study, μ is the dynamic viscosity of pure water. For the cases where the cartridge has only one membrane layer the intrinsic permeability can be directly calculated. However, in some other cases there are two membrane layers, the pre and the main filter. There are two options for modeling double membrane layers. First, both layers are separately modeled with thicknesses L_1, L_2 and permeabilities k_1, k_2. Alternatively, the double layer can be treated as a homogeneous region with total thickness of $L_{total} = L_1 + L_2$ and permeability k_{total}. The total permeability k_{total} in the membrane stack can be calculated using Darcy's law based on the equality of water flow densities, $Q_{total} = Q_1 = Q_2$ and on the additivity of pressure drops, $\Delta P_{total} = \Delta P_1 + \Delta P_2$:

$$\Delta P_{total} = \frac{Q_{total}\ \mu\ L_{total}}{S\ k_{total}} \tag{3.3a}$$

$$\Delta P_1 = \frac{Q_1\ \mu\ L_1}{S\ k_1} \tag{3.3b}$$

$$\Delta P_2 = \frac{Q_2\ \mu\ L_1}{S\ k_2} \tag{3.3c}$$

$$\frac{Q_{total}\ \mu\ L_{total}}{S\ k_{total}} = \frac{Q_1\ \mu\ L_1}{S\ k_1} + \frac{Q_2\ \mu\ L_1}{S\ k_2} \quad \text{(additivity of pressure drops)} \tag{3.3d}$$

$$\frac{L_{total}}{k_{total}} = \frac{L_1}{k_1} + \frac{L_2}{k_2} \quad \text{(equality of water flow densities)} \tag{3.3e}$$

$$k_{total} = \frac{L_1 + L_2}{(\frac{L_1}{k_1} + \frac{L_2}{k_2})} \tag{3.3f}$$

The membrane properties of the analyzed cartridges are shown in the table below (Tab. 3.2). The porosity ε of the membrane and the fleece layer is the same in all studied cartridges.

Table 3.2: Membrane properties of the studied cartridges

Cartridge Units	ε %	L_{total} *mm*	k_1 m^2	k_2 m^2	κ_{total} m^2
A	79	313	$22.5\ 10^{-15}$	$6.25\ 10^{-15}$	$10.0\ 10^{-15}$
B	79	305	$35.4\ 10^{-15}$	$6.25\ 10^{-15}$	$10.8\ 10^{-15}$
C	79	313	$24.3\ 10^{-15}$	$6.37\ 10^{-15}$	$10.3\ 10^{-15}$
D	79	313	$24.3\ 10^{-15}$	$6.37\ 10^{-15}$	$10.3\ 10^{-15}$
E	79	313	$24.3\ 10^{-15}$	$6.37\ 10^{-15}$	$10.3\ 10^{-15}$
F	85	160	–	$68.5\ 10^{-15}$	$68.5\ 10^{-15}$
G	85	160	–	$68.5\ 10^{-15}$	$68.5\ 10^{-15}$

3.4 Plastic cage

The pleated membrane and fleece layers are supported by the plastic cage. The plastic cage serves as a screen for back pressure. The plastic cage consists of two concentric cylinders that have several open windows through which the liquid enters and exits. The windows are arranged in rows and symmetry allows to reduce the model to only one ring. In contrast to the geometry of the pleats where computer aided design (CAD) files were not available, the CAD files of the plastic cage with an inner core diameter of 44 *mm* were provided by Sartorius Stedim Biotech. The designs are imported to COMSOL and a full 2D cross section of the pleated membrane is placed in the center and extruded to the third dimension (Fig. 3.6). In the typical flow path of the liquid enters from the front region A goes through the windows to the porous regions. Then the filtered liquid, travels through the exit windows and is collected at the back side of region B.

3.5 Water flow measurement

All water flow experiments have been performed by Sartorius Stedim Biotech. Fig. 3.7 shows a schematic representation of the experimental procedure. A fresh 10” cartridge

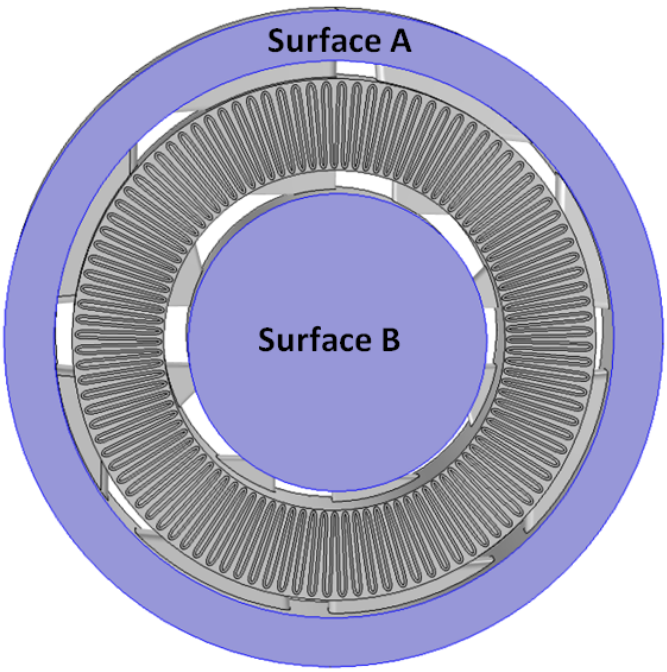

Figure 3.6: 3D computational geometry

is wetted for 90 *s* under a pressure drop of 0.3 *bar* prior to the measurement. The experiment is performed with mains water that recirculates in the 300 *L* tank. At the beginning of each wetting cycle, the vent valve on top of the cartridge housing is opened until remaining air entrapped in the filter housing doesn't exit from the cartridge. The experiments are performed directly after the wetting procedure without breaks in order to avoid air entrapment. Each pressure step is applied for 300 *s* at different pressure drops of for example 2.0 *bar*, 1.5 *bar*, 1.0 *bar*, 0.5 *bar*, 0.3 *bar*, 0.2 *bar* and 0.1 *bar*. The pressure drop is measured by sensors and the water flow is recorded by a flowmeter. The pressure at the inlet is controlled by a controller in a rotary pump and at the outlet is open at atmospheric pressure. A heat exchanger with cooling water (20^o *C*) is used for removing excess heat caused by friction in the filter cartridge and in the test system.

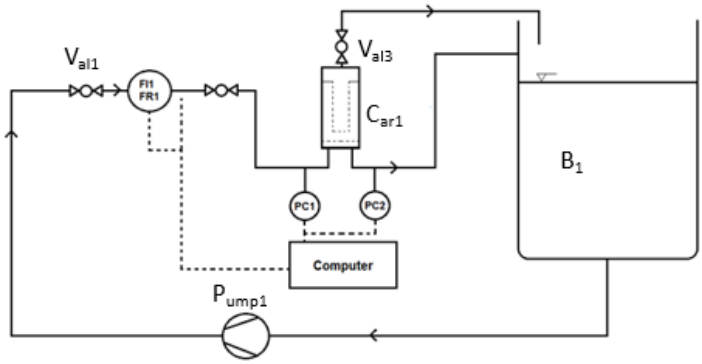

Figure 3.7: Experimental setup to determine the water flow density. C_{car1}: cartridge, B_1: water reservoir, P_{ump1}: rotary pump, $V_{al1} - V_{al3}$: valves, FI1: flowmeter, PC1 - PC2: pressure sensor (courtesy of Sartorius Stedim Biotech)

3.6 Results & Discussion

3.6.1 Numerical accuracy

Mesh independency studies have been performed for all the models in order to define the appropriate mesh density. The models were considered mesh independent when the difference between water flow rate from models with different mesh size was smaller than 1%. For example, for model A in 2D at a pressure drop of 0.1 *bar* the water flow rate of the cartridge was 9.718 m^3/s with a mesh size of 150.000 elements in contrast to 9.717 m^3/s when 250.000 mesh elements are used. The relative error was $RE = \frac{9.718-9.717}{9.718} * 100$ = -0.01 % and therefore the model with the 150.000 elements is used in order to reduce the computational effort. The mesh size was determined for every cartridge with the same manner and it is shown in Tab. 3.3. In addition, the mesh density between models which are a sector of a cartridge and full circle models should be approximately the same. For example, for cartridge A the 2D model has 10 pleats and the mesh size is 150.000 elements. The 2D model of cartridge C has approximately 100 pleats and a mesh size of about 1.700.000 elements which is proportional to the size of the model. For the 2D meshes triangular elements were used and tetrahedral elements were used in 3D meshes. For all fluid flow simulations $P_2 + P_1$ element discretization was used and the solutions were obtained with the direct solver MUMPS.

Table 3.3: Mesh sizes of the applied CFD models

Cartridge	2D model applied mesh elements	2D model refined mesh elements	Relative error for 2D models %	3D model applied mesh elements	3D model refined mesh elements	Relative error for 3D models %
A	150.000	250.000	−0.01	4.700.000	6.000.000	0.01
B	160.000	250.000	−0.10	–	–	–
C	1.700.000	3.000.000	−0.25	5.000.000	5.000.000	0.03
D	1.700.000	3.000.000	−0.25	5.000.000	5.000.000	0.03
E	1.700.000	3.000.000	−0.25	5.000.000	5.000.000	0.03
F	1.500.000	3.000.000	+0.02	4.500.000	5.500.000	0.02
G	1.600.000	3.000.000	−0.05	–	–	–

3.6.2 Consistency check for double membrane layer modeling

In section 3.3 we introduced an approach for treating double membrane layers as a single membrane layer with average material properties. Here comparative 2D simulations of a homogeneous membrane layer Fig. 3.8a and heterogeneous double layers Fig. 3.8b were carried out. The specifications of cartridge A were used in the regular generic method for the geometry reconstruction. Results are shown in Fig. 3.8 and with a naked eye no visible differences between the two models can be observed. The water flow rate of the entire cartridge is calculated from simulation results. From the latter, the velocity magnitude in m/s is multiplied by the area of the filter cartridge in m^2 which is calculated by $area = 2\,\pi\,r\,h$ where r is the radius of the filter cartridge in m and h the height in m. The water flow rate in m^3/s is compared to the experimental values. When the simulation results are calculated for the entire cartridge the two models yield at a difference of 2.5%. However, Sartorius Stedim Biotech assumes an average measurement error for all cartridges about 2%. Hence the deviation between the two models can be considered insignificant. For this study, the following simulations were performed with a homogeneous membrane layer.

3.6.3 Differences between geometry reconstruction methods

2D models of the standard cartridge A were built based on the four pleat reconstruction methods. Flow profile results were computed for pressure drops of 0.1 *bar*, 0.5 *bar* and 1 *bar*. Fig. 3.9 shows the flow magnitude results at a pressure drop of 0.5 *bar* and the rest are shown in the Appendix (Fig. 6.1 at a pressure drop of 0.1 *bar* and Fig. 6.2 a pressure drop of 1.0 *bar*). All exhibit higher velocities at the spaces between the pleats and homogeneous flow within the membrane domain where the average velocity is the same. The typical flow path is along the pleats and the fluid will cross the membrane shortly due to the high pressure drop. Jets are observed at the downstream part of the filter cartridge and are caused by the pleat structure. Fig. 3.9a shows the reconstruction of the geometry based on the image analysis method. This manual approach requires high effort and yields at a high degree of accuracy since the center line of each pleat is followed during the geometry reconstruction. Fig. 3.9b shows the results based on

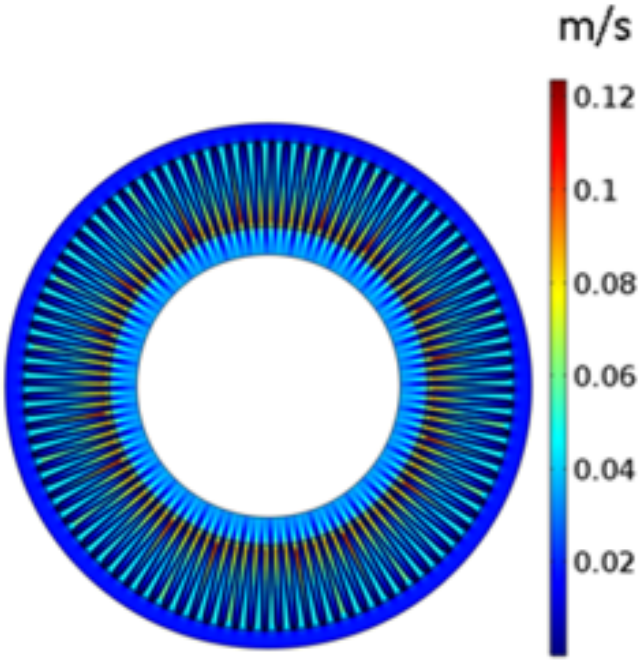

(a) Homogeneous membrane layer

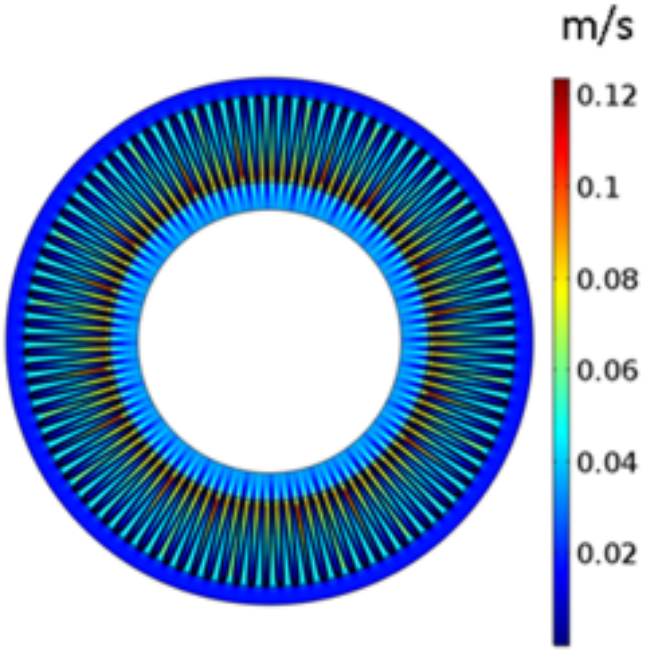

(b) Double membrane layer

Figure 3.8: Simulated velocity magnitude profiles for cartridge A with homogeneous and double membrane layer

the regular generic design method. It is simpler and quicker to obtain this geometry but it is less detailed because all pleats are regular and the distance between them is

equal. The results from the deterministic irregular design are shown in Fig. 3.9c. In comparison to the image analysis method it is easier to set up the geometry using the deterministic irregular method. Even though the width of each pleat matches the width of the microscopic image some differences can still be observed such as the jets patterns. Finally, Fig. 3.9d shows the results from the randomized irregular pleat reconstruction approach with one set of random numbers. For this specific set of random numbers Fig. 3.9d is similar to Fig. 3.9b and no clear flow patterns can be observed.

Experimental data that give insights into the flow patterns of the cartridge during the operation are extremely challenging and difficult to obtain. In contrast, measurements of the flow rate as a function of the pressure drop are possible and were performed at Sartorius Stedim Biotech. From the simulation results the water flow rate of the whole cartridge was calculated and compared to the experimental data as shown in Tab. 3.4. The discrepancy between the simulation results and the measurements was smallest at 0.5 *bar* and largest at 0.1 *bar*. The linearity of water flow rate to pressure drop from 0.1 *bar* to 1.0 *bar* is observed for the simulations but not for the experimental data. The variation of the experimental data is about 2%.

With only one exception the image analysis method is always the most accurate followed by the deterministic irregular approach whereas the other two methods have comparably much larger prediction errors. Since the deterministic irregular design is less laborious as the image analysis method it could be chosen as an alternative option for the pleat reconstruction. However, both methods have the disadvantage that they can reproduce only a sector of the cartridge. From Tab. 3.4 it is concluded that the regular generic design results in the highest discrepancies between the simulation results and the measurements for the analyzed cartridge. Further analysis with different sets of random numbers has been performed in the case of the randomized irregular design and the discrepancy between these different models is 0.5 percentage points.

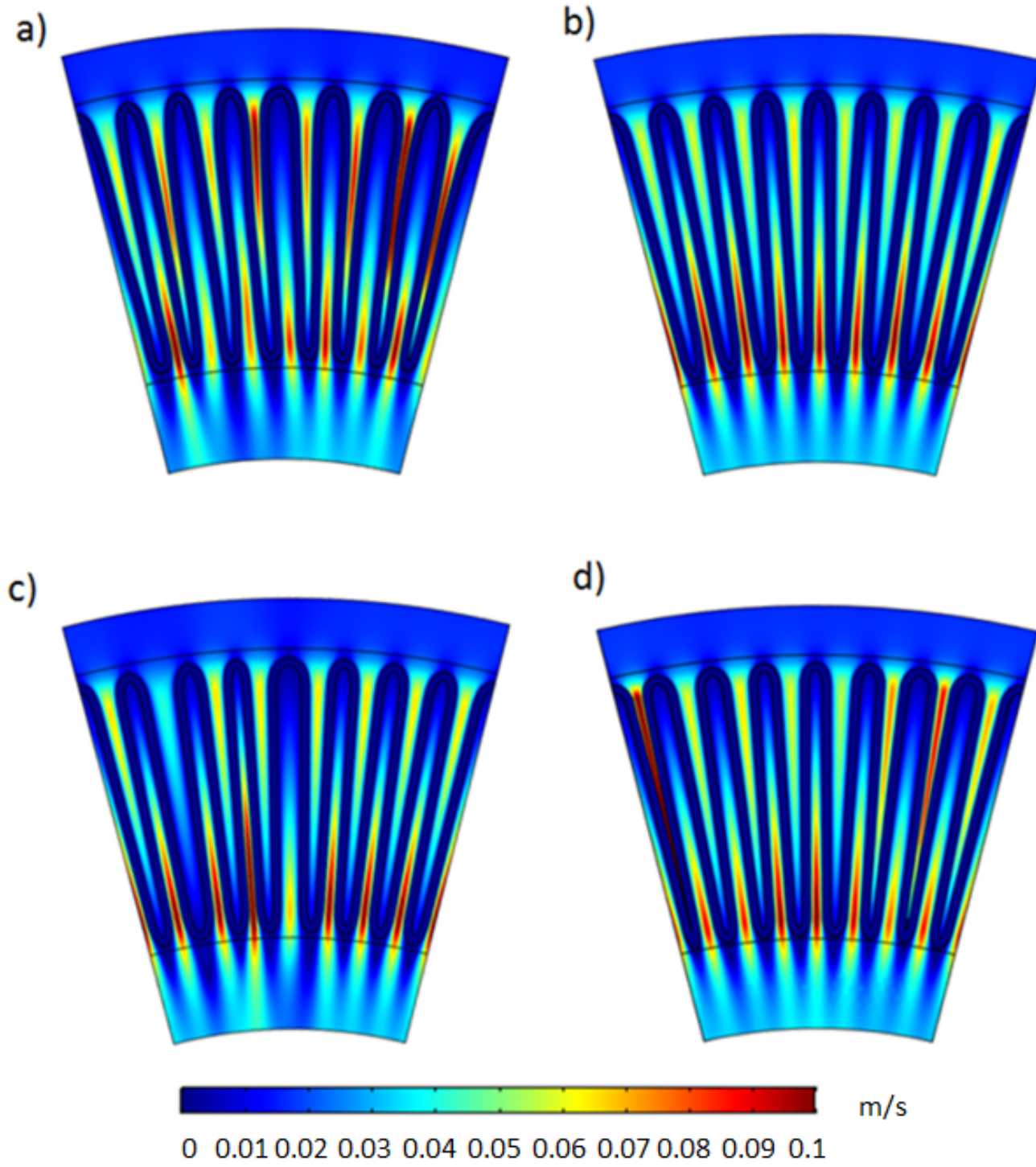

Figure 3.9: Simulated velocity magnitude profiles for cartridge A in a 2D cross section for a pressure drop of 0.5 *bar. Pleat geometry reconstructed by a) image analysis, b) regular generic, c) deterministic irregular generic, and d) randomized irregular design*

Table 3.4: Water flow rates of cartridge A as measured and simulated in 2D and 3D. Difference between measured and simulated values is shown in parentheses

Design	Pressure drop	Experimental	Simulated (2D)	Simulated (3D) without frame	Simulated (3D) with frame
Units	*bar*	$\frac{L}{min}$	$\frac{L}{min}$	$\frac{L}{min}$	$\frac{L}{min}$
Image analysis	0.1	8.1	9.7 (+20.0 %)	–	–
Regular generic	0.1	8.1	10.3 (+27.2 %)	10.4 (28.4 %)	10.3 (+27.2 %)
Irregular generic	0.1	8.1	9.8 (+21.3 %)	–	–
Randomized generic	0.1	8.1	10.3 (+27.2 %)	–	–
Image analysis	0.5	44.3	48.6 (+9.6 %)	–	–
Regular generic	0.5	44.3	51.5 (+16.3 %)	51.8 (+16.9 %)	51.0 (+15.1 %)
Irregular gereric	0.5	44.3	49.1 (+10.9 %)	–	–
Randomized generic	0.5	44.3	51.5 (+16.2 %)	–	–
Image analysis	1.0	83.1	97.1 (+20.0 %)	–	–
Regular generic	1.0	83.1	103.8 (+24.0 %)	103.5 (+24.5 %)	101.5 (+22.1 %)
Irregular generic	1.0	83.1	98.2 (+18.2 %)	–	–
Randomized generic	1.0	83.1	102.8 (+23.7 %)	–	–

3.6.4 Impact of the plastic cage

For cartridge A it is observed that all 2D studies systematically overpredict the flow rates in comparison to the measurements. However, the impact of the plastic cage on the flow rate hasn't been included yet. In general, it is expected that the consideration of the plastic cage will add flow resistance in the filter cartridge resulting in lower flow rates. Further CFD studies were performed in order to quantify the impact of the plastic cage on the water flow rate. Due to change in symmetry 3D simulations were carried out. In contrast to 2D simulations 3D studies require more memory and processors and cost a higher computational time. The membrane geometry was reproduced based on the regular generic design method because high quality microscopic images of the pleats weren't available for cartridge A. Fig. 3.10 shows the simulated flow profile at a pressure drop of 0.5 *bar* and the simulation results at a pressure drop of 0.1 *bar* and at 1.0 *bar* are shown in the Appendix (Fig. 6.3 and Fig. 6.4).

Tab. 3.4 shows the simulation results for different pressure drops. The numerical accuracy of 3D calculations is tested by making the plastic cage permeable and the obtained results are compared with the 2D simulations (Fig. 3.10). The difference between the 2D results and the 3D simulation where the plastic cage has infinite perme-

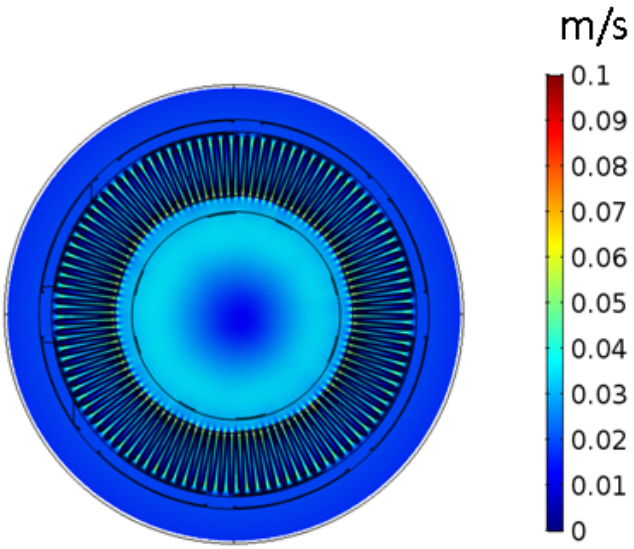

(a) Permeable

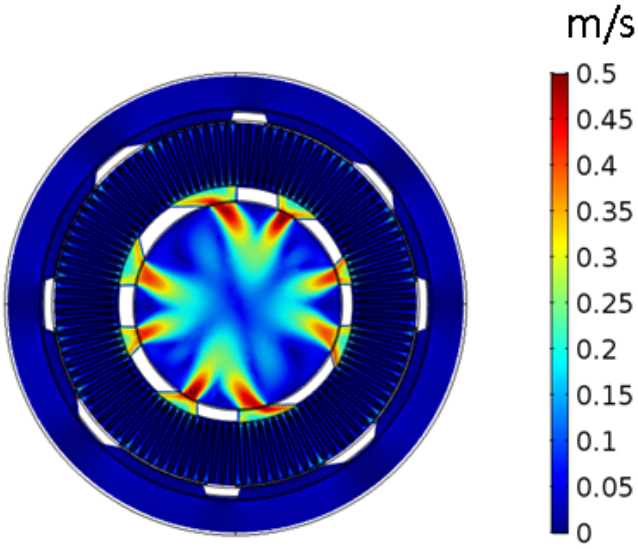

(b) Impermeable

Figure 3.10: Simulated velocity magnitude profiles for cartridge A in a 3D cylinder for a pressure drop of 0.5 *bar. Pleat geometry reconstructed by regular generic design. Both figures show a cross-section though the simulated cylinder*

ability is below 1.2 percentage points. The discrepancy between the studies where the plastic cage was taken into account (impermeable) with those where it was neglected (permeable) is below 2.4 percentage points. However, the difference between the image analysis and the regular generic method is much higher. Furthermore, simulations with impermeable plastic cage result in differences which are in the same range of the experimental error so the plastic cage can be neglected. Hence, we hypothesize that

the remaining difference between the simulations and the experiments is caused by the fleece layer which is not considered so far.

3.6.5 Impact of the pleat number

Before studying the fleece layer the impact of the pleat number on the water flow rate is discussed. Cartridge B has the same pleat height as cartridge A and consists of two membrane layers. However, the prefilter membrane of cartridge B is thinner and has a higher permeability than that of cartridge A. In addition, cartridge B contains 138 pleats whereas cartridge A contains 104 pleats (Tab. 3.1). The reconstruction of the pleat geometry was based on the image analysis method and on the regular generic design approach. Cartridge B was simulated at the same pressure drops as cartridge A, i.e. 0.1 *bar*, 0.5 *bar* and 1 *bar*. The flow profile results at a pressure drop of 0.5 *bar* are shown in Fig. 3.11 and the simulation results at a pressure drop of 0.1 *bar* and at 1.0 *bar* are shown in the Appendix (Fig. 6.5 and Fig. 6.6).

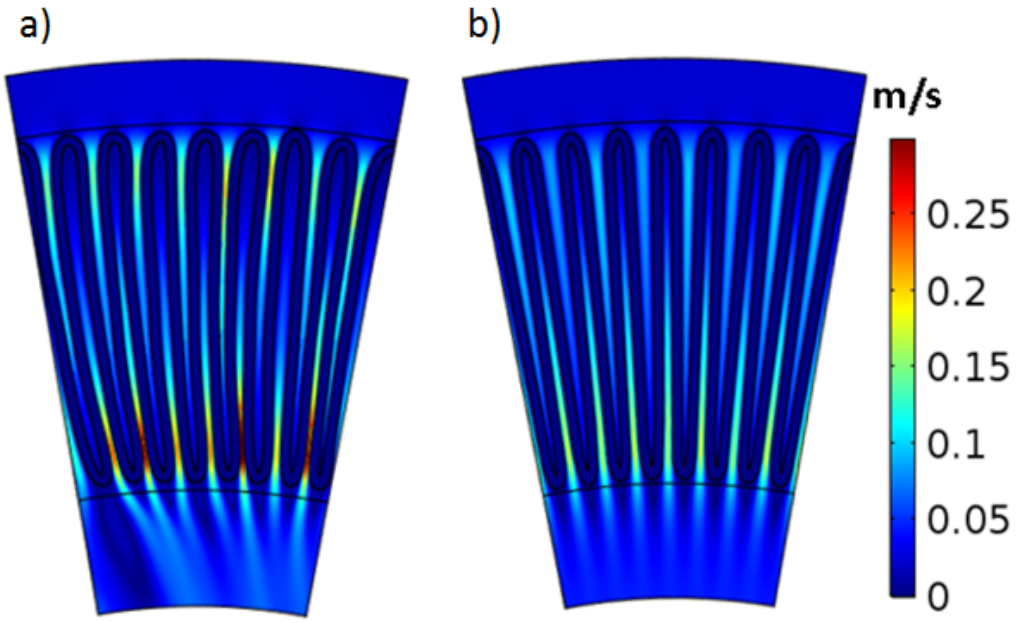

Figure 3.11: Simulated velocity magnitude profiles for cartridge B in a 2D cross section for a pressure drop of 0.5 *bar. Pleat geometry reconstructed by a) Image analysis design b) Regular generic design*

From the latter it is observed that the pleats which were reconstructed based on the image analysis method are tilted in contrast to the pleat geometry based on the regular

generic method. Moreover, the pleats are more densely packed in contrast to cartridge A. Tab. 3.5 shows the comparison between simulations and experimental data. It is observed that with increasing pressure drop the discrepancy between the simulations and the measurements increases. In addition, due to the higher pleat packing density the difference between the image analysis and the regular generic method is below 2.8 percentage points. As a result, for cartridge B the regular generic design can be used for the reconstruction of the pleats. Analysis of cartridge A revealed that the plastic cage can be neglected. Based on the previous hypothesis, the impact of the fleece layer on the water flow rate will be analyzed.

Table 3.5: Water flow rates of cartridge B as measured and simulated in 2D and 3D. Difference between measured and simulated values is shown in parentheses

Design	Pressure drop	Experimental	Simulated (2D)
Units	*bar*	$\frac{L}{min}$	$\frac{L}{min}$
Image analysis	0.1	14.0	15.2 (+8.5 %)
Regular generic	0.1	14.0	14.9 (+6.3 %)
Image analysis	0.5	56.6	75.9 (+34.2 %)
Regular generic	0.5	56.6	74.4 (+31.4 %)
Image analysis	1.0	99.5	149.7 (+50.5 %)
Regular generic	1.0	99.5	148.3 (+49.1 %)

3.6.6 Impact of the fleece layer

Catridges C, D and E are used in order to analyze the impact of the fleece layer on the water flow rate. These cartridges are exclusively built and measured by Sartorius Stedim Biotech for this project. In contrast to cartridges A and B, cartridges C, D and E are identical except for the number of pleats. Generally, the material properties of those three prototypes are similar to these of cartridge A. Cartridge D has 102 pleats whereas cartridge A contains 104 pleats. Cartridge C has 95 pleats and cartridge E has 110 pleats (Tab. 3.1).

Analysis of these cartridges has been performed in a similar way to A. However, high quality microscopic images of the full cross section were provided by Sartorius Stedim Biotech. A typical microscopic image of cartridge C is shown in Fig. 3.12, and

in total 8 microscopic images where combined in order to depict a full cross-section of cartridge C. In particular, adjustment of the membrane position at the side boundaries of the geometry is not demanded. The exact position of the pleated membrane and fleece layers is accurately shown in the microscopic images. Hence the image analysis method is used for reconstructing the geometries and the geometry of cartridge C is shown in Fig. 3.13. The irregular shape that is observed for the pleats at the left side of Fig. 3.13 is created when the first and last pleat are glued together. Similar procedure was followed for creating the geometries for cartridges D and E.

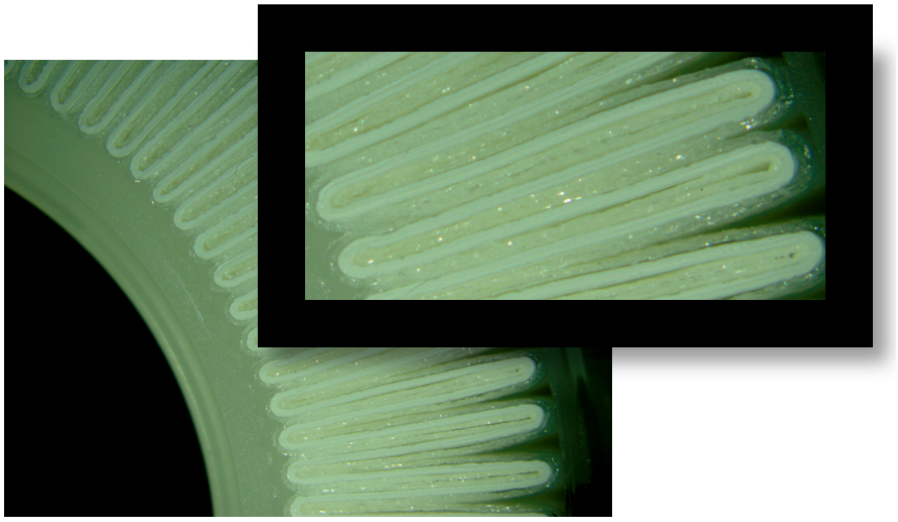

Figure 3.12: Microscopic image of pleated membrane and fleece layers for cartridge C (courtesy of Sartorius Stedim Biotech)

The intrinsic permeability of the membrane layers has been converted from water flow density measurements independent from the arrangement of the cartridge (Tab. 3.2). However, it is difficult to measure directly the permeability of the fleece layer. Moreover, the fleece permeability can vary significantly in axial and lateral flow directions and experimental data were not available. In simulations for cartridges A and B the fleece layer hasn't been considered which is the same as assuming infinite fleece permeability. For comparison, simulations of cartridges C, D and E were performed where the fleece layer was considered infinitely permeable. At a pressure drop of 2.0 *bar* the simulation results overpredict the water flow density up to 33% for cartridges C and D and up to 44% for cartridge E as shown in Tab. 3.6 - 3.8. The fleece permeability is

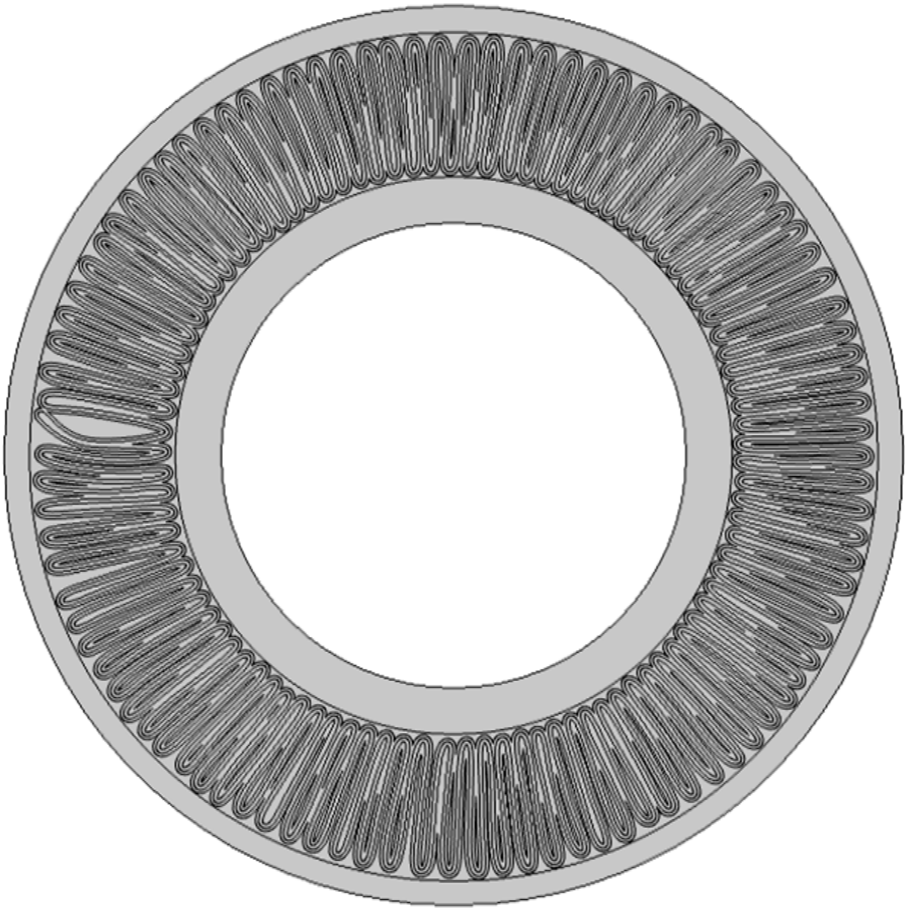

Figure 3.13: Computational geometry for cartridge C where membrane and fleece layers are recreated using the image analysis method

estimated for cartridges C, D and E at different water flow rates so that the simulations match the measurements and the values are tabulated in Tab. 3.6 - 3.8. These values show that the fleece is more permeable than the membrane by almost four orders of magnitude. From Fig. 3.14a it is shown that the estimated fleece permeabilities depend on the pressure drop even though the permeability strictly is a material property. However, some simplifications are made. First, the direction of the fleece permeability is considered isotropic. In addition, the fleece permeability values don't take into account the compression of the fleece towards the center of the filter which will lead to a decreased pleat width. Hence, the estimated fleece permeability values will not match the true material property. As it is shown in Tab. 3.6 - 3.8 the fleece permeability values are found to be dependent on the water flow rate. This dependency can be potentially explained by the fact that the fleece is more compressed due to pleat movement at higher

pressure drops. Consequently, the estimated fleece permeability values can be only used as apparent values that depend on specific cartridge and pressure drop. However, they can be interpolated between pressure drops, and transferred between different cartridges with specific limits as shown in the following.

Fig. 3.14b shows the relationship of the estimated fleece permeability and its reciprocal value, which is resistance, over pressure drop. For each of the cartridges the estimated resistance increases with pressure drop except for very low flow rates which are not relevant for practical operations. It is a non trivial finding due to the complex, non-linear nature of pressure dependence of partial fleece compression on the membrane structure. However, this observed linear relationship can be used for interpolating between pressure drops.

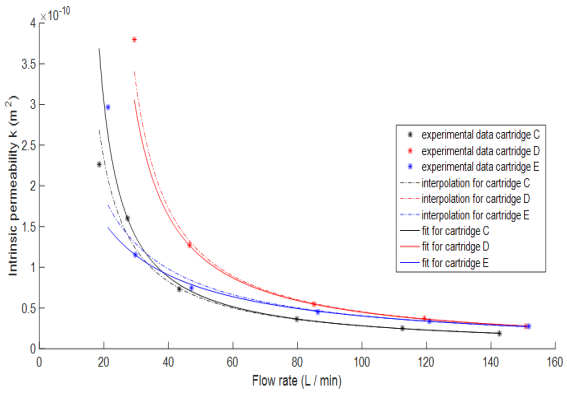

(a)

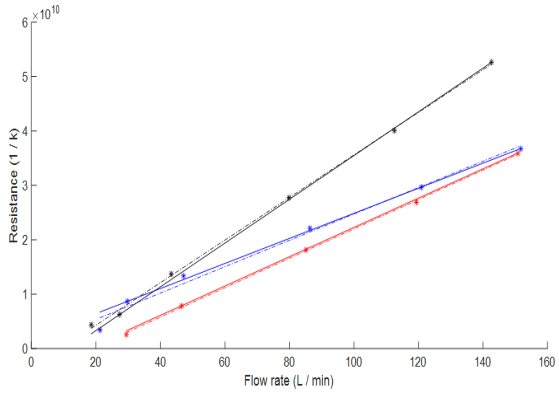

(b)

Figure 3.14: Flow rate over pressure drop and resistance (1/k) over pressure drop for cartridges C, D and E

Table 3.6: Water flow rates of cartridge C as measured and simulated in 2D with fleece layer. Difference between measured and simulated values is shown in parentheses

Pressure drop *bar*	Experimental flow rate $\frac{L}{min}$	Simulated (2D) without fleece layer $\frac{L}{min}$	Fleece k m^2
0.1	10.1	9.5 (-5.9 %)	–
0.2	18.5	19.1 (+3.2 %)	$2.26\ 10^{-10}$
0.3	27.3	28.6 (+4.8 %)	$1.60\ 10^{-10}$
0.5	43.3	47.6 (+9.9 %)	$0.73\ 10^{-10}$
1.0	79.8	95.1 (+19.2 %)	$0.36\ 10^{-10}$
1.5	112.5	142.7 (+26.8 %)	$0.25\ 10^{-10}$
2.0	142.7	190.0 (+33.1 %)	$0.19\ 10^{-10}$

Table 3.7: Water flow rates of cartridge D as measured and simulated in 2D with fleece layer. Difference between measured and simulated values is shown in parentheses

Pressure drop *bar*	Experimental $\frac{L}{min}$	Simulated (2D) without fleece layer $\frac{L}{min}$	Fleece k m^2
0.1	11.2	10.1 (-9.8 %)	–
0.2	20.7	20.2 (-2.4 %)	–
0.3	29.4	30.3 (+3.1 %)	$3.80\ 10^{-10}$
0.5	46.5	50.4 (+8.4 %)	$1.27\ 10^{-10}$
1.0	85.1	100.6 (+18.2 %)	$0.55\ 10^{-10}$
1.5	119.3	150.6 (+26.2 %)	$0.37\ 10^{-10}$
2.0	150.9	201.6 (+33.6 %)	$0.28\ 10^{-10}$

Table 3.8: Water flow rates of cartridge E as measured and simulated in 2D with fleece layer. Difference between measured and simulated values is shown in parentheses

Pressure drop *bar*	Experimental $\frac{L}{min}$	Simulated (2D) without fleece layer $\frac{L}{min}$	Fleece k m^2
0.1	11.4	11.1 (-2.6 %)	–
0.2	21.2	22.2 (+4.7 %)	$2.97\ 10^{-10}$
0.3	29.8	33.3 (+11.7 %)	$1.15\ 10^{-10}$
0.5	47.1	55.3 (+17.4 %)	$0.75\ 10^{-10}$
1.0	86.3	110.1 (+27.6 %)	$0.45\ 10^{-10}$
1.5	120.9	164.6 (+36.1 %)	$0.34\ 10^{-10}$
2.0	151.7	218.8 (+44.2 %)	$0.27\ 10^{-10}$

3.6.7 Interpolation of fleece permeability

For each cartridge the fleece permeabilities were interpolated by taking the estimated values at the highest and second lowest pressure drop. For the cases were the simulations with infinite fleece permeability result in lower water flow rates than the experimental data, the apparent fleece permeability values couldn't be estimated. The lowest pressure drop for which a positive permeability was estimated was excluded due to the observed deviation from the linear model. The taken points are used to interpolate the fleece permeability at the other pressure drops where experimental data are available. The results are shown in Tab. 3.9 - Tab. 3.11 and in Fig. 3.15. The difference between the simulations and the experiments is below 2%. Only for cartridge E at the lowest pressure drop of 0.2 *bar* the extrapolated fleece permeability results in 5% difference from the experiments. However, these results are significantly improved in comparison to the cases where the permeability of the fleece layer was considered infinite permeable (difference up to 44%). It is now possible to predict the performance of the cartridges with an error of up to 2%. This error is in the same range of the experimental errors. As a result, experimental costs can be minimized.

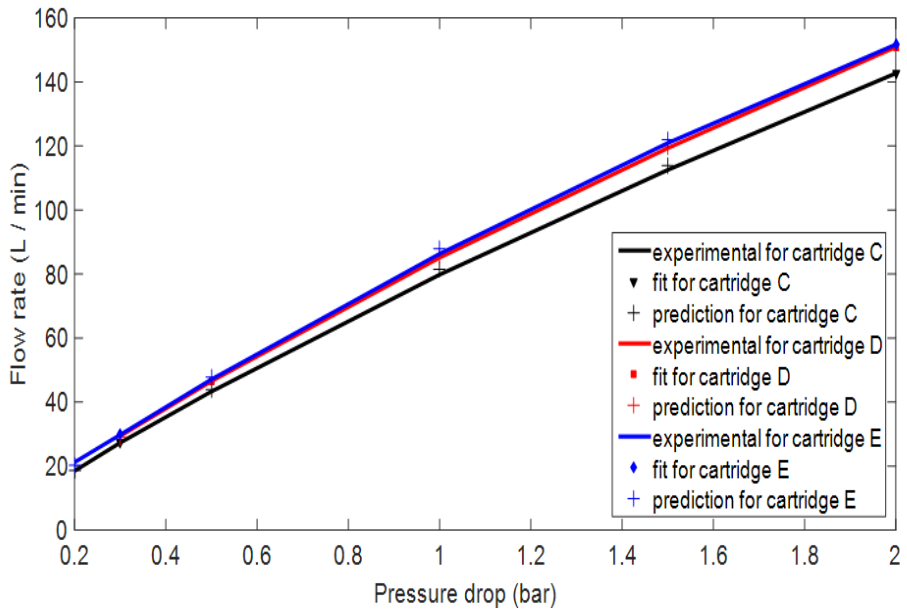

Figure 3.15: Interpolation of fleece permeability values for cartridges C, D and E

Table 3.9: Water flow rates of cartridge C as measured and simulated in 2D with interpolated fleece permeability values. Difference between measured and simulated values is shown in parentheses

Pressure drop *bar*	Experimental flow rate $\frac{L}{min}$	Simulated (2D) $\frac{L}{min}$	Fleece k m^2
0.2	18.5	18.5 (0.0 %)	$2.74\ 10^{-10}$
0.5	43.3	43.9 (+1.4 %)	$0.87\ 10^{-10}$
1.0	79.8	81.3 (+1.9 %)	$0.41\ 10^{-10}$
1.5	112.5	113.9 (+1.2 %)	$0.27\ 10^{-10}$

Table 3.10: Water flow rates of cartridge D as measured and simulated in 2D with interpolated fleece permeability values. Difference between measured and simulated values is shown in parentheses

Pressure drop *bar*	Experimental flow rate $\frac{L}{min}$	Simulated (2D) $\frac{L}{min}$	Fleece k m^2
0.3	29.4	28.9 (-1.7 %)	$2.41\ 10^{-10}$
1.0	85.1	85.7 (+0.7 %)	$0.58\ 10^{-10}$
1.5	119.3	119.6 (+0.3 %)	$0.38\ 10^{-10}$

Table 3.11: Water flow rates of cartridge E as measured and simulated in 2D with interpolated fleece permeability values. Difference between measured and simulated values is shown in parentheses

Pressure drop *bar*	Experimental flow rate $\frac{L}{min}$	Simulated (2D) $\frac{L}{min}$	Fleece k m^2
0.2	21.2	20.2 (-4.7 %)	$1.42\ 10^{-10}$
0.5	47.1	47.8 (+1.5 %)	$0.83\ 10^{-10}$
1.0	86.3	87.8 (+1.7 %)	$0.49\ 10^{-10}$
1.5	120.9	122.0 (+0.9 %)	$0.35\ 10^{-10}$

3.6.8 Transfer of fleece permeability

After successfully interpolating the estimated permeabilities for different pressure drops for the same cartridge it is now attempted to transfer the fleece permeability values between different cartridges at the same pressure drop. The fleece permeability values that are estimated from one cartridge are used for predicting the performance of the other two and the results are shown in Fig. 3.16. The simulated water flow rates for cartridge C coincide with the experimental data with a deviation of 2% which increases

up to 7% for the highest pressure drop of 2.0 *bar*. The difference between simulations and experiments for cartridge C in the case where the fleece was infinitely permeable was up to 33% for the pressure drop of 2.0 *bar*. Similar observations are made for cartridges D and E when the fleece permeability values of the respective other cartridges are used. The apparent permeability values are useful when they are transferred across cartridges with identical membrane properties since the prediction of their performance with respect to the water flow rate has deviations that are generally in the range of the experimental error. Taking into consideration the complicated nature of the experiments that determine the fleece permeability and the costs of prototypes this method can be used for predicting the performance of such cartridges. In addition, this approach can be very useful for industrial process development since it could be also used for membranes.

3.6.9 Flow and pressure profiles

CFD results for cartridges C, D and E contain much more information than just water flow rate. Further analysis of cartridges C, D and E has been performed. The hydrodynamics analysis of all three cartridges revealed uniform flow in the porous region. At the downstream part the high degree of fleece compression is visible, especially at the inner part of the pleats. As a result the permeability of the fleece layer at these regions is decreased. Fig. 3.17a shows the flow velocity profile for cartridge C at a pressure drop of 0.2 *bar*. In addition, we can observe that the direction of the flow indicates that the lateral permeability values especially at the compressed regions change under pressure for cartridge C but cartridges D and E show similar behaviour. Although the permeability of the fleece layer is much larger than that of the membrane it is found to have a big impact.

In addition, an increased pressure drop will cause movement of the pleats and change in the fleece permeability which is not considered in the modeled geometry (Fig. 3.17b). Hence, it impacts on the estimated fleece permeability. As a consequence, the water flow rate isn't a linear function of the pressure drop as it would be predicted by Darcy's law for an incompressible medium. Previously it was found that the impact

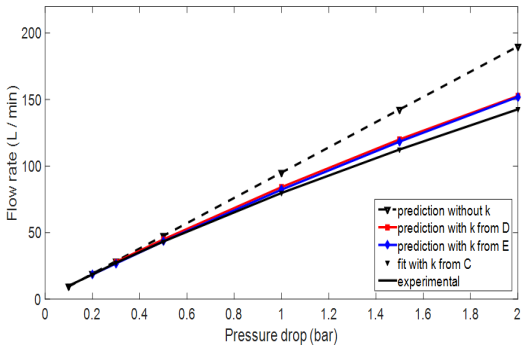

(a) Cartridge C

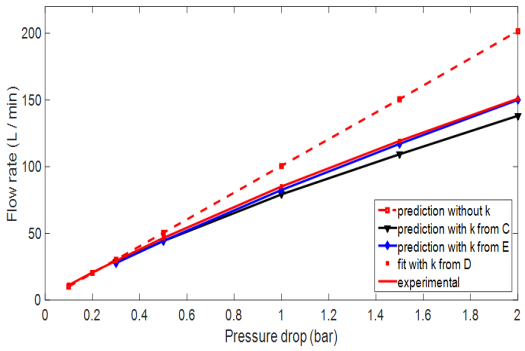

(b) Cartridge D

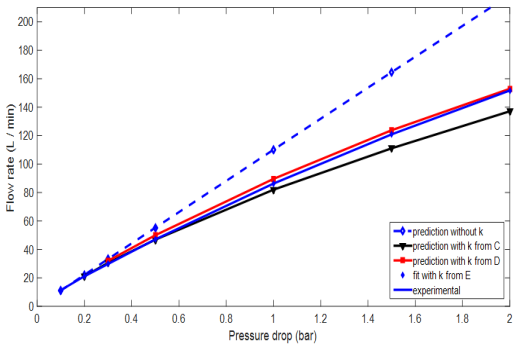

(c) Cartridge E

Figure 3.16: Transfer of fleece permeability values for cartridges C, D and E at respective pressure drops

of the plastic cage on the water flow rate is insignificant. 3D simulations with the plastic cage and the fleece layer have been performed. The numerical accuracy has been tested as has been explained before. Fig. 3.18 shows the simulation results for cartridge C. The 3D results show that the resistance of the plastic cage is also not important here and it can be neglected reducing the computational geometry in two dimensions. The results are similar for cartridges D and E.

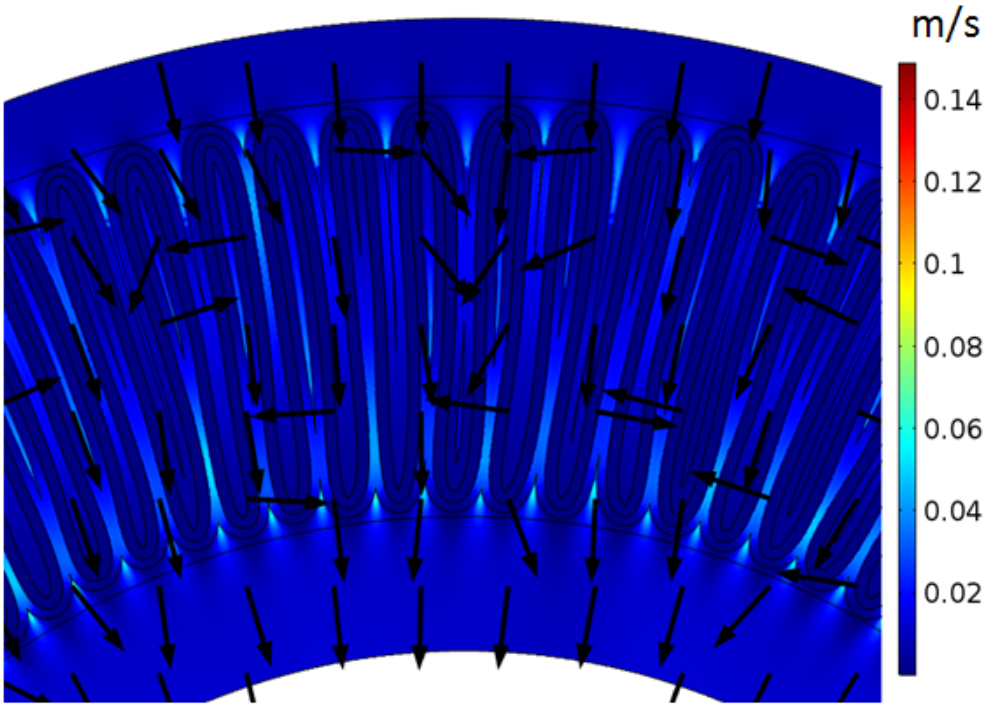

(a) Direction of the fluid flow

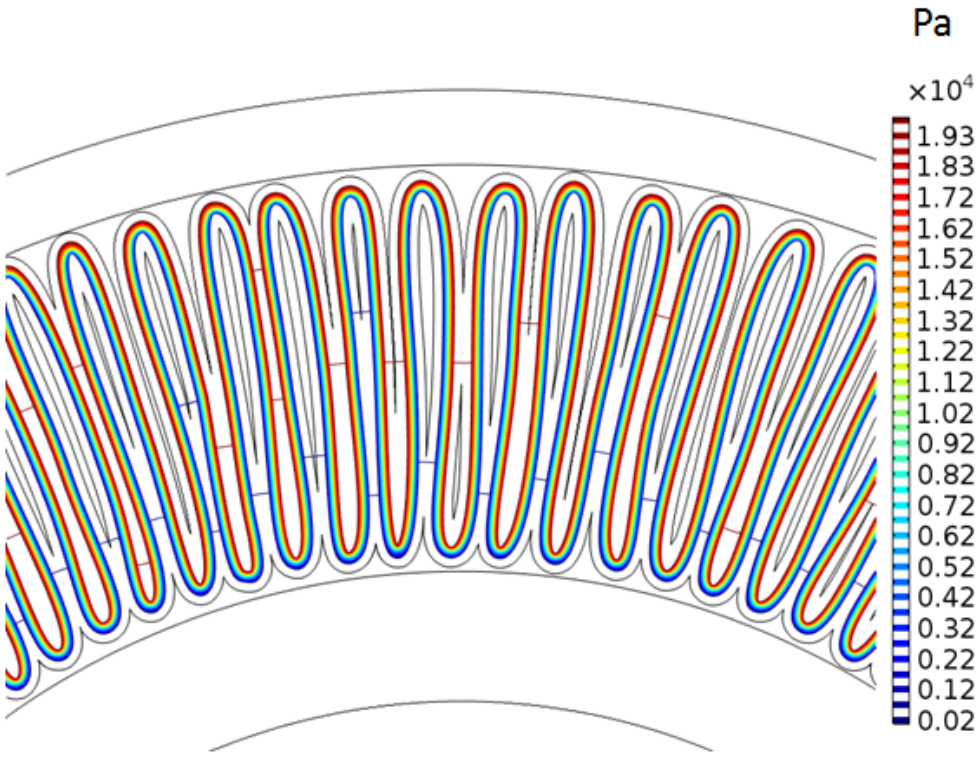

(b) Contour plot of pressure drop

Figure 3.17: Cartridge C in a 2D cross section for a pressure drop of 0.2 *bar*

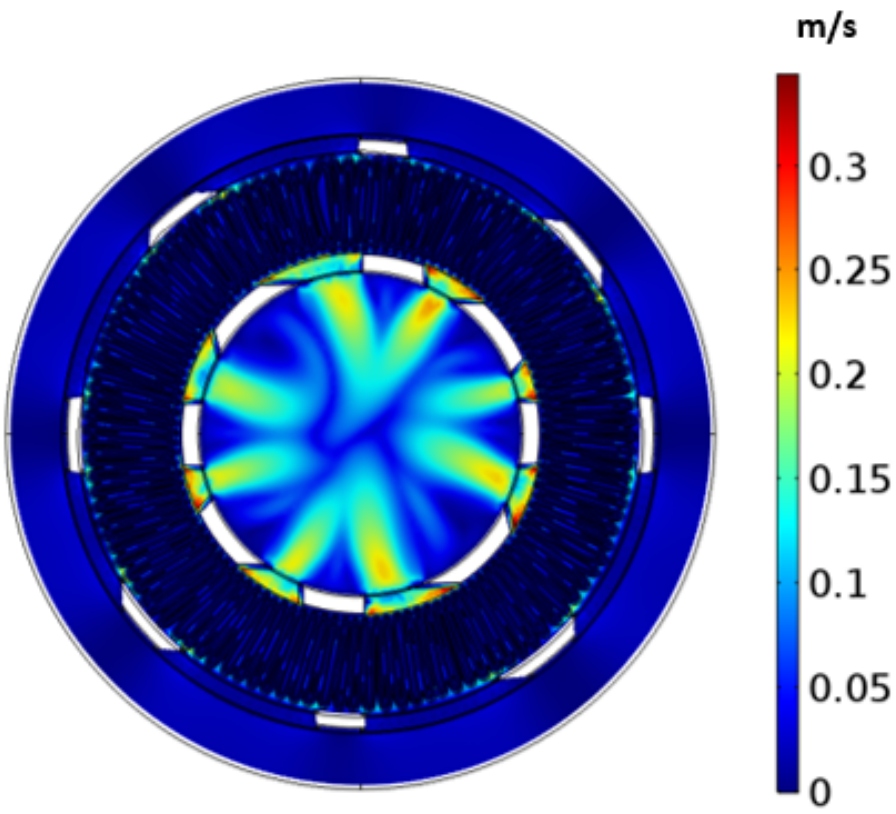

Figure 3.18: Simulated velocity magnitude profiles for cartridge C in a 3D cylinder for a pressure drop of 0.5 *bar and the pleat geometry was reconstructed by the image analysis design. Both figures show a cross-section though the simulated cylinder*

3.6.10 Impact of pleat height

Cartridges A to E have the same pleat height and consist of two membrane layers. Now, two cartridges F and G, with different core diameter are studied. Cartridge G has a smaller core diameter and consequently less pleats can be arranged in the cartridge. Cartridges F and G contain only one membrane layer and have considerably less pleats than cartridges A-E.

The regular generic design method was used for reconstructing the computational geometries because high quality microscopic images weren't available. For both cartridges a constant fleece thickness was assumed (Fig. 3.19, 3.20). Initially the impact of the fleece layer was neglected by considering infinite permeability. The quantitave results and the validation of the 2D simulations against experimental data for each cartridge is shown in Tab. 3.12 and Tab. 3.13. The difference between the simulations and

the experiments is significantly bigger in comparison to cartridges C, D and E and it differs up to two orders of magnitude. This is caused by the fact that the filter cartridges contain only one membrane layer with increased permeability. For cartridge F when the fleece layer is neglected, the water flow rate is 73.5 % higher than the experimental value at 0.5 *bar* and 258.5% higher at 1.0 *bar*. For cartridge G and for infinitely permeable fleece the water flow rate is 176.3 % higher than the measurements at 0.1 *bar*, 466.7 % higher than the experimental value at 0.5 *bar* and 258.5% higher at 1.0 *bar*. Transfer of the fleece permeabilities between cartridges F and G at the same pressure drops showed a difference between the experiments and the simulations of 2% at a pressure drop of 0.1 *bar* and 8% at a pressure drop of 0.5 *bar* (Fig. 3.21).

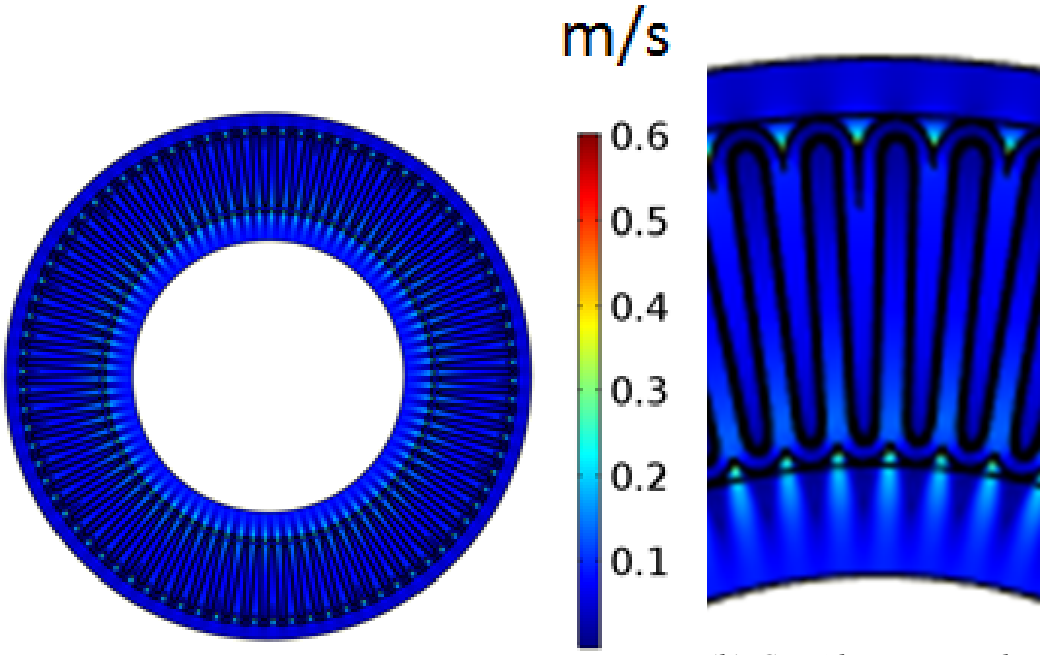

(a) Cartridge F

(b) Cartridge F zoomed-in section

Figure 3.19: Simulated velocity profiles for cartridges F and G in a 2D cross section for a pressure drop of 0.5 *bar. Pleat geometry reconstructed by regular generic design*

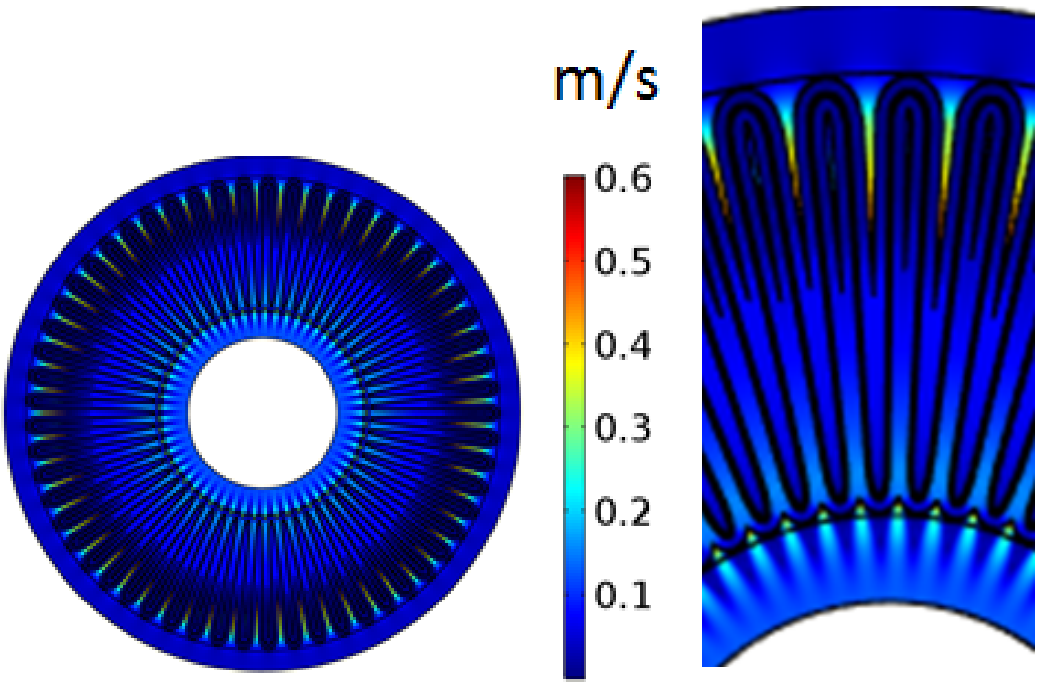

(a) Cartridge G

(b) Cartridge G zoomed-in section

Figure 3.20: Simulated velocity profiles for cartridges F and G in a 2D cross section for a pressure drop of 0.5 *bar. The pleat geometry was reconstructed by the regular generic design*

Table 3.12: Water flow rates of cartridge F as measured and simulated in 2D with interpolated fleece permeability values. Difference between measured and simulated values is shown in parentheses

Pressure drop *bar*	Experimental $\frac{L}{min}$	Simulated (2D) without fleece layer $\frac{L}{min}$	Fleece k m^2
0.1	59.3	102.9 (+73.5 %)	$0.80\ 10^{-10}$
0.5	143	512.7 (+258.5 %)	$0.22\ 10^{-10}$

In all cartridges A to E the flow resistance caused by the plastic cage is negligible in comparison to that caused by the fleece layer. However, the flow resistance is much lower in cartridges F and G due to the high permeability of the porous media. Therefore the impact of the plastic cage on the water flow rate has to be reanalyzed. First, the impact of the plastic cage is studied independently from the fleece layer by assuming infinite permeability for comparison with the other cartridges (Fig. 3.22). For a pressure drop of 0.5 *bar* the three dimensional studies without the fleece layer show 150% higher

Table 3.13: Water flow rates of cartridge G as measured and simulated in 2D with interpolated fleece permeability values. Difference between measured and simulated values is shown in parentheses

Pressure drop *bar*	Experimental $\frac{L}{min}$	Simulated (2D) without fleece layer $\frac{L}{min}$	Fleece k m^2
0.1	48.2	133.2 (+176.3 %)	$0.71\ 10^{-10}$
0.5	116.3	659.1 (+466.7 %)	$0.25\ 10^{-10}$
1.0	167.6	1297.1 (+673.9 %)	$0.16\ 10^{-10}$

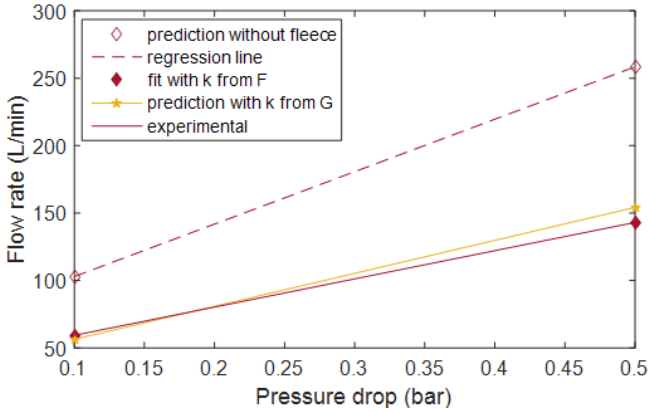

(a) Cartridge F

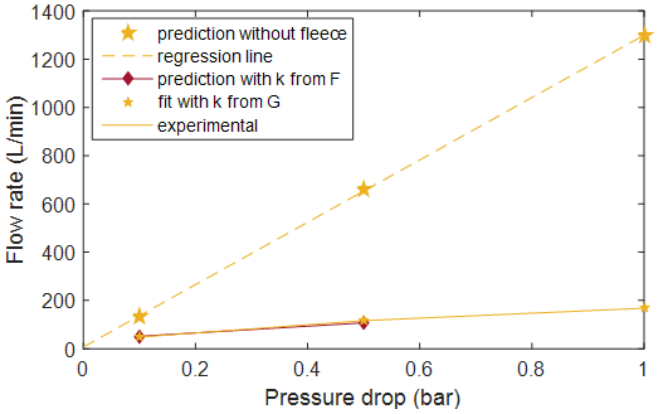

(b) Cartridge G

Figure 3.21: Fleece permeability transfer between cartridges F and G at respective pressure drops

flow rate in contrast to 250% of the 2D study. Then, a 3D study where the fleece layer is considered in combination with the plastic cage is performed at the pressure drop of 0.5 *bar*. For the fleece layer the permeability that has been estimated from the 2D studies is used. When the fleece layer is considered in the 3D studies the simulated

water flow rate is 15 % lower than the experimental value at 0.5 *bar*. Therefore the permeability of the fleece is estimated from the 3D studies. Consequently, the influence of the plastic cage on the water flow rate is important and the fleece permeability values are estimated based on 3D studies.

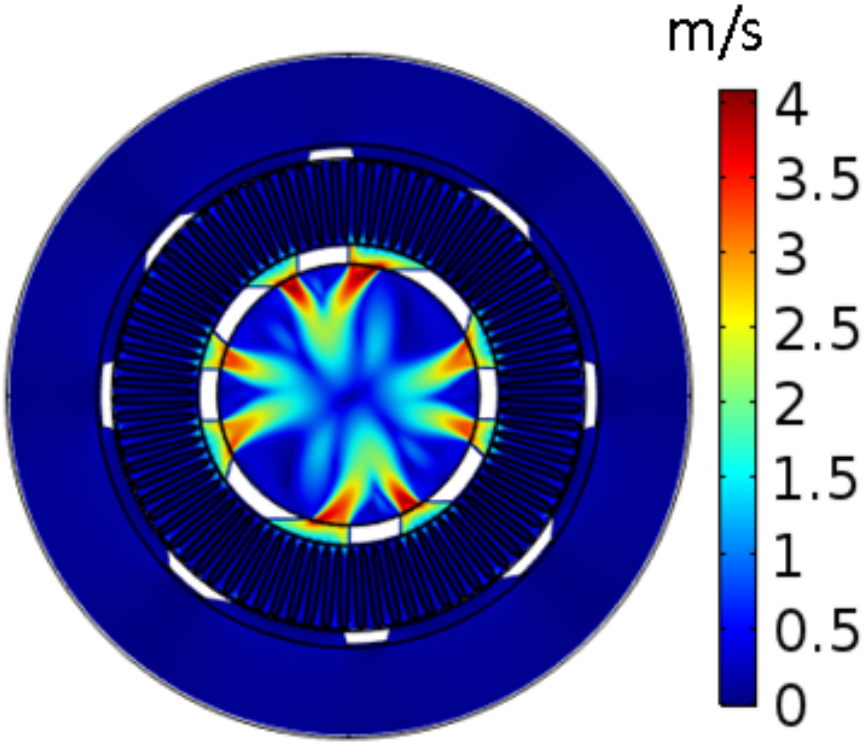

Figure 3.22: Simulated velocity magnitude profiles for cartridge F in a 3D cylinder for a pressure drop of 0.5 *bar. Pleat geometry was reconstructed by regular generic design. Both figures show a cross-section though the simulated cylinder*

3.7 Summary

In the present chapter model-based analysis of different pleated filter cartridges has been performed. Initially, cartridge A was used for establishing a standard procedure. Four different methods for the reconstruction of the pleat geometry were developed based on 2D microscopic images. The simulation results are used for calculating the water flow rate for the entire cartridge and are compared with experimental data. The image analysis method is the most laborious and proven to be the most accurate reconstruction method with the disadvantage of being restricted to the sector shown in the

image. Apart from the image analysis method, the deterministic irregular method also shows similar results by recreating each pleat with its real width and neglecting any other variations. Both approaches are more accurate in contrast to the regular generic design and the randomized irregular design which show much higher discrepancies between the experiments and the simulations. Nevertheless, the latter can be used in cases where a full sector geometry reconstruction is necessary but microscopic images are not available. For all studied models the simulated water flow rate was higher than the experimental when the fleece and the plastic cage were neglected. For all developed geometry reconstruction methods the models overpredict the flow rates in contrast to experimental data. The influence of the plastic cage on the flow rate was quantified and for the standard cartridge proved to be negligible. It was concluded that the complexity of the model can be reduced from 3D to 2D simulations.

The remaining discrepancy between the simulations and the measurements was caused by the fleece layer. Modeling was based on high quality microscopic images from prototypes built by Sartorius Stedim Biotech. The prototypes have similar configurations with the standard cartridge. In order to study the impact of the fleece layer the geometry was reconstructed in full detail using the image analysis method and three cartridges were analysed. Generally, it is difficult to measure the permeability of the fleece layers and such data weren't available in our case. Hence, the fleece permeability was estimated such that the simulation results match the experimental data. As a material property the fleece permeability doesn't depend on the pressure drop. However, the estimated permeability values are flow rate dependent. Therefore they are apparent values since some other properties are lumped into them, in particular fleece compression, which need to be further investigated. In addition, it was shown that if only two fleece permeabilities are known, simulations with interpolated values can predict the performance of the filter cartridge with a prediction error of the same uncertainty with the experiments. Furthermore, transfer of the fleece permeability across the three cartridges significantly reduced the difference between the simulations and the experiments in contrast to the cases where the fleece layers weren't studied. The impact of the plastic cage and its impact on the flow rate was found to be negligible for practically relevant design variants and operating conditions.

Finally, analysis of two other cartridges was performed in order to assess the impact of the pleat height on the water flow rate. These cartridges have different configurations compared to the ones analyzed above i.e. one membrane layer and considerably less pleats. Their analysis showed large variations from the respective measured water flow rates which were up to two orders of magnitude in the cases where the fleece layer was neglected. The addition of the fleece layer and the transfer of the fleece permeability between the two cartridges exhibited a surprising improvement in contrast to the previously studied cartridges. The impact of the plastic cage here was important due to the very low permeability of the fleece layer. However, such cases are mainly of academic interest and they are not important for industrial applications.

Chapter 4

Membrane Adsorbers

The content of the following chapter is based on the article: Eirini Velali, Birgit Stute, Martin Leuthold, Eric von Lieres "Model-based performance analysis and scale-up of membrane adsorbers with a cassettes format designed for parallel operation" Chemical Engineering Science Volume 192, 31 December 2018, Pages 103-113.

4.1 Introduction

The manufacturing of commercial drug therapeutics requires robust and cost-effective purification units [41]. Different chromatography modes are used for removing impurities such as affinity or hydrophobic interaction but among them the use of ion-exchange chromatography prevails [101]. Traditionally packed-bed chromatography has been used in this field but it demands large columns in order to process high volumetric flow rates.

The use of membrane adsorbers (MA)s can overcome the above limitations. One major advantage of MAs is that the molecules are transferred faster to the binding sites of the membrane because the main transport mechanism is convection [102]. MAs are used from small to large scales for capturing viruses or for removing DNA parts, host cell proteins and endotoxins for example [103]. These devices are typically disposable therefore minimizing the costs for cleaning, maintaining and sanitizing the equipment [104]. MAs can be found in market from several vendors at different configurations and sizes. Flat sheet membrane arrangements are common at lab scales whereas in produc-

tion scales the membranes are typically spirally wound or pleated around a cylindrical core.

Protein purification with MAs has been experimentally performed by different authors. Madadkar et al. [105] fabricated a device for hydrophobic interaction membrane chromatography for separation of monoclonal antibody (mAb) aggregates. The membrane in the device is configured in flat sheets and it has a bed volume of 0.4 mL. The authors reported that separation of mAb aggregates was achieved in less than the half time in comparison to size exclusion ultraperformance liquid resin chromatography and the operating pressure drop was about 100 times lower. In addition to pure experimental studies mathematical modeling and simulations are increasingly applied to evaluate the performance of MAs. In literature the studies can be divided into two areas: 1) one dimensional lumped models 2) computational fluid dynamics (CFD) in two or three dimensions. 1D models are easily computed but are not able to differentiate between the impact of non-ideal hydrodynamics and non-ideal binding to the total response of the system. Shiosaki et al. [106] used 1D modeling with axial dispersion for describing the adsorption of myoglobin and ovalbumin to a packed-bed adsorber and to a MA. Binding was described by the Langmuir model and it was shown that binding was flow rate dependent for ovalbumin and independent for myoglobin. In addition, the models predicted successfully the binding of myoglobin but it failed to predict the adsorption of ovalbumin.

Winderl et al. [107] tested whether fiber-based adsorbents can be mechanistically modeled. The model parameters were experimentally determined from a lab scale chromatography column packed with polymeric fiber stationary phases that have 40 mm bed height. In their study, they combined a transport-dispersive model (TSD) with a steric mass action (SMA) isotherm. The results showed good description of the hydrodynamics behaviour in the column and accurate reproduction of the breakthrough and elution curves of three proteins with different sizes. Vicente et al. [108] evaluated the performance of a commercial anion-exchange MA in purifying viruses or virus-like particles (VLP)s. The results revealed an optimum range of pH and ionic strength where the recovery was maximum. Furthermore, the obtained results from the combination of the equilibrium dispersive model (EDM) with the SMA model showed a good agreement

with the experiments. Frerick et al. [109] designed a standard modeling procedure of downstream processes which includes simulation of ion-exchange MA, ion-exchange and size-exclusion chromatography and ultra-diafiltration. The SMA isotherm has been applied and the parameters were determined from bovine serum albumin (BSA) and immunoglobulin G (IgG) experiments. The comparison of simulation results with experiments showed good agreement. Dimartino et al. [110] used an one dimensional model for the purification of IgG to affinity membranes. The authors used the Langmuir model for descibing the adsorption of IgG to the membranes and they modeled the loading, washing and elution step. The simulations were compared to experimental data obtained from new affinity membranes and the results were in good agreement.

In contrast to lumped models, CFD simulations are computationally more expensive but the geometry of the MAs and the influence of the properties of the membrane are not modeled depending on each other. Orthogonal modeling is a key prerequisite for identifying and quantifying the causes of non-deal system behaviour. Moreover, it enables to transfer membrane related data across the scales. Ghosh et al. [111, 112] have used CFD modeling for commercial ion-exchange MAs with different flow configurations and sizes. Accurate prediction of breakthrough curves (BTC) under non-binding conditions was achieved without model parameter estimation. The simulations are based only on the device's geometry which was either given by the manufacturer or reconstructed with the use of magnetic resonance imaging (MRI) [113]. For the purpose of understanding the binding mechanism the CFD models were coupled to the binding isotherms. The parameters of the binding isotherms were estimated from BTC data of BSA under binding conditions. The binding parameters are transferred across scales since the non-idealities in hydrodynamics and in the binding procedure were decoupled.

4.1.1 Scope of this work

The present work builds on the studies performed by Ghosh et al. [112]. It follows a modeling approach that allows to predict the behaviour of different MAs across scales. The influences of non-ideal flow and non-ideal binding are decoupled in the models of the studied MAs, consequently the binding parameters that are estimated from one MA

can be transferred across different capsules. Analysis of four different MAs is presented at three different flow rates. The MAs were provided by Sartorius Stedim Biotech. Exceeding the scope of Ghosh et al. [112] where Pico with 0.08 *mL* membrane volume and another device with 1.2 *L* membrane volume were studied, here additionally Nano with 3 *mL* membrane volume is studied and Cassettes with 1.6 *L* membrane volume. The Cassettes system has recently become commercially available. The membrane has a flat sheet configuration and can be obtained with a bed volume of 0.8 *L* or 1.6 *L* and at a bed height of 4 *mm* or 8 *mm*. In a conventional holder up to 13 Cassettes can be operated in parallel. Larger holders allow to operate 20 and more Cassettes in parallel. Furthermore, in contrast to Ghosh et al. [112] where the binding parameters were estimated from Pico 0.08 *mL*, here they are estimated from a reference device with 1.2 *L* membrane volume because it has shown a much more robust performance. Then these parameters are transferred to the Cassettes and to two additional MAs with membrane volumes of 0.8 *mL* and 3 *mL*. At last, studies have been performed for parallel Cassettes operation under non-binding and binding conditions.

4.2 Theory

4.2.1 System Dispersion

A typical MA has a much lower bed height in comparison to packed bed chromatography. Although recent advances in this field have lead to MAs with highly optimized holdup volumes, in small scales holdup volumes can be very large in comparison to the bed volume. The volume of the system, Vm_{sys} consists of: 1) membrane pores, Vm_{pore}, 2) internal channels, etc., Vm_{int}, and 3) external tubing, connectors, etc., Vm_{ext}. Lumped models usually take into account the sum of internal and external holdup volumes [114, 115, 110], eq. (4.1a) in contrast to CFD models [111, 112, 116], eq. (4.1b).

$$Vm_{sys} = Vm_{pore} + Vm_{holdup} \qquad \text{lumped} \qquad (4.1a)$$

$$Vm_{sys} = Vm_{pore} + Vm_{int} + Vm_{ext} \qquad \text{CFD} \qquad (4.1b)$$

External volumes, Vm_{ext} can cause time-lag and dispersion. In 1D models, $Vm_{holdup} = Vm_{int} + Vm_{ext}$, are usually described by a plug flow reactor (PFR), eq. (4.2a), a continuous stirred tank reactor (CSTR), eq. (4.2b), or a series of such elements. The time-shift caused by the PFR can be applied at all steps of the study because the results will not change. When the CSTR is placed before the MA analytical solutions are obtained whereas in the case that the CSTR is after the MA then the system needs to be solved numerically.

$$c(t) = c_{in}(t - \tau) \qquad \text{PFR} \qquad (4.2a)$$

$$\frac{dc}{dt}(t) = \frac{c_{in}(t) - c(t)}{\tau} \qquad \text{CSTR} \qquad (4.2b)$$

4.2.2 Binding models

A binding model that took into account the kinetics of molecule adsorption to and desorption from the sorbent is essential. In this study the Langmuir [117, 114] and the spreading [118] isotherms are compared. Both models have been previously employed in order to describe adsorption of BSA on anion-exchange membrane [111, 112]. The Langmuir model assumes that the molecules are homogeneously adsorbed on the membrane surface and once they are adsorbed their conformation state remains the same (Fig. 4.1a). In addition, this model is based on the assumption that there is no interaction between the molecules and that there is no difference between the binding sites. The traditional Langmuir model is described in eq. (4.3) where k_a and k_d are the adsorption and desorption rates and q_m is the maximum binding capacity.

The spreading model assumes that a molecule can initially bind in one state a surface but it can change binding state during reorientation or spreading (Fig.4.1b). This model is described in eq. (4.4) where $k_{a,1}$, $k_{a,2}$ are the two adsorption states and $k_{d,1}$, $k_{d,2}$ are the desorption states. The transition between the different states is described by the rates k_{12} and k_{21}. The maximum binding capacity of both states is given by q_m and $\beta \geq 1$ describes the ratio of occupied surface area at the different states.

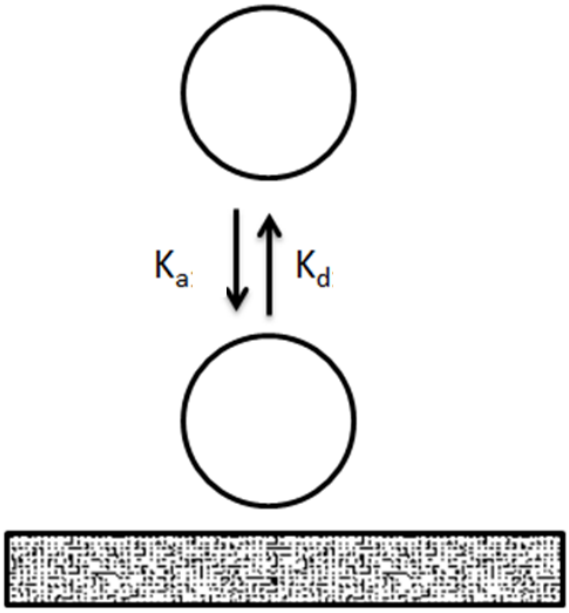

(a) Langmuir binding model

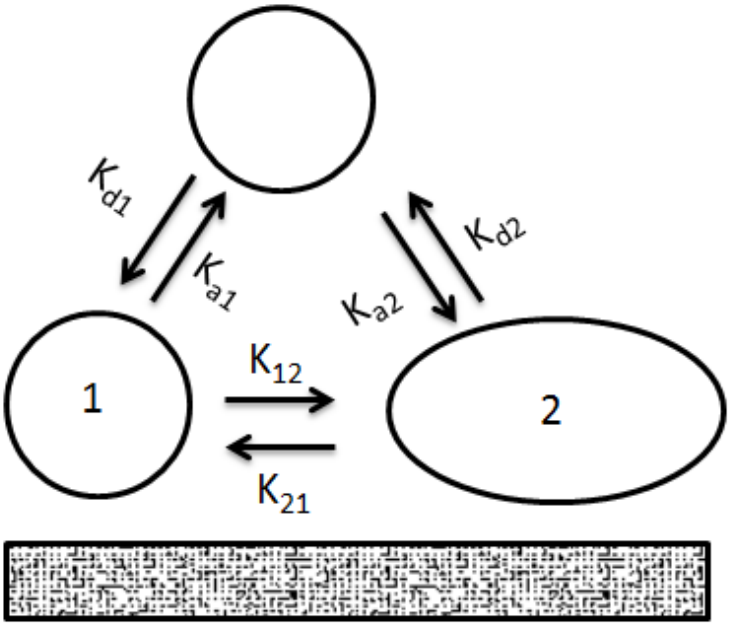

(b) Simplified spreading model

Figure 4.1: Schematic of binding mechanisms (adapted from [119])

$$\frac{dq}{dt} = k_a(q_m - q) - k_d q \tag{4.3}$$

$$\frac{dq}{dt} = \frac{dq_1}{dt} + \frac{dq_2}{dt} \tag{4.4a}$$

$$\frac{dq_1}{dt} = (k_{a1}c - k_{12}q_1)(q_m - q_1 - \beta q_2) + k_{21}q_2 - k_{d1}q_1 \tag{4.4b}$$

$$\frac{dq_2}{dt} = (k_{a2}c + k_{12}q_1)(q_m - q_1 - \beta q_2) - k_{21}q_2 - k_{d2}q_2 \tag{4.4c}$$

Since the resulting fits do not lead to different residuals, adsorption and desorption to and from the second bound state is not considered in this study, $k_{a2} = 0$ and $k_{d2} = 0$.

4.3 Experimental

BTC data for the four different MAs were provided by Sartorius Stedim Biotech. Pico (0.08 mL) and Cassettes (1.6 L) have axial flow configurations whereas Nano (3 mL) and the reference device (1.2 L) have radial flow configurations. All four MAs contain the same membrane but not necessarily from the same membrane batch. A strong ion-exchange membrane is packed which is functionalized with quaternary ammonium groups on a stabilized reinforced cellulose matrix. The membrane in every MA is from different batches and this can cause capacity variations that will be further discussed later. The porosity of the membrane is $\varepsilon = 80\%$. Pico (0.08 mL) has a bed height of 4 mm whereas in Nano, the reference device and Cassettes the bed height is 8 mm. Experiments were performed at flow rates of 2 $\frac{MV}{min}$, 4 $\frac{MV}{min}$ and 6 $\frac{MV}{min}$ for Nano (3 mL), the reference device (1.2 L) and the Cassettes (1.6 L) where MV denotes the membrane volume. For Pico (0.08 mL) experiments were performed at flow rates of 5 $\frac{MV}{min}$, 10 $\frac{MV}{min}$ and 15 $\frac{MV}{min}$. The concentration of BSA was 2 g/L for Nano (3 mL), the reference device (1.2 L) and the Cassettes (1.6 L) and 1 g/L for Pico (0.08 mL). Furthermore, KPi buffer was used. For each device, BTC data was measured under three conditions: 1) by-

pass without the MA, 2) non-binding conditions with 1% acetone in 10 mM phosphate buffer at pH 7 and 1.6 mS conductivity and 3) binding conditions with BSA in 10 mM phosphate buffer at pH 7 and 1.6 mS conductivity.

4.4 Results and discussion

Four different MAs have been analyzed. First the reference device with 1.2 *L* membrane is studied. For all studied devices flow profile studies will be performed. Then predictive simulations will be performed under non-binding conditions based on the geometry of the MA. At last, the binding parameters that are estimated from the reference device will be transferred to the other three MA in order to predict the breakthrough curves under binding conditions.

4.4.1 Numerical accuracy

As explained before mesh independency studies are necessary and were performed for the case of MAs as well. The approximate mesh size of each model is shown in Tab. 4.1. For the 2D meshes triangular elements were used and tetrahedral elements were used in 3D meshes. A swept mesh with hexahedral elements was built for the middle part of the Cassettes system after the model was simplified. For all fluid flow simulations P_2+P_1 element discretization was used. For all mass transfer simulations linear element discretization was used. The results were obtained with the direct solver MUMPS.

Table 4.1: Mesh sizes of the applied CFD models

MA	Applied mesh elements	Refined mesh elements	Relative error %
Reference device 1.2 *L*	600.000	1.000.000	−0.01
Pico 0.08 *mL*	135.000	250.000	+0.17
Nano 3 *mL*	60.000	180.000	+0.24
Cassettes 1.6 *L* inlet part	3.000.000	4.700.000	+0.73
Cassettes 1.6 *L* middle part	320.000	700.000	+0.90
Cassettes 1.6 *L* oulet part	3.000.000	4.700.000	+0.71

4.4.2 Reference device (1.2 *L*)

The reference device has highly optimized channel design and holdup volumes, Vm_{int}, in comparison to the membrane volume, Vm_{pores}. It has a radial flow configuration in which the membrane is spirally wounded around the core. The fluid enters from a thin void ring at the perimeter of the capsule and exits from the thin ring and channels at the inner periphery of the device. Owing to the geometry which was reconstructed based on technical drawings, symmetry can be exploited to reduce the computational geometry. A representative 2D axial cross section of the device is considered. The velocity profile is computed under steady state conditions. From Fig. 4.2 it can be observed that the flow is homogeneously distributed in the membrane stack.

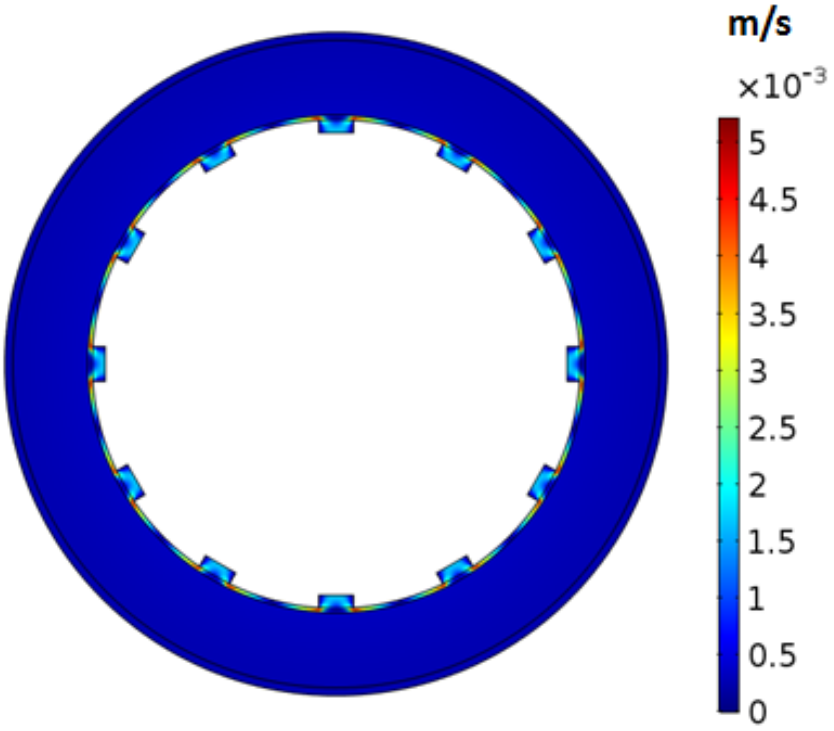

Figure 4.2: Flow magnitude of reference device (1.2 L) with rotational symmetry at a flow rate of 2 $\frac{MV}{min}$ *[120]*

The external holdup volumes of the capsule such as the end caps, tubes, valves etc. are modeled as a PFR and CSTR in series and are estimated from experimental data under non-binding conditions as shown in Tab. 4.2.

Table 4.2: External volumes, Vm_{ext}, as modeled by a PFR and CSTR in series with volumes estimated from non-binding BTC data [120]

Device	$Membrane\ Volume(MV)$	Vm_{PFR}	Vm_{CSTR}
Reference	1.2 L	360 mL	200 mL
Pico	0.08 mL	1.04 mL	0.21 mL
Nano	3 mL	1.10 mL	0.10 mL
Cassettes	1.6 L	130 mL	20.0 mL

The prediction under non-binding conditions is shown in Fig. 4.3a, 4.3c and 4.3e for the different flow rates. As discussed before, two binding models have been applied and their ability to reproduce the breakthrough curves (BTC) has been compared. The Langmuir isotherm fails to describe the tailing part as the membrane reaches saturation in contrast to the spreading model as shown in Fig. 4.3b, 4.3d and 4.3f. The breakthrough curves can only be accurately reproduced if the rate parameters, k_{a1} and k_{d1} are dependent on the flow rate. The binding sites of the membrane are reached by a combination of convective transport in the membrane pores and diffusive transport in a stagnant surface boundary layer and therefore with increasing flow rate the binding rate will increase. In addition, with increasing flow rate the convective contribution to the transport towards the surface is enhanced and hence the binding rate increases. However, the rest of the parameters and in particular the equilibrium constant $k_{eq} = \frac{k_{a1}}{k_{d1}}$ don't depend on the flow rate. The estimated binding parameters are shown in Tab. 4.3.

Table 4.3: Binding parameters of spreading model as estimated for reference device at different flow rates [120]

Parameter	2 $\frac{MV}{min}$	4 $\frac{MV}{min}$	6 $\frac{MV}{min}$	Unit
k_{a1}	1.30	2.30	3.00	$\frac{m^3}{s\ mol}$
k_{d1}	0.0074	0.0130	0.0170	$\frac{1}{s}$
k_{eq}	177	177	177	$\frac{m^3}{mol}$
k_{12}	3.75	3.75	3.75	$\frac{m^3}{s\ mol}$
k_{21}	0.70	0.70	0.70	$\frac{1}{s}$
q_m	2.47	2.47	2.47	$\frac{mol}{m^3}$
β	1.86	1.86	1.86	–

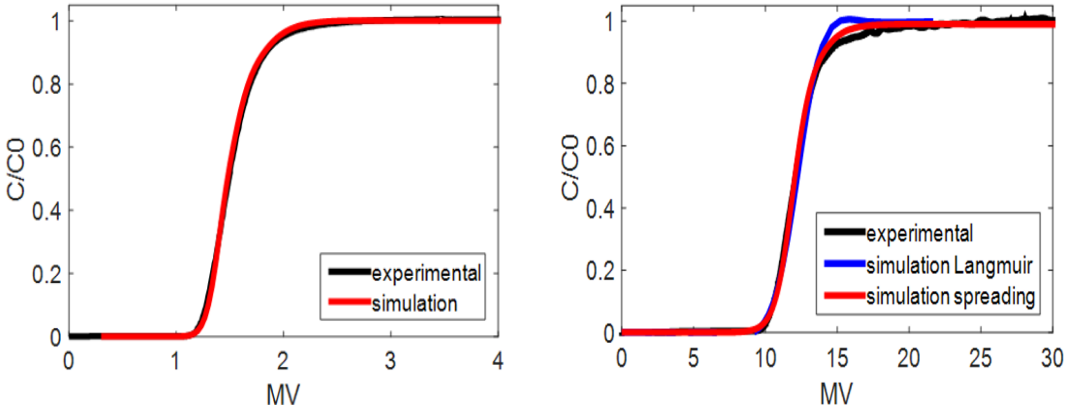

(a) Non-binding BTC at 2 $\frac{MV}{min}$

(b) Binding BTC 2 $\frac{MV}{min}$

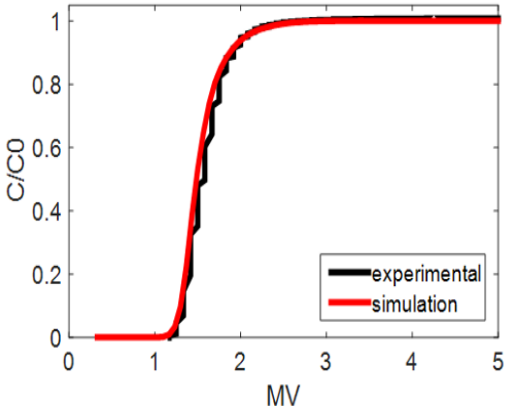

(c) Non-binding BTC at 4 $\frac{MV}{min}$

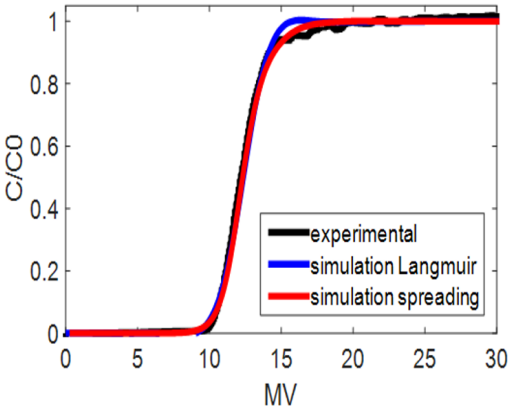

(d) Binding BTC at 4 $\frac{MV}{min}$

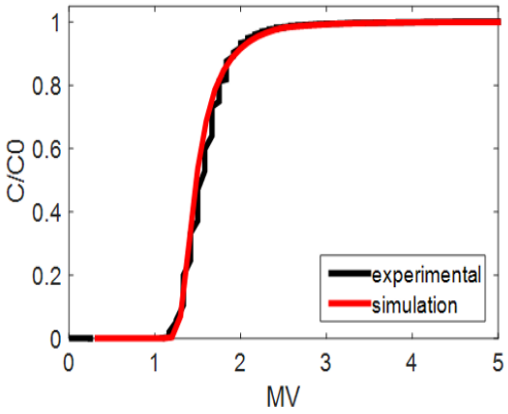

(e) Non-binding BTC at 6 $\frac{MV}{min}$

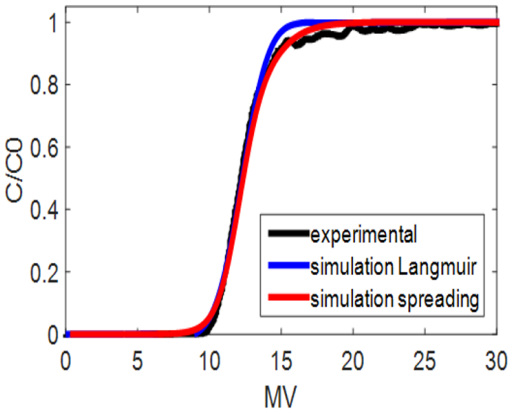

(f) Binding BTC at 6 $\frac{MV}{min}$

Figure 4.3: Simulated (red/blue) and measured (black) BTC of reference device 1.2*L under non-binding (left) and binding (right) conditions at different flow rates [120]*

4.4.3 Pico device (0.08 *mL*)

Pico capsule has a membrane volume of 0.08 *mL*. It has axial flow configuration and is designed for polishing applications at low quantities. The geometry was reconstructed

based on a magnetic resonance image (MRI), as shown in Fig. 4.4a. Axially there are 5 membrane stacks and each one of them consists of three membrane layers. The membrane stacks are separated by O-rings and are divided into 3 regions radially: 1) the central 2) the intermediate and 3) the clamped region. Due to the compression of the intermediate and clamped regions their porosities have been correspondingly reduced. A 2D model with radial symmetry is representative for the entire device. The hydrodynamics result is shown in Fig. 4.4b where it can be observed that the flow is homogeneously distributed in the central membrane region, the intermediate regions (where the membrane thickness decreases) exhibit lower velocities and the clamped regions show velocities close to zero. The external holdup volumes have been estimated from BTC data under non-binding conditions and are shown in Tab. 4.2. From Fig. 4.5a, 4.5c and 4.5e it is observed that the experimental breakthrough curves under non-binding conditions show good reproducibility. For the reproduction of the BTC under binding conditions the binding parameters that were estimated for the reference device are used in the spreading model. The predicted curves are compared to corresponding measurements in Fig. 4.5b, 4.5d and 4.5f using the binding parameters from Tab. 4.3. From these figures it can be observed that the experimental breakthrough curves have different positions for the highest flow rate. This indicates a difference regarding the membrane capacity which can be explained by charge-to-charge membrane capacity variations from different membrane batches during the manufacturing.

4.4.4 Nano device (3 *mL*)

The Nano device has a radial flow configuration such as the 1.2 *L* device. The geometry was reconstructed in COMSOL based on technical drawings and on a MRI image (Fig. 4.6a). Rotational symmetry was exploited in this case as well. Accurate reconstruction of the geometry was challenging in comparison to the previously analyzed MAs due to variances in the final assembly. At the welding step the plastic is molten. The plastic parts are pressed together and hence the pieces are glued and the excess plastic is collected by a nozzle. In addition, during the assembly the dimensions of the upper horizontal part can slightly change. The simulated flow magnitude result is shown

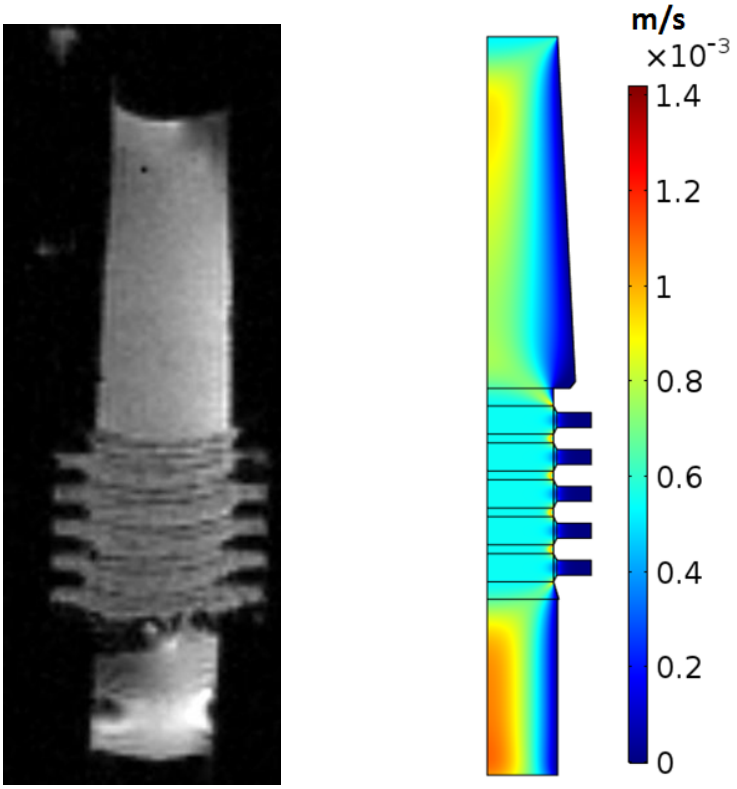

(a) MRI *(b) CFD*

Figure 4.4: Geometry reconstruction and flow magnitude for Pico (0.08 mL) device at flow rate 5 $\frac{MV}{min}$

in Fig. 4.6b. The comparison of experiments and simulations under non-binding conditions is shown in Fig. 4.7a, 4.7c and 4.7e. It is observed that although the geometry has been reconstructed in a detailed way the reproduction of the breakthrough curves isn't as accurate as for the reference device where the experimental reproducibility is good. As for other devices, the external holdup volumes are modeled by a PFR and CSTR from experimental data under non-binding conditions and the values are shown in Tab. 4.2.

The binding parameters that were estimated for the reference device (Tab. 4.3) are transferred in order to predict the performance of Nano under binding conditions and the results are shown in Fig. 4.7b, 4.7d and 4.7f. These figures show that the data sets exhibit much larger variations under binding conditions for all three flow rates. The experimental breakthrough curves vary in position as for the Pico device and in shape. The difference in the position of the curves can be explained by the charge-to-charge

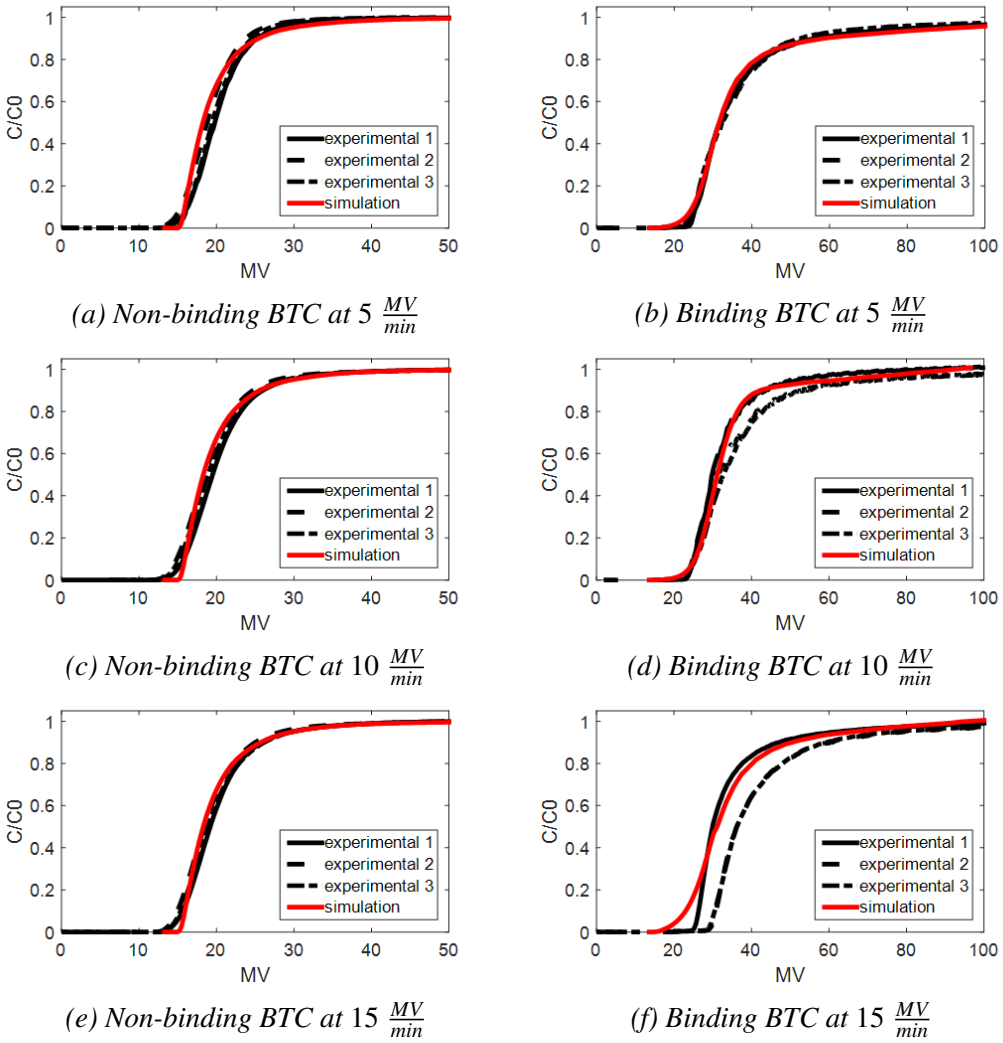

(a) Non-binding BTC at 5 $\frac{MV}{min}$ *(b) Binding BTC at* 5 $\frac{MV}{min}$

(c) Non-binding BTC at 10 $\frac{MV}{min}$ *(d) Binding BTC at* 10 $\frac{MV}{min}$

(e) Non-binding BTC at 15 $\frac{MV}{min}$ *(f) Binding BTC at* 15 $\frac{MV}{min}$

Figure 4.5: Simulated (red/blue) and measured (black) BTC of Pico 0.08*mL under non-binding (left) and binding (right) conditions at different flow rates*

variations in membrane capacity. However, the different shapes of the breaktrough curves above 80% breakthrough have been observed by other researchers. The cause is not exactly known but we hypothesize that it can be attributed to the variability caused by the molten process. As a matter of fact, one data set is predicted very accurately by the simulations. However, due to the given variability, this result can't be considered to be representative for the general case.

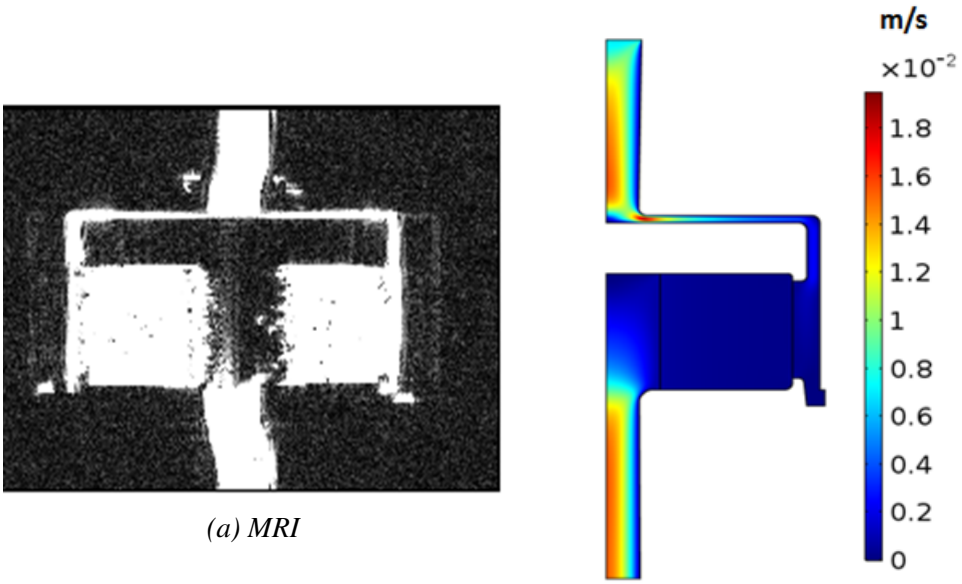

(a) MRI

(b) CFD [120]

Figure 4.6: Geometry reconstruction and flow magnitude for Nano (3 mL) device at flow rate 2 $\frac{MV}{min}$

4.4.5 Cassettes ($\geq$ 1.6 L)

The Cassettes system has a flat sheet membrane configuration and a highly complex geometry. The design has evolved from the plate and frame filter press which allows filtration of large volumes. The membrane is placed in rectangular frames, the beams, which are fixed by a stainless steel holder [121, 122, 25]. Left to right in Fig. 4.8 it is shown: 1) inlet manifold, 2) filter plate, 3) membrane stack, 4) spacer plate, 5) membrane stack, 6) filter plate, 7) outlet manifold. The inlet manifold is connected to the middle plate with a large channel and the outlet plates are connected through a second channel. The central spacer plate is where the flow enters and then it is divided into two streams left and right at the membrane stacks. After that the liquid is collected in the filter plates. Between the manifold plates up to 13 (standard holder) and more cassette systems can operate in parallel. The CAD files were provided by Sartorius Stedim Biotech. Since it isn't possible to assume symmetries along any axes, 3D simulations have to be performed. Due to the highly complex geometry the channels that connect the middle part with the inlet and the outlet parts are cut through and the system is simulated in three steps: 1) the inlet manifold part, 2) the cassettes and 3) the outlet

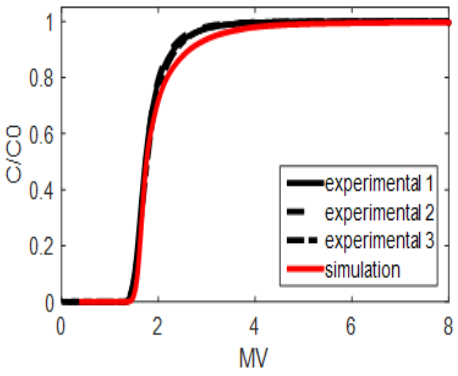

(a) Non-binding BTC at 2 $\frac{MV}{min}$

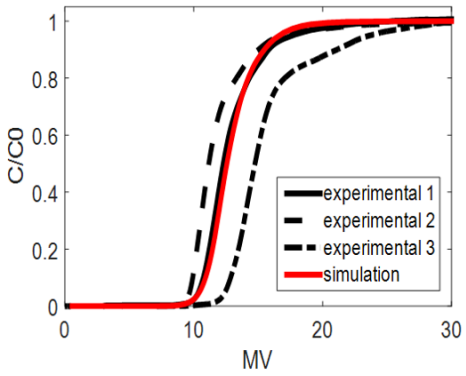

(b) Binding BTC at 2 $\frac{MV}{min}$

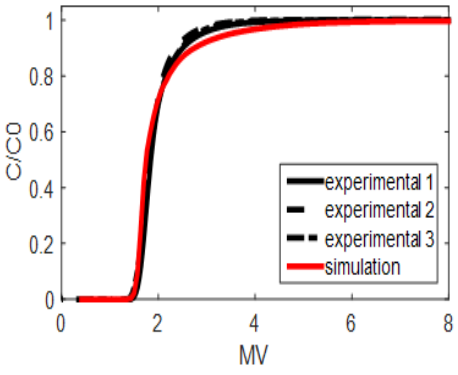

(c) Non-binding BTC at 4 $\frac{MV}{min}$

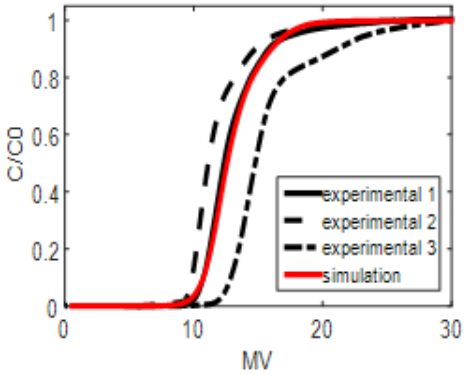

(d) Binding BTC at 4 $\frac{MV}{min}$

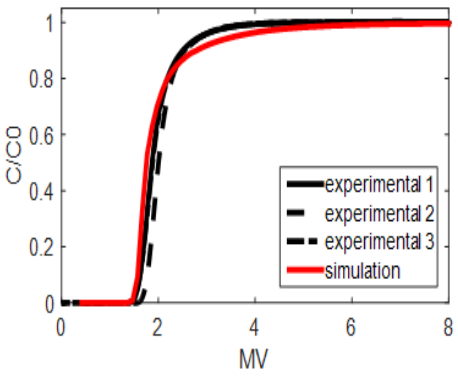

(e) Non-binding BTC at 6 $\frac{MV}{min}$

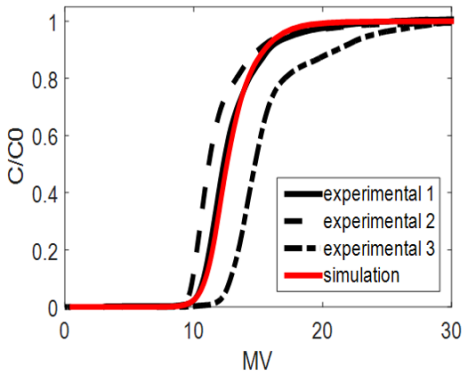

(f) Binding BTC at 6 $\frac{MV}{min}$

Figure 4.7: Simulated (red/blue) and measured (black) BTC of Nano 3mL under non-binding (left) and binding (right) conditions at different flow rates [120]

manifold (Fig. 4.9). Every study is connected to the next one by using the results of the upstream parts as boundary conditions for simulating the downstream parts. The flow in the Cassettes system in most regions belongs to the laminar regime. In and around the small channels that connect the Cassettes with the inlet and outlet manifolds the flow belongs to the transient regime. However, the geometry differs from the standard

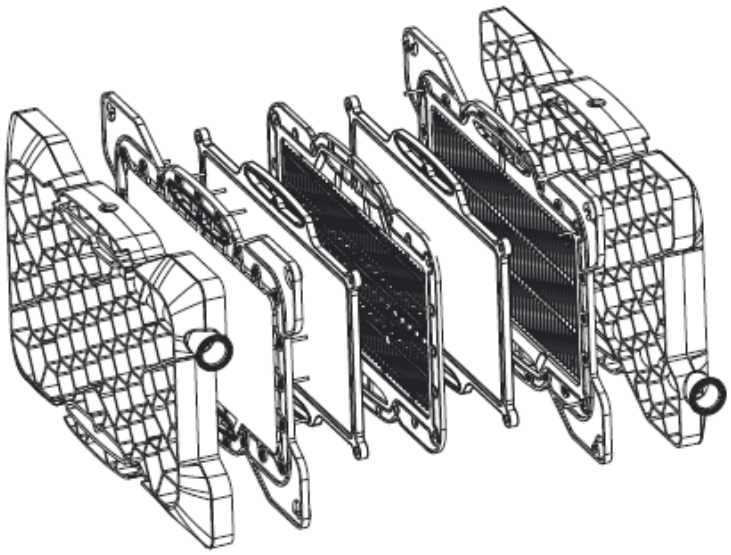

Figure 4.8: Schematic of Cassettes (courtesy of Sartorius Stedim Biotech) [120]

pipe or slab for which the Reynolds number is defined. Hence, comparative simulations of laminar and turbulent flow modules have been performed in COMSOL in order to assess the differences. The results revealed that although the flow profiles in these regions differ, the mass transfer results under non-binding and binding conditions are in good agreement as shown in Fig. 4.10. Therefore, the laminar flow module has been applied since it requires less computational time. The flow profile study for the spacer and filter plates is shown in Fig. 4.11a and 4.11c. From Fig. 4.11b it is shown that the flow is homogeneously distributed over the membrane stack. It is observed that the velocity is higher at the vicinity of the connection channels at the top of the space plate and at the bottom of the filter plates. For further simulations, the complicated geometry of the Cassettes has been simplified. A 3D geometry with the same dimensions as the original has been constructed without the thin structures of the spacer and filter plates. Simulations of the original and the simplified geometry show that the bars and struts present insignificant differences in the mass transport results. Hence, the simplified geometry has been used in the following simulations to reduce the computational effort. The simplified geometry also allows to exploit mirror symmetry which halves the computational time.

The external holdup volumes have been modeled by a PFR and CSTR in series

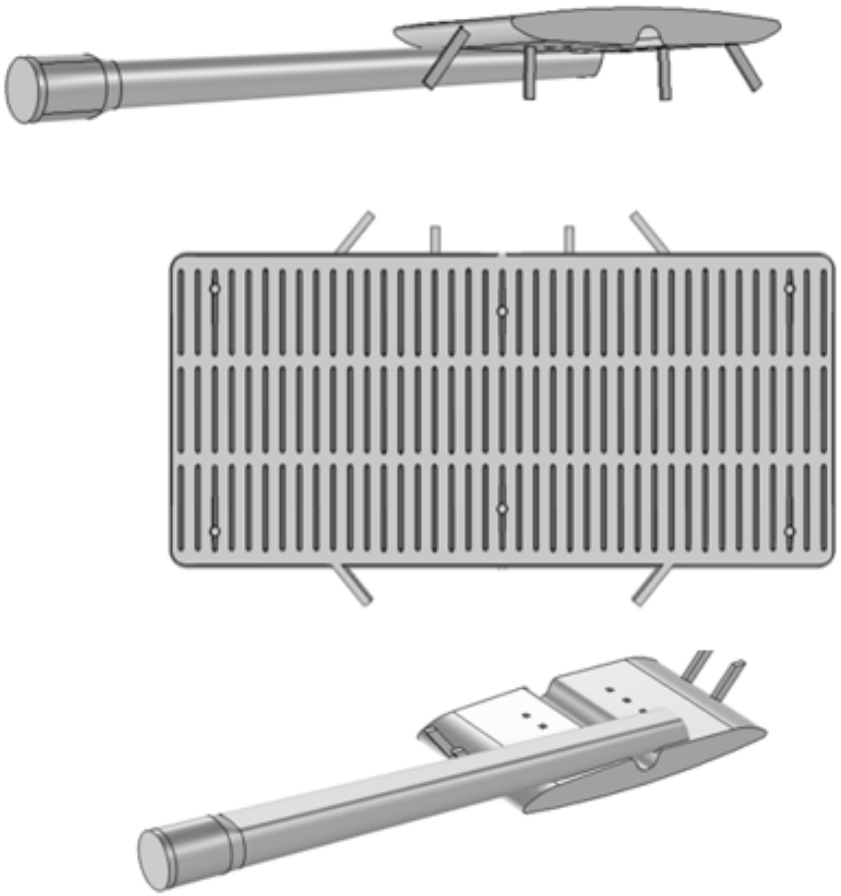

Figure 4.9: Sequential solution procedure

whose sizes have been estimated from non-binding BTC, Tab. 4.2. The breakthrough curves under non-binding conditions are shown in Fig. 4.12a, 4.12c and 4.12e. The spreading model and the binding parameters that were estimated for the reference device have been used for predicting the BTC under binding conditions, Tab. 4.3. From Fig. 4.12b, 4.12d and 4.12f it is shown that the predicted BTC can match very well the shape but not the position of the curve. This can again be explained by charge-to-charge membrane capacity variation during the manufacturing process while usually only the minimum capacity is specified by the vendors. In this case, the capacity had to be adjusted by 8.5 % which is within the range of previously analyzed capacity variations.

At last, parallel operation of Cassettes has been studied. One Cassettes system is compared to two and four Cassettes between one set of manifolds at a flow rate of

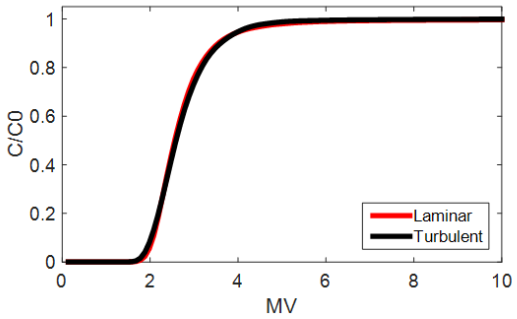

(a) Non-binding

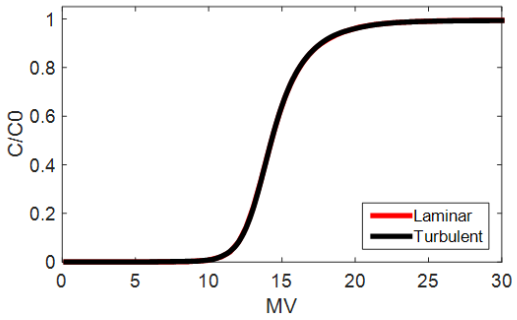

(b) Binding

Figure 4.10: Simulated BTC of Cassettes without manifolds under a) non-binding and b) binding conditions at flow rate 6 $\frac{MV}{min}$ *comparing the laminar and turbulent flow modules [120]*

$2MV/min$. The sequential solution procedure is also applied in this case and the simulation results are shown in Fig. 4.13. For the prediction under binding conditions the simulation results of serial and parallel operation reveal good scalability of the system under the condition that the membrane properties are the same.

In addition, simulations with 4 mm bed height were performed. In this case experimental BTC curves were not available. Fig. 4.14a shows the BTCs under non-binding conditions for all three different flowrates and the results under binding conditions are shown in Fig. 4.14b

4.5 Summary

A brief summary is given here before the final conclusions which will be presented in the following chapter. Four different membrane adsorbers with different flow configurations and various membrane volumes from 3 mL to 1.6 L were studied. The

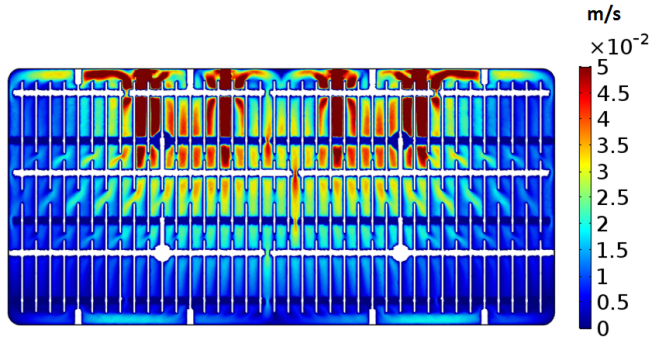

(a) Flow in central spacer plate

(b) Flow in membrane stack

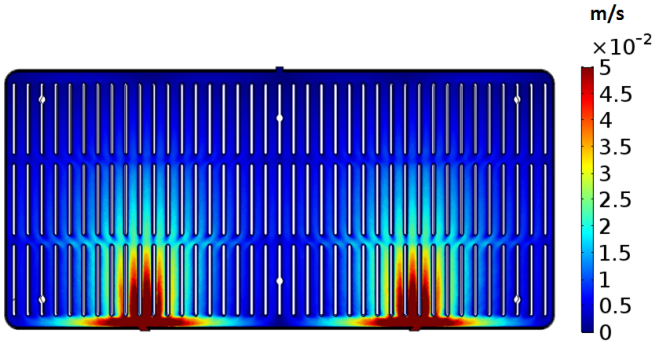

(c) Flow in outer filter plates

Figure 4.11: Flow magnitude for Cassettes as simulated at flow rate 2 $\frac{MV}{min}$ [120]

experimental breakthrough curves under non-binding conditions were compared with the simulated in order to validate the geometry of the MAs. For calibrating the model under binding conditions only one experimental breakthrough curve is needed and then the estimated parameters can be transferred to the other models. The flow profile studies were calculated by solving Navier-Stokes equations for the void regions and Brinkman's equations for the porous regions. The external holdup volumes were modeled as a PFR and CSTR in series and their sizes were estimated from BTC data under non-binding conditions. For the prediction of the BTC under binding conditions the spreading model

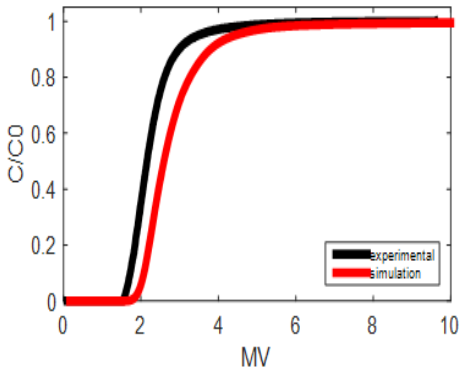

(a) Non-binding BTC at 2 $\frac{MV}{min}$

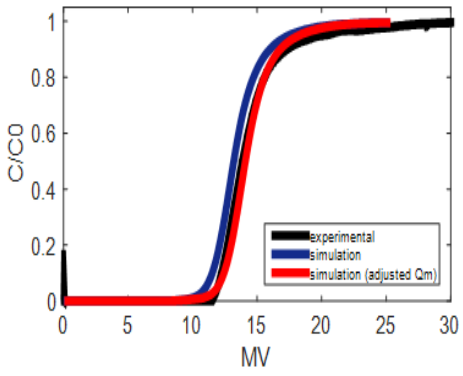

(b) Binding BTC at 2 $\frac{MV}{min}$

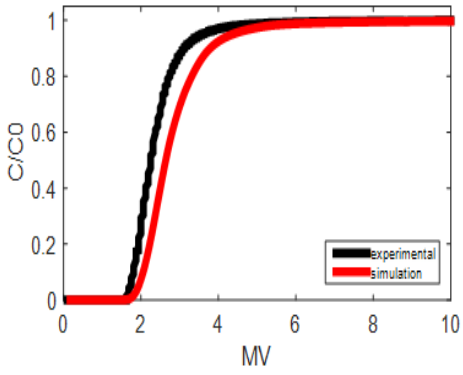

(c) Non-binding BTC at 4 $\frac{MV}{min}$

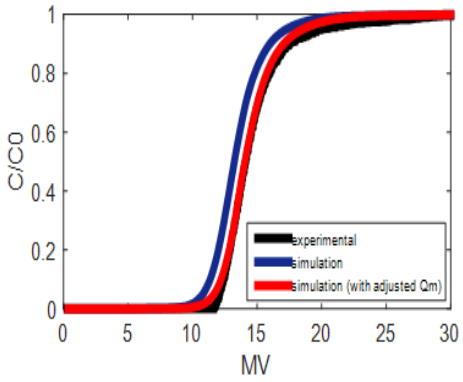

(d) Binding BC at 4 $\frac{MV}{min}$

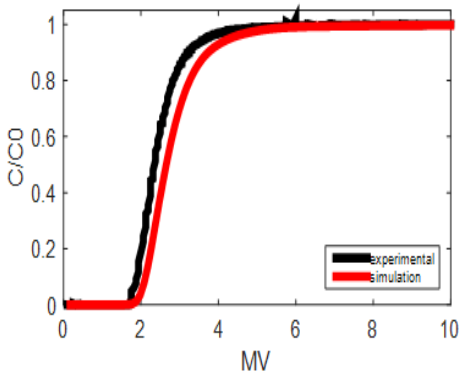

(e) Non-binding BTC at 6 $\frac{MV}{min}$

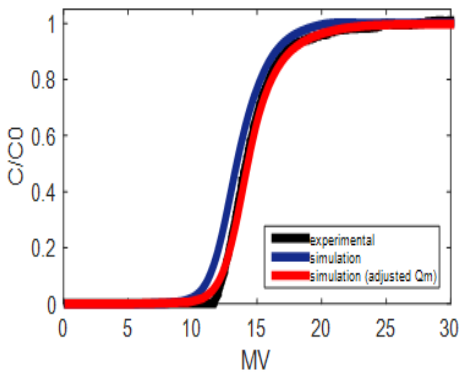

(f) Binding at 6 $\frac{MV}{min}$

Figure 4.12: Simulated (red/blue) and measured (black) BTC of Cassettes 1.6*L under non-binding (left) and binding (right) conditions at different flow rates [120]*

was applied in agreement with previous studies and the binding parameters were estimated for the reference device 1.2 *L* and transferred to other devices. The study revealed that the rate constants are flow rate dependent which can be explained by the fact that the binding sites of the membrane are reached by convective and diffusive transport. The other parameters and the equilibrium constant remain the same for all flow rates.

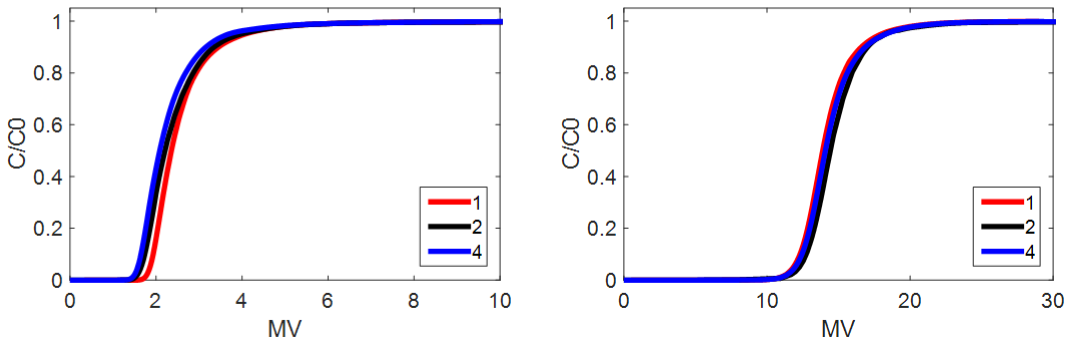

(a) Non-binding conditions *(b) Binding conditions*

Figure 4.13: Simulated BTC of one, two and four Cassettes in parallel operation at flow rate 2 $\frac{MV}{min}$ *[120]*

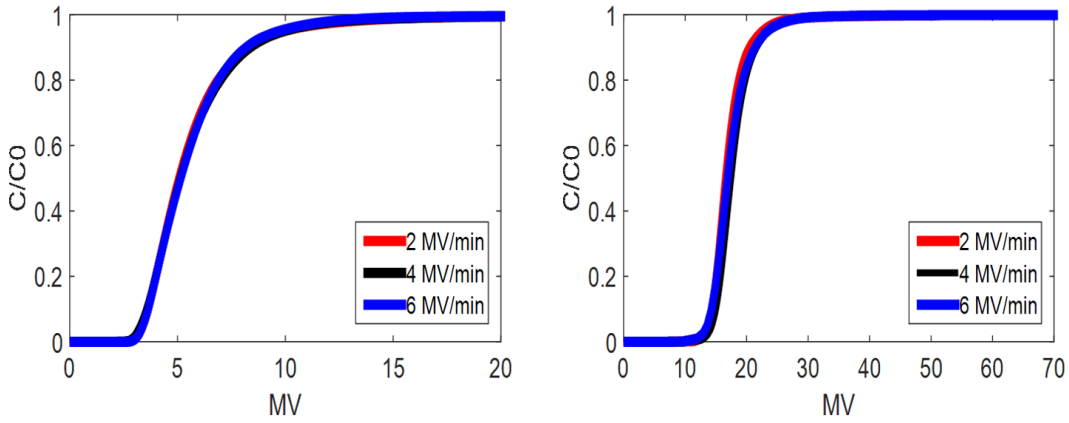

(a) Non-binding conditions *(b) Binding conditions*

Figure 4.14: Simulated BTC of Cassettes with 4 *mm bed height at different flow rates under non-binding (left) and binding (right) conditions*

The geometries of the two smaller MAs were reconstructed based on MRI data whereas technical drawings were used for the reconstruction of the reference device. Although for these membrane adsorbers 2D models were representative, for the cassette system simulations in three dimensions were necessary. For the Cassettes system 1.6 L a simplified geometry was developed without details which are not important.

The experimental data for the Pico with 0.08 mL membrane volume and especially for Nano with 3 mL membrane volume were poorly reproduced by the model. In particular, discrepancies in position and at the shape of the BTC were observed. Variance in the position of the curves can be caused by charge-to-charge capacity variation during the manufacture process. It was shown for Cassettes that the BTC under binding con-

ditions can be predicted if the binding capacity of the membrane is adjusted. Multiple Cassettes systems were simulated in parallel operation and the results revealed good scalability of the system. If the membrane properties are the same then modeling parameters that are estimated from one device can be transferred to others for predicting their performance.

Chapter 5

Conclusions

This thesis is concerned with membrane based separation processes. The separation mechanism in filter cartridges is size exclusion whereas in MAs is selective binding. Different sizes and flow configurations are commercially available. The number of membrane layers in filters is one or two whereas in membrane adsorbers a dozen or more layers are used in order to achieve a larger bed height. Large bed heights are not required for surface filtration since they can only be beneficial for separation processes which take place inside the membrane, for example in the case of membrane adsorbers. However, bigger pores can be used which decrease the pressure drop. Fleece layers are usually placed before and after the membranes in order to keep them in a fixed position. These fleece layers have a much higher permeability than the membrane. In pleated filter cartridges and in membrane adsorbers there is an interplay of hydrodynamics in the device and interactions between the solute molecules and the membranes at the molecular level. Generally molecular interactions with the outer and inner membrane surfaces are less well known than hydrodynamics and in the literature there is a variety of hypotheses and different modeling approaches for describing these interactions. In addition, the impact of the fleece on the performance of pleated filter cartridges is not well understood. This study is focused on fresh unused capsules. For filter cartridges, surface interactions are not considered. In situ measurements of hydrodynamics and of surface interactions, such as binding, are difficult to obtain. The contribution of different mechanisms can be analyzed using models and used for scale-up. The modeling work-flow has generally three parts: 1) hydrodynamics 2) mass transfer under non-retaining

conditions 3) mass transfer under retaining conditions. Regarding the first step, when the geometry of such devices is known the hydrodynamics can be fully predicted. For the membranes, material properties such as the intrinsic permeability, k and the porosity ε are typically known. For membrane adsorbers simulations under non-binding conditions where compared to experimental breakthrough curves in order to validate the hydrodynamics. However, for filters the retention mechanism is always active hence non-retaining mass transfer experiments can not be usually performed. The real separation or purification can only be simulated by combining the second and third step with surface interaction models. For filters that would be size-exclusion mechanisms, pore blocking etc. whereas for membrane adsorbers molecular binding with for example ion-exchange or affinity membranes etc. In this thesis hydrodynamics were extensively studied for different types of pleated filter cartridges and membrane adsorbers. For the pleated filter cartridges fresh filters were used and the retention mechanism was not studied, while for the membrane adsorbers the retention mechanism has been included.

5.1 Filter cartridges

For modeling pleated filter cartridges the most important feature is to reconstruct the geometry of the pleat structure. Four different approaches have been proposed for solving this problem. Standard operating procedures for all are provided and results are compared showing that it can depend on the application which is the best to use because they differ greatly in detail and effort.

In filtration devices there are three major contributions to the overall mass transfer resistance. 1) membrane 2) fleece layer 3) plastic cage. It could be shown that the impact of plastic is negligible for all devices and operating conditions that are typically used in filtration applications. However, the performance, quantified in terms of water flow rate, has been found to be very sensitive to the resistance of the fleece layer even though it is lower than the resistance of the membrane by several orders of magnitude. Fleece permeability can be experimentally measured but such experiments are difficult to obtain and they were not available for the studied cartridges. This is further complicated by the fact that the permeability is anisotropic and that the fleece is always

compressed towards the center of the filter cartridge. Moreover, the degree of compression decreases under pressure. As these details are not considered in the geometries of CFD simulations, apparent permeabilities are estimated from measurement data. The corresponding resistances (1/permeability) are found to depend linearly on the applied pressure which can be exploited for predicting the performance of such cartridges at a wide range of applied pressures based on only two experiments. The prediction error was about 2 % which is in the same range as the assumed experimental error. Moreover, the estimated permeabilities can even be transferred between different cartridges in which the same fleece is used. The prediction error was below 10 % which still is a very good prediction considering that the simulation without the fleece layer can deviate from the corresponding experimental data by several hundred percent.

The significance of the fleece layer for the performance of pleated filter cartridges was previously not recognized in the scientific community and in particular the contribution of the three major mass transfer resistances couldn't be quantitatively distinguished. This finding provides novel insights for further improving the design of such cartridges both in academia and industry. The models provided in this thesis can help to further analyze and rationally design these cartridges and thus save costs and time consuming experiments. The proposed and demonstrated procedure can potentially be further improved by explicitly modeling the anisotropy and compression of fleece layers as a function of the pressure drop. However, such simulations are particularly challenging as they require to use a position dependent permeability tensor and fluid structure interaction (FSI). Moreover, since prediction of unused capsules can now be made with high accuracy this paves the way for also considering the retention mechanism including effects such as pore blocking and/or cake formation in the future. An additional point of interest would be to study different pleat types in the future.

5.2 Membrane Adsorbers

In the second part of the thesis surface interactions in membrane adsorbers are analyzed. As reported in previous studies the commonly applied Langmuir models found to be incapable of accurately describing binding of BSA to a strong anion-exchange membrane.

The binding process can be described accurately using the spreading model. However, the adsorption and desorption rates are found to depend on the applied flow rate. This relationship can be explained by the fact that the binding sites are mainly reached by convection in the membrane pores. This can be potentially exploited for predicting the performance of a MA at different flow rates based on a few measurements as for the filters. In addition, the performance of MAs with different flow configurations but containing the same membrane has been successfully predicted by transferring the binding parameters between the respective CFD models, which can be referred to as model-based scale-up. However, this can be complicated by several factors. First, the reference device from which the binding parameters are determined needs to be properly chosen. In particular the hydrodynamic behaviour needs to be reproducible as can be tested under non-binding conditions. Secondly, it needs to be ensured that membranes from the same production batch are used both in the scaled-down and scaled-up devices as lot-to-lot variations can otherwise deteriorate the results. Alternatively, the membrane capacity of a different lot can be determined in a separate experiment, as all other binding parameters are found to remain unaffected. At last, model-based scale-up can be challenging for highly complex geometries as particularly for the newly introduced Cassettes format. This can be addressed by a careful analysis of which details of the geometry are required for quantitative predictions. However, simplifying the geometry and exploiting symmetries is essential. Validated scale-up models can save a large amount of expensive material and hence money by minimizing the number of large scale experiments required under binding conditions. Moreover, such models can be used for screening design variants in operating conditions. In this thesis, a validated CFD models was applied for analyzing the scalability of Cassettes system by parallel operation of several Cassettes in one holder and variations of Cassettes with different bed height. In the future the same model can be used for studying parallelization of even more cartridges as well as further design variants.

Chapter 6

Appendix

Table 6.1: Detailed specifications of the studied cartridges

Cartridge	A	B	C	D	E	F	G	Units
Filtration area	0.57	0.76	0.52	0.56	0.60	0.45	0.51	m^2
Number of pleats	104	138	95	102	110	82	57	–
Pleat height	11.5	11.5	11.5	11.5	11.5	11.5	18.52	mm
Pleat width	240.5	240.5	240.3	240.3	240.3	240.5	240.5	mm
Core diameter	44	44	44	44	44	44	28	mm
Thickness of prefilter	163	155	160	160	160	–	–	μm
Thickness of main filter	150	150	153	153	153	160	160	μm
Thickness of fleece downstream	300	155	260	260	260	600	600	μm
Thickness of fleece upstream	300	155	260	260	260	600	600	μm
Water flow density of prefilter	83	137	91	91	91	–	–	$mL/(min * cm^2 * bar)$
Water flow density of main filter	25	25	25	25	25	257	257	$mL/(min * cm^2 * bar)$
Porosity of prefilter	0.78	0.79	0.79	0.79	0.79	–	–	–
Porosity of main filter	0.79	0.79	0.79	0.79	0.79	0.85	0.85	–
Mean flux pore size of prefilter	0.65	1.10	1.10	1.10	1.10	–	–	μm
Mean flux pore size of mainfilter	0.36	0.36	0.36	0.36	0.36	–	–	μm

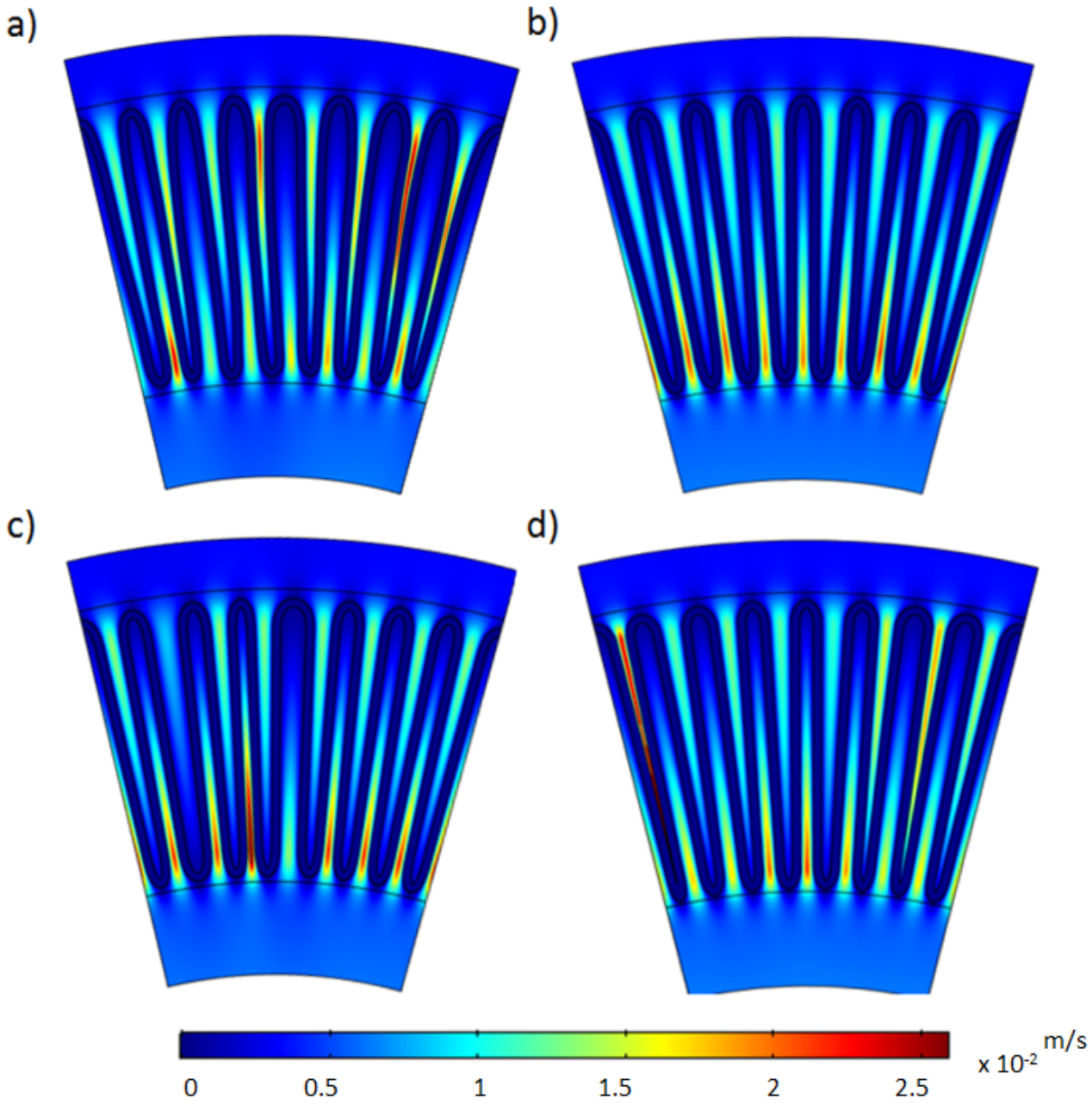

Figure 6.1: Simulated velocity magnitude profiles for cartridge A in a 2D cross section for a pressure drop of 0.1 *bar. The pleat geometry reconstructed by a) image analysis, b) regular generic, c) deterministic irregular generic, and d) randomized irregular design*

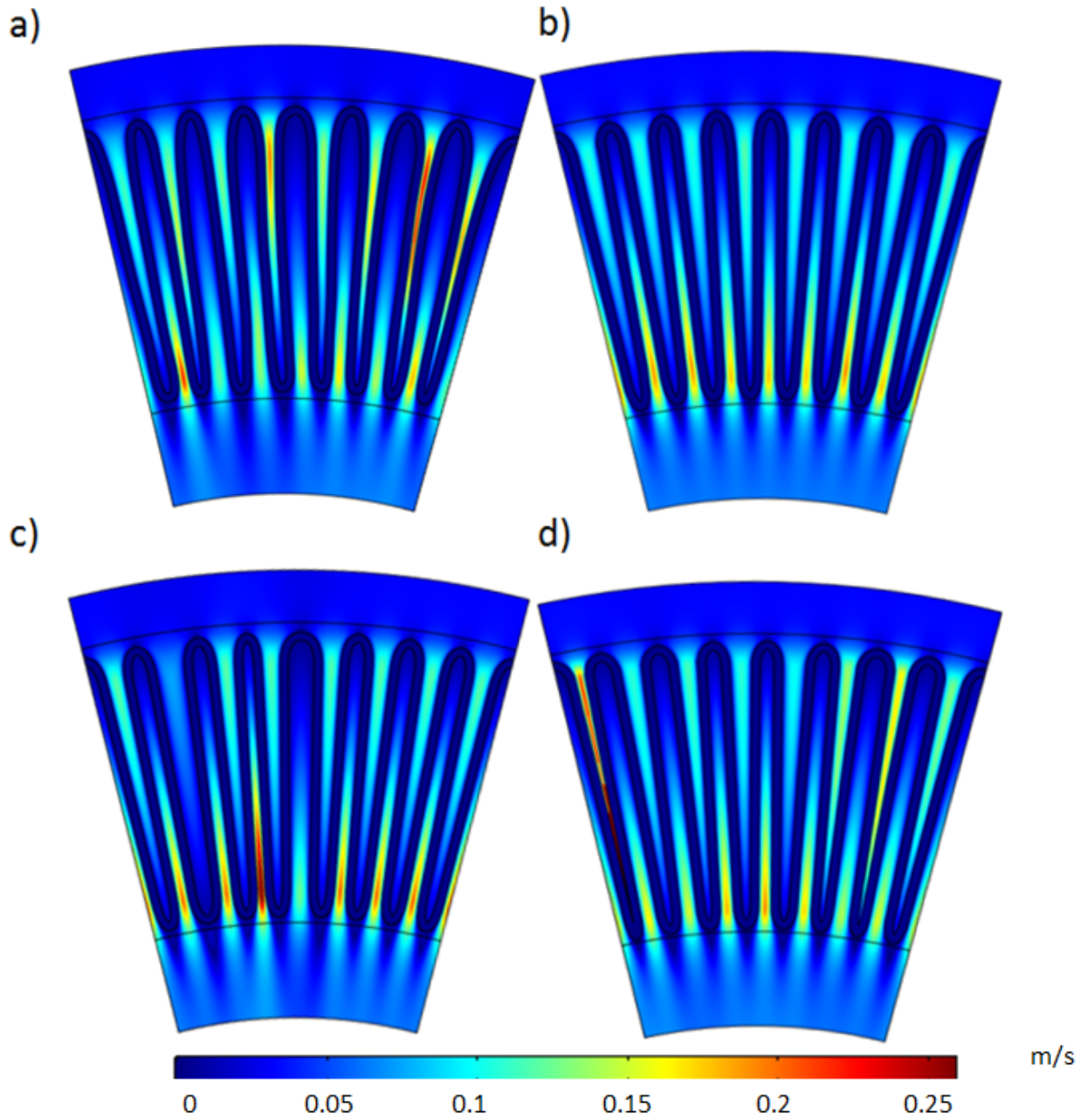

Figure 6.2: Simulated velocity magnitude profiles for cartridge A in a 2D cross section for a pressure drop of 1.0 *bar. The pleat geometry reconstructed by a) image analysis, b) regular generic, c) deterministic irregular generic, and d) randomized irregular design*

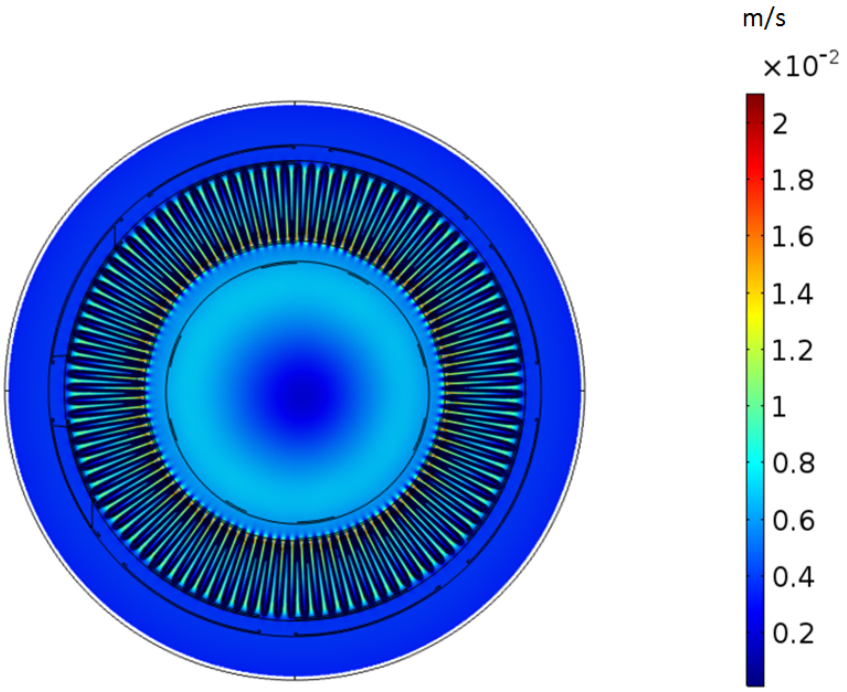

(a) Permeable

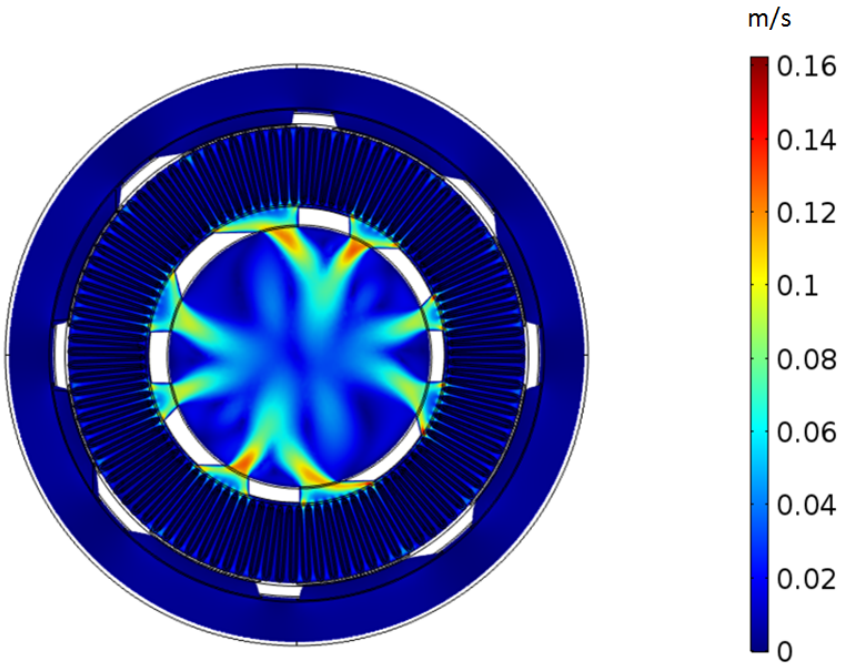

(b) Impermeable

Figure 6.3: Simulated velocity magnitude profiles for cartridge A in a 3D cylinder for a pressure drop of 0.1 *bar. The pleat geometry was reconstructed by the regular generic design. Both figures show a cross-section though the simulated cylinder*

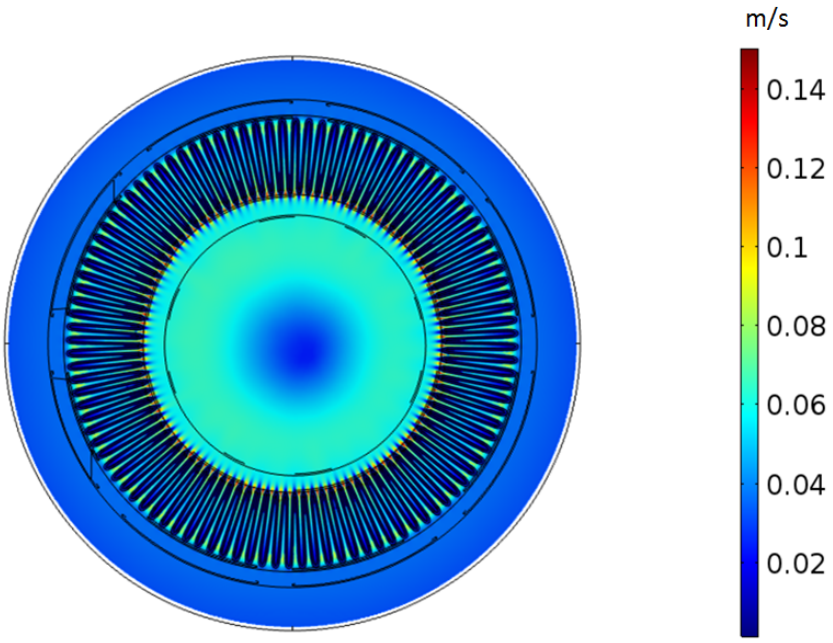

(a) Permeable

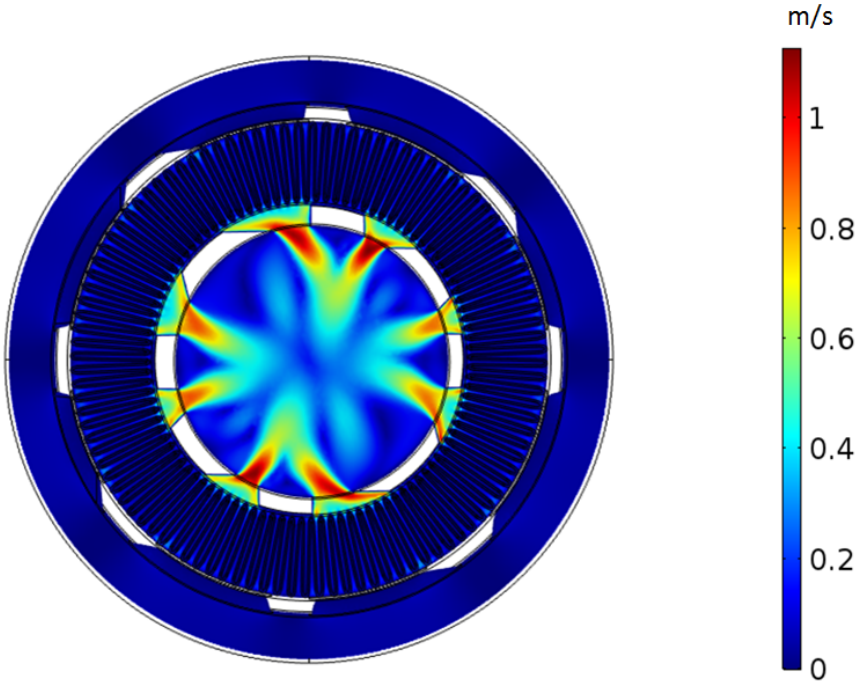

(b) Impermeable

Figure 6.4: Simulated velocity magnitude profiles for cartridge A in a 3D cylinder for a pressure drop of 1.0 *bar. The pleat geometry was reconstructed by the regular generic design. Both figures show a cross-section though the simulated cylinder*

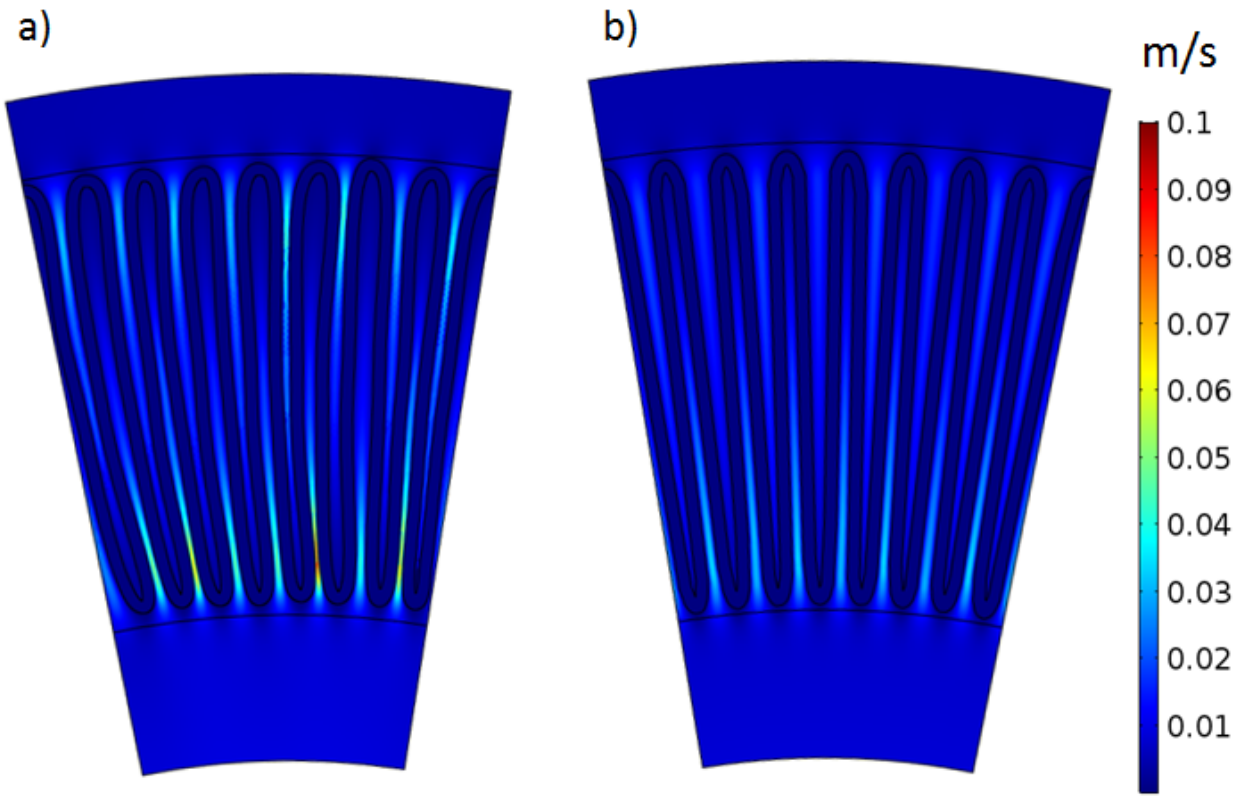

Figure 6.5: Simulated velocity magnitude profiles for cartridge B in a 2D cross section for a pressure drop of 0.1 *bar. The pleat geometry reconstructed by a) image analysis and b) regular generic design*

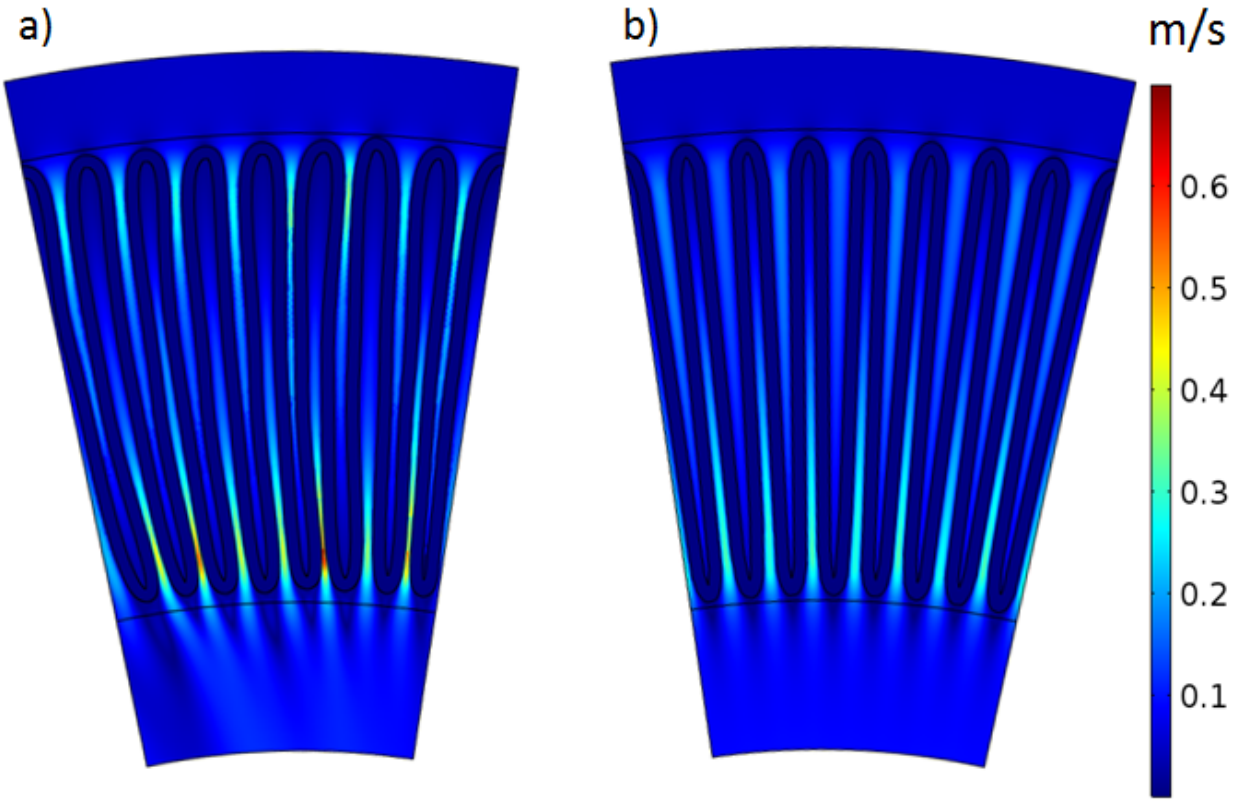

Figure 6.6: Simulated velocity magnitude profiles for cartridge B in a 2D cross section for a pressure drop of 1.0 *bar. The pleat geometry reconstructed by a) image analysis and b) regular generic design*

Bibliography

[1] T. Uragami. *Science and Technology of Separation Membranes*. Wiley, 2017.

[2] M Traube et al. Experimente zur Theorie der Zellenbildung und Endosmose. *Arch. Anat. Physiol. Wiss. Med*, 87:129, 1867.

[3] Wilhelm Pfeffer. *Osmotische Untersuchungen: Studien zur Zellmechanik*. W. Engelmann, 1877.

[4] FICK Adolf. Über Diffusion. *Poggendorff's Annalen*, 94:59–86, 1855.

[5] Jacobus H van't Hoff. Die Rolle des osmotischen Druckes in der Analogie zwischen Lösungen und Gasen. *Zeitschrift für physikalische Chemie*, 1(1):481–508, 1887.

[6] Walther Nernst. Zur Kinetik der in Lösung befindlichen Körper. *Zeitschrift für physikalische Chemie*, 2(1):613–637, 1888.

[7] Max Planck. Ueber die Erregung von Electricität und Wärme in Electrolyten. *Annalen der Physik*, 275(2):161–186, 1890.

[8] Francis G Donnan. Theorie der Membrangleichgewichte und Membranpotentiale bei Vorhandensein von nicht dialysierenden Elektrolyten. ein Beitrag zur physikalisch-chemischen Physiologie. *Berichte der Bunsengesellschaft für physikalische Chemie*, 17(14):572–581, 1911.

[9] Heinrich Bechhold. Kolloidstudien mit der Filtrationsmethode. *Zeitschrift für Physikalische Chemie*, 60(1):257–318, 1907.

[10] R Zsigmondy, E Wilke-Dörfurt, and Av Galecki. Anwendung der Ultrafiltration in der analytischen Chemie. *Berichte der deutschen chemischen Gesellschaft*, 45(1):579–582, 1912.

[11] Oscar W. W. Reif. *Microfiltration Membranes: Characteristics and Manufacturing*, pages 73–103. Springer Berlin Heidelberg, Berlin, Heidelberg, 2006.

[12] Marcel Mulder. Nature of membranes, 01 1993.

[13] Siegfried Ripperger, Walter Gösele, Christian Alt, and Thomas Loewe. *Filtration, 1. Fundamentals*. American Cancer Society, 2013.

[14] Lars Hagel, Günter Jagschies, and Gail Sofer. 4 - separation technologies. In Lars Hagel, Günter Jagschies, and Gail Sofer, editors, *Handbook of Process Chromatography (Second Edition)*, pages 81 – 125. Academic Press, Amsterdam, second edition edition, 2008.

[15] Adi Levi, Edo Bar-Zeev, Hila Elifantz, Tom Berman, and Ilana Berman-Frank. Characterization of microbial communities in water and biofilms along a large scale swro desalination facility: Site-specific prerequisite for biofouling treatments. *Desalination*, 378:44 – 52, 2016.

[16] T Christopher Dickenson. *Filters and filtration handbook*. Elsevier, 1997.

[17] O. Karnieli. Chapter 6 - bioreactors and downstream processing for stem cell manufacturing. In Joaquim M.S. Cabral, Cláudia Lobato de Silva, Lucas G. Chase, and Maria Margarida Diogo, editors, *Stem Cell Manufacturing*, pages 141 – 160. Elsevier, Boston, 2016.

[18] Zhaohuan Mai. *Procédés membranaires pour le traitement de l'eau, étude et modélisation des interctions entre membranes et composés organiques*. PhD thesis, 2013. Thèse de doctorat dirigée par Rakib, Mohammed Génie des procédés Châtenay-Malabry, Ecole centrale de Paris 2013.

[19] Nediljka Gaurina-Medjimurec. *Handbook of research on advancements in environmental engineering*. IGI Global, 2014.

[20] DY Kwon, S Vigneswaran, AG Fane, and R Ben Aim. Experimental determination of critical flux in cross-flow microfiltration. *Separation and Purification Technology*, 19(3):169–181, 2000.

[21] Steven S Lee, A Burt, G Russotti, and B Buckland. Microfiltration of recombinant yeast cells using a rotating disk dynamic filtration system. *Biotechnology and Bioengineering*, 48(4):386–400, 1995.

[22] Jens H Vogel and Karl-Heinz Kroner. Controlled shear filtration: a novel technique for animal cell separation. *Biotechnology and Bioengineering*, 63(6):663–674, 1999.

[23] David W. Kahn, Michelle D. Butler, Darien L. Cohen, Margaret Gordon, Jeanne W. Kahn, and Marjorie E. Winkler. Purification of plasmid dna by tangential flow filtration. *Biotechnology and Bioengineering*, 69(1):101–106, 2000.

[24] Pedro E Cruz, Cristina C Peixoto, Kathleen Devos, José L Moreira, Eric Saman, and Manuel J.T Carrondo. Characterization and downstream processing of hiv-1 core and virus-like-particles produced in serum free medium. *Enzyme and Microbial Technology*, 26(1):61 – 70, 2000.

[25] Richard J Wakeman. Separation technologies for sludge dewatering. *Journal of hazardous materials*, 144(3):614–619, 2007.

[26] Chalore Teepakorn, Koffi Fiaty, and Catherine Charcosset. A review on some recent advances on membrane chromatography for biomolecules purification. *Journal of Colloid Science and Biotechnology*, 5(1):32–44, 2016.

[27] AI Brown, P Levison, NJ Titchener-Hooker, and GJ Lye. Membrane pleating effects in 0.2 m rated microfiltration cartridges. *Journal of Membrane Science*, 341(1):76–83, 2009.

[28] Daniel J Brose, Michael Dosmar, and Maik W Jornitz. Membrane filtration. In *Development and Manufacture of Protein Pharmaceuticals*, pages 213–279. Springer, 2002.

[29] Moshe Rosenberg. Current and future applications for membrane processes in the dairy industry. *Trends in Food Science & Technology*, 6(1):12 – 19, 1995.

[30] V. Mavrov and E. Bélières. Reduction of water consumption and wastewater quantities in the food industry by water recycling using membrane processes. *Desalination*, 131(1):75 – 86, 2000.

[31] B. Girard, L. R. Fukumoto, and Dr. S. Sefa Koseoglu. Membrane processing of fruit juices and beverages: A review. *Critical Reviews in Biotechnology*, 20(2):109–175, 2000.

[32] Richard W. Baker. Future directions of membrane gas separation technology. *Industrial & Engineering Chemistry Research*, 41(6):1393–1411, 2002.

[33] Colin A. Scholes, Geoff W. Stevens, and Sandra E. Kentish. Membrane gas separation applications in natural gas processing. *Fuel*, 96:15 – 28, 2012.

[34] Marin Berovic. Sterilisation in biotechnology. volume 11 of *Biotechnology Annual Review*, pages 257 – 279. Elsevier, 2005.

[35] Abhinav A. Shukla and Jörg Thömmes. Recent advances in large-scale production of monoclonal antibodies and related proteins. *Trends in Biotechnology*, 28(5):253 – 261, 2010.

[36] Arunima Saxena, Bijay P. Tripathi, Mahendra Kumar, and Vinod K. Shahi. Membrane-based techniques for the separation and purification of proteins: An overview. *Advances in Colloid and Interface Science*, 145(1):1 – 22, 2009.

[37] Mikhail Tswett. Adsorption analysis and chromatographic method. application to the chemistry of chlorophyll. *Ber. Deut. Botan. Ges*, 24:385–393, 1906.

[38] Judith Wagner and Nat Lane. Paper chromatography*. *School Science and Mathematics*, 64(4):252–254, 1964.

[39] Raja Ghosh. Protein separation using membrane chromatography: opportunities and challenges. *Journal of Chromatography A*, 952(1):13 – 27, 2002.

[40] Cristiana Boi. Membrane adsorbers as purification tools for monoclonal antibody purification. *Journal of Chromatography B*, 848(1):19 – 27, 2007. Polyclonal and Monoclonal Antibody Production, Purification, Process and Product Analytics.

[41] Valerie Orr, Luyang Zhong, Murray Moo-Young, and C. Perry Chou. Recent advances in bioprocessing application of membrane chromatography. *Biotechnology Advances*, 31(4):450 – 465, 2013.

[42] D. Harkensee, Ö. Kökpinar, J. Walter, C. Kasper, S. Beutel, O.-W. Reif, T. Scheper, and R. Ulber. Fast screening for the purification of proteins using membrane adsorber technology. *Engineering in Life Sciences*, 7(4):388–394, 2007.

[43] Hironobu Shirataki, Chie Sudoh, Takamitsu Eshima, Yoshiro Yokoyama, and Kazuo Okuyama. Evaluation of an anion-exchange hollow-fiber membrane adsorber containing γ-ray grafted glycidyl methacrylate chains. *Journal of Chromatography A*, 1218(17):2381 – 2388, 2011. Selected Papers of the 4th Summer School of Monolith Technology for Biochromatography, Bioconversion and Phase State Synthesis.

[44] Luciana Cristina Lins de Aquino, Heloisa Ribeiro Tunes de Sousa, Everson Alves Miranda, Luciano Vilela, and Sônia Maria Alves Bueno. Evaluation of ida-peva hollow fiber membrane metal ion affinity chromatography for purification of a histidine-tagged human proinsulin. *Journal of Chromatography B*, 834(1):68 – 76, 2006.

[45] Ana M. Ventura, H. Marcelo Fernandez Lahore, Eduardo E. Smolko, and Mariano Grasselli. High-speed protein purification by adsorptive cation-exchange hollow-fiber cartridges. *Journal of Membrane Science*, 321(2):350 – 355, 2008.

[46] Alois Jungbauer and Rainer Hahn. Chapter 22 ion-exchange chromatography. In Richard R. Burgess and Murray P. Deutscher, editors, *Guide to Protein Purification, 2nd Edition*, volume 463 of *Methods in Enzymology*, pages 349 – 371. Academic Press, 2009.

[47] Toni Kline. *Handbook of affinity chromatography*. CRC Press, 1993.

[48] Raja Ghosh and Lu Wang. Purification of humanized monoclonal antibody by hydrophobic interaction membrane chromatography. *Journal of Chromatography A*, 1107(1):104 – 109, 2006.

[49] Philip M Cummins and Brendan F O'Connor. Hydrophobic interaction chromatography. In *Protein Chromatography*, pages 431–437. Springer, 2011.

[50] M.A. Teeters, S.E. Conrardy, B.L. Thomas, T.W. Root, and E.N. Lightfoot. Adsorptive membrane chromatography for purification of plasmid dna. *Journal of Chromatography A*, 989(1):165 – 173, 2003. 15th International Symposium on Preparative and Process Chromatography: Ion Exchange, Adsorption/Desorption Processes and Related Separation Techniques.

[51] Patricia Guerrero-Germán, Duarte M. F. Prazeres, Roberto Guzmán, Rosa Ma. Montesinos-Cisneros, and Armando Tejeda-Mansir. Purification of plasmid dna using tangential flow filtration and tandem anion-exchange membrane chromatography. *Bioprocess and Biosystems Engineering*, 32(5):615–623, Aug 2009.

[52] Heather N Endres, Julie AC Johnson, Carl A Ross, John K Welp, and Mark R Etzel. Evaluation of an ion-exchange membrane for the purification of plasmid dna. *Biotechnology and Applied Biochemistry*, 37(3):259–266, 2003.

[53] Shiying Zhang, Alla Krivosheyeva, and Samuel Nochumson. Large-scale capture and partial purification of plasmid dna using anion-exchange membrane capsules. *Biotechnology and Applied Biochemistry*, 37(3):245–249, 2003.

[54] Joe X Zhou and Tim Tressel. Basic concepts in q membrane chromatography for large-scale antibody production. *Biotechnology Progress*, 22(2):341–349, 2006.

[55] Deqiang Yu, Michael D McLean, J Christopher Hall, and Raja Ghosh. Purification of a human immunoglobulin g1 monoclonal antibody from transgenic tobacco using membrane chromatographic processes. *Journal of Chromatography A*, 1187(1-2):128–137, 2008.

[56] Rachel Specht, Binbing Han, S. Ranil Wickramasinghe, Jonathan O. Carlson, Peter Czermak, Anne Wolf, and Oscar-Werner Reif. Densonucleosis virus purification by ion exchange membranes. *Biotechnology and Bioengineering*, 88(4):465–473, 2004.

[57] Cristina Peixoto, Tiago B Ferreira, Marcos FQ Sousa, Manuel JT Carrondo, and Paula M Alves. Towards purification of adenoviral vectors based on membrane technology. *Biotechnology Progress*, 24(6):1290–1296, 2008.

[58] John David Anderson and J Wendt. *Computational fluid dynamics*, volume 206. Springer, 1995.

[59] Osborne Reynolds. Xxix. An experimental investigation of the circumstances which determine whether the motion of water shall he direct or sinuous, and of the law of resistance in parallel channels. *Philosophical Transactions of the Royal Society of London*, 174:935–982, 1883.

[60] David J Acheson. Elementary fluid dynamics, 1991.

[61] Yunus Cengel and John Cimbala. Fluid mechanics fundamentals and applications. 2013.

[62] Giancarlo Alfonsi. Reynolds-averaged navier-stokes equations for turbulence modeling. *Applied Mechanics Reviews - APPL MECH REV*, 62, 07 2009.

[63] Walter Frei. Comsol blogspot, July 2017.

[64] M. King Hubbert. Darcy's law and the field equations of the flow of underground fluids. *International Association of Scientific Hydrology. Bulletin*, 2(1):23–59, 1957.

[65] HC Brinkman. A calculation of the viscous force exerted by a flowing fluid on a dense swarm of particles. *Flow, Turbulence and Combustion*, 1(1):27, 1949.

[66] Peter Lyu. Which porous media and subsurface flow interface should i use?, 2017.

[67] John Campbell. Chapter 5 - solidification structure. In John Campbell, editor, *Complete Casting Handbook (Second Edition)*, pages 163 – 222. Butterworth-Heinemann, Boston, second edition edition, 2015.

[68] E. L. Cussler. *Fundamentals of Mass Transfer*, page 237–273. Cambridge Series in Chemical Engineering. Cambridge University Press, 3 edition, 2009.

[69] Ray M Bowen. *Introduction to continuum mechanics for engineers*. Plenum Press, 1989.

[70] Murray R Spiegel, Seymour Lipschutz, and Dennis Spellman. *Schaum's outline of theory and problems of vector analysis and an introduction to tensor analysis*, volume 36. McGraw-Hill New York, 1959.

[71] Larry A Glasgow. *Transport phenomena: an introduction to advanced topics*. John Wiley & Sons, 2010.

[72] Daryl L Logan. *A first course in the finite element method*. Cengage Learning, 2011.

[73] Olek C Zienkiewicz, Robert L Taylor, and Jian Z Zhu. *The finite element method: its basis and fundamentals*. Elsevier, 2005.

[74] Mumps, 2017.

[75] V. Nassehi, N.S. Hanspal, A.N. Waghode, W.R. Ruziwa, and R.J. Wakeman. Finite-element modelling of combined free/porous flow regimes: simulation of flow through pleated cartridge filters. *Chemical Engineering Science*, 60(4):995 – 1006, 2005.

[76] M J. Matteson and C Orr. Filtration: principles and practices. 01 1979.

[77] Maik W. Jornitz. *Filter Construction and Design*, pages 105–123. Springer Berlin Heidelberg, Berlin, Heidelberg, 2006.

[78] R.J. Wakeman, N.S. Hanspal, A.N. Waghode, and V. Nassehi. Analysis of pleat crowding and medium compression in pleated cartridge filters. *Chemical Engineering Research and Design*, 83(10):1246 – 1255, 2005.

[79] Mandar Dixit. Membranes and filtration: Membrane filtration in the biopharm industry. *Filtration & Separation*, 45(8):18–21, 2008.

[80] Bruno F Marques, David J Roush, and Kent E Göklen. Virus filtration of high-concentration monoclonal antibody solutions. *Biotechnology Progress*, 25(2):483–491, 2009.

[81] Stephan Klutz, Jorgen Magnus, Martin Lobedann, Peter Schwan, Benjamin Maiser, Jens Niklas, Maike Temming, and Gerhard Schembecker. Developing the biofacility of the future based on continuous processing and single-use technology. *Journal of Biotechnology*, 213:120–130, 2015.

[82] NA Belyakov, VA Voinov, and SA Simbirtsev. Blood microfilters. *Biomedical Engineering*, 11(6):331–336, 1977.

[83] Luisa A Ikner, Charles P Gerba, and Kelly R Bright. Concentration and recovery of viruses from water: a comprehensive review. *Food and Environmental Virology*, 4(2):41–67, 2012.

[84] SAMUEL R Farrah, CHARLES P Gerba, CRAIG Wallis, and JOSEPH L Melnick. Concentration of viruses from large volumes of tap water using pleated membrane filters. *Applied and Environmental Microbiology*, 31(2):221–226, 1976.

[85] Charles P Gerba, SAMUEL R Farrah, Sagar M Goyal, CRAIG Wallis, and Joseph L Melnick. Concentration of enteroviruses from large volumes of tap water, treated sewage, and seawater. *Applied and Environmental Microbiology*, 35(3):540–548, 1978.

[86] David R Preston, Tirucherai V Vasudevan, Gabriel Bitton, Samuel R Farrah, and Jean-Louis Morel. Novel approach for modifying microporous filters for virus concentration from water. *Applied and Environmental Microbiology*, 54(6):1325–1329, 1988.

[87] PATRICIA A Shields, SHARON A Berenfeld, and SAMUEL R Farrah. Modified membrane-filter procedure for concentration of enteroviruses from tap water. *Applied and Environmental Microbiology*, 49(2):453–455, 1985.

[88] JL Cashdollar and L Wymer. Methods for primary concentration of viruses from water samples: a review and meta-analysis of recent studies. *Journal of Applied Microbiology*, 115(1):1–11, 2013.

[89] Mohammad R Karim, Eric R Rhodes, Nichole Brinkman, Larry Wymer, and G Shay Fout. New electropositive filter for concentrating enteroviruses and noroviruses from large volumes of water. *Applied and Environmental Microbiology*, 75(8):2393–2399, 2009.

[90] Luisa A Ikner, Marcela Soto-Beltran, and Kelly R Bright. New method using a positively charged microporous filter and ultrafiltration for concentration of viruses from tap water. *Applied and Environmental Microbiology*, 77(10):3500–3506, 2011.

[91] CD Gibbons, RA Rodriguez, L Tallon, and MD Sobsey. Evaluation of positively charged alumina nanofibre cartridge filters for the primary concentration of noroviruses, adenoviruses and male-specific coliphages from seawater. *Journal of Applied Microbiology*, 109(2):635–641, 2010.

[92] KH Oshima, TT Evans-Strickfaden, AK Highsmith, and EW Ades. The use of a microporous polyvinylidene fluoride (pvdf) membrane filter to separate contaminating viral particles from biologically important proteins. *Biologicals*, 24(2):137–145, 1996.

[93] Shengjiang Liu, Mark Carroll, Raquel Iverson, Christine Valera, Joann Vennari, Kimberly Turco, Robert Piper, Robert Kiss, and Herbert Lutz. Development and qualification of a novel virus removal filter for cell culture applications. *Biotechnology Progress*, 16(3):425–434, 2000.

[94] AI Brown, NJ Titchener-Hooker, and GJ Lye. Scale-down prediction of industrial

scale pleated membrane cartridge performance. *Biotechnology and Bioengineering*, 108(4):830–838, 2010.

[95] Da-Ren Chen, David Y. H. Pui, and Benjamin Y. H. Liu. Optimization of pleated filter designs using a finite-element numerical model. *Aerosol Science and Technology*, 23(4):579–590, 1995.

[96] Henry HS Yu and Cecil H Goulding. Optimized ultra high efficiency filter for high-efficiency industrial combustion turbines. *Atmosphere*, 1:1, 1992.

[97] Félicie Théron, Aurélie Joubert, and Laurence Le Coq. Numerical and experimental investigations of the influence of the pleat geometry on the pressure drop and velocity field of a pleated fibrous filter. *Separation and Purification Technology*, 182:69–77, 2017.

[98] Shaowen Chen, Qiang Wang, and Da-Ren Chen. Effect of pleat shape on reverse pulsed-jet cleaning of filter cartridges. *Powder Technology*, 305:1 – 11, 2017.

[99] A. Subrenat, J. Bellettre, and P. Le Cloirec. 3-d numerical simulations of flows in a cylindrical pleated filter packed with activated carbon cloth. *Chemical Engineering Science*, 58(22):4965 – 4973, 2003.

[100] Sal Giglia, Kevin Rautio, Greg Kazan, Kari Backes, Mark Blanchard, and John Caulmare. Improving the accuracy of scaling from discs to cartridges for dead end microfiltration of biological fluids. *Journal of Membrane Science*, 365(1):347–355, 2010.

[101] Robert L. Fahrner, Heather L. Knudsen, Carol D. Basey, Walter Galan, Dian Feuerhelm, Martin Vanderlaan, and Gregory S. Blank. Industrial purification of pharmaceutical antibodies: Development, operation, and validation of chromatography processes. *Biotechnology and Genetic Engineering Reviews*, 18(1):301–327, 2001.

[102] Raja Ghosh. Protein separation using membrane chromatography: opportunities and challenges. *Journal of Chromatography A*, 952(1):13 – 27, 2002.

[103] Jörg Thömmes and Mark Etzel. Alternatives to chromatographic separations. *Biotechnology Progress*, 23(1):42–45, 2007.

[104] Cristiana Boi, Simone Dimartino, and Giulio C. Sarti. Modelling and simulation of affinity membrane adsorption. *Journal of Chromatography A*, 1162(1):24 – 33, 2007. 11th International Symposium on Preparative and Industrial Chromatography and Allied Techniques.

[105] Pedram Madadkar, Qijiayu Wu, and Raja Ghosh. A laterally-fed membrane chromatography module. *Journal of Membrane Science*, 487:173 – 179, 2015.

[106] Ayahito Shiosaki, Motonobu Goto, and Tsutomu Hirose. Frontal analysis of protein adsorption on a membrane adsorber. *Journal of Chromatography A*, 679(1):1–9, 1994.

[107] Johannes Winderl, Tobias Hahn, and Jürgen Hubbuch. A mechanistic model of ion-exchange chromatography on polymer fiber stationary phases. *Journal of Chromatography A*, 1475(Supplement C):18 – 30, 2016.

[108] Tiago Vicente, René Fáber, Paula M. Alves, Manuel J.T. Carrondo, and José P.B. Mota. Impact of ligand density on the optimization of ion-exchange membrane chromatography for viral vector purification. *Biotechnology and Bioengineering*, 108(6):1347–1359, 2011.

[109] Constantin Frerick, Peter Kreis, Andrzej Górak, Alexander Tappe, and Dieter Melzner. Simulation of a human serum albumin downstream process incorporating ion-exchange membrane adsorbers. *Chemical Engineering and Processing: Process Intensification*, 47(7):1128 – 1138, 2008. Euromembrane 2006.

[110] Simone Dimartino, Cristiana Boi, and Giulio C Sarti. A validated model for the simulation of protein purification through affinity membrane chromatography. *Journal of Chromatography A*, 1218(13):1677–1690, 2011.

[111] Pranay Ghosh, Kaveh Vahedipour, Min Lin, Jens H. Vogel, Charles Haynes, and Eric von Lieres. Computational fluid dynamic simulation of axial and radial

flow membrane chromatography: Mechanisms of non-ideality and validation of the zonal rate model. *Journal of Chromatography A*, 1305:114 – 122, 2013.

[112] Pranay Ghosh, Kaveh Vahedipour, Martin Leuthold, and Eric von Lieres. Model-based analysis and quantitative prediction of membrane chromatography: Extreme scale-up from 0.08ml to 1200ml. *Journal of Chromatography A*, 1332:8 – 13, 2014.

[113] Chalore Teepakorn, Koffi Fiaty, and Catherine Charcosset. Effect of geometry and scale for axial and radial flow membrane chromatography—experimental study of bovin serum albumin adsorption. *Journal of Chromatography A*, 1403:45 – 53, 2015.

[114] Heewon Yang, Matthias Bitzer, and Mark R. Etzel. Analysis of protein purification using ion-exchange membranes. *Industrial & Engineering Chemistry Research*, 38(10):4044–4050, 1999.

[115] Cristiana Boi. Membrane adsorbers as purification tools for monoclonal antibody purification. *Journal of Chromatography B*, 848(1):19 – 27, 2007. Polyclonal and Monoclonal Antibody Production, Purification, Process and Product Analytics.

[116] Chalore Teepakorn, Denis Grenier, Koffi Fiaty, and Catherine Charcosset. Characterization of hydrodynamics in membrane chromatography devices using magnetic resonance imaging and computational fluid dynamics. *Chemical Engineering Research and Design*, 113(Supplement C):61 – 73, 2016.

[117] K.H. Gebauer, J. Thömmes, and M.R. Kula. Breakthrough performance of high-capacity membrane adsorbers in protein chromatography. *Chemical Engineering Science*, 52(3):405 – 419, 1997.

[118] Justin T. McCue, Philip Engel, Austen Ng, Rich Macniven, and Jörg Thömmes. Modeling of protein monomer/aggregate purification and separation using hydrophobic interaction chromatography. *Bioprocess and Biosystems Engineering*, 31(3):261, Jan 2008.

[119] Heewon Yang and Mark R. Etzel. Evaluation of three kinetic equations in models of protein purification using ion-exchange membranes. *Industrial & Engineering Chemistry Research*, 42(4):890–896, 2003.

[120] Eirini Velali, Birgit Stute, Martin Leuthold, and Eric von Lieres. Model-based performance analysis and scale-up of membrane adsorbers with a cassettes format designed for parallel operation. *Chemical Engineering Science*, 192:103–113, 2018.

[121] Philip Kriegel. Plate and frame filter press. *Industrial & Engineering Chemistry*, 30(11):1211–1213, 1938.

[122] Shing-Yi Suen, Yung-Chuan Liu, and Chao-Shuan Chang. Exploiting immobilized metal affinity membranes for the isolation or purification of therapeutically relevant species. *Journal of Chromatography B*, 797(1-2):305–319, 2003.